NASA/TM–2016-217551

Atmospheric Correction for Satellite Ocean Color Radiometry

Curtis D. Mobley, Jeremy Werdell, Bryan Franz, Ziauddin Ahmad, and Sean Bailey

National Aeronautics and
Space Administration

Goddard Space Flight Center
Greenbelt, Maryland 20771

June 2016

NASA STI Program ... in Profile

Since its founding, NASA has been dedicated to the advancement of aeronautics and space science. The NASA scientific and technical information (STI) program plays a key part in helping NASA maintain this important role.

The NASA STI program operates under the auspices of the Agency Chief Information Officer. It collects, organizes, provides for archiving, and disseminates NASA's STI. The NASA STI program provides access to the NASA Aeronautics and Space Database and its public interface, the NASA Technical Report Server, thus providing one of the largest collections of aeronautical and space science STI in the world. Results are published in both non-NASA channels and by NASA in the NASA STI Report Series, which includes the following report types:

- TECHNICAL PUBLICATION. Reports of completed research or a major significant phase of research that present the results of NASA Programs and include extensive data or theoretical analysis. Includes compilations of significant scientific and technical data and information deemed to be of continuing reference value. NASA counterpart of peer-reviewed formal professional papers but has less stringent limitations on manuscript length and extent of graphic presentations.

- TECHNICAL MEMORANDUM. Scientific and technical findings that are preliminary or of specialized interest, e.g., quick release reports, working papers, and bibliographies that contain minimal annotation. Does not contain extensive analysis.

- CONTRACTOR REPORT. Scientific and technical findings by NASA-sponsored contractors and grantees.

- CONFERENCE PUBLICATION. Collected papers from scientific and technical conferences, symposia, seminars, or other meetings sponsored or co-sponsored by NASA.

- SPECIAL PUBLICATION. Scientific, technical, or historical information from NASA programs, projects, and missions, often concerned with subjects having substantial public interest.

- TECHNICAL TRANSLATION. English-language translations of foreign scientific and technical material pertinent to NASA's mission.

Specialized services also include organizing and publishing research results, distributing specialized research announcements and feeds, providing help desk and personal search support, and enabling data exchange services. For more information about the NASA STI program, see the following:

- Access the NASA STI program home page at http://www.sti.nasa.gov

- E-mail your question via the Internet to help@sti.nasa.gov

- Fax your question to the NASA STI Help Desk at 443-757-5803

- Phone the NASA STI Help Desk at 443-757-5802

NASA/TM–2016-217551

Atmospheric Correction for Satellite Ocean Color Radiometry

Curtis D. Mobley
Sequoia Scientific, Inc., Bellevue, WA

Jeremy Werdell
NASA's Goddard Space Flight Center, Greenbelt, MD

Bryan Franz
NASA's Goddard Space Flight Center, Greenbelt, MD

Ziauddin Ahmad
NASA's Goddard Space Flight Center, Greenbelt, MD

Sean Bailey
NASA's Goddard Space Flight Center, Greenbelt, MD

National Aeronautics and
Space Administration

Goddard Space Flight Center
Greenbelt, Maryland 20771

June 2016

Abstract

This tutorial is an introduction to atmospheric correction in general and also documentation of the atmospheric correction algorithms currently implemented by the NASA Ocean Biology Processing Group (OBPG) for processing ocean color data from satellite-borne sensors such as MODIS and VIIRS. The intended audience is graduate students or others who are encountering this topic for the first time. The tutorial is in two parts. Part I discusses the generic atmospheric correction problem. The magnitude and nature of the problem are first illustrated with numerical results generated by a coupled ocean-atmosphere radiative transfer model. That code allow the various contributions (Rayleigh and aerosol path radiance, surface reflectance, water-leaving radiance, etc.) to the top-of-the-atmosphere (TOA) radiance to be separated out. Particular attention is then paid to the definition, calculation, and interpretation of the so-called "exact normalized water-leaving radiance" and its equivalent reflectance. Part I ends with chapters on the calculation of direct and diffuse atmospheric transmittances, and on how vicarious calibration is performed. Part II then describes one by one the particular algorithms currently used by the OBPG to effect the various steps of the atmospheric correction process, viz. the corrections for absorption and scattering by gases and aerosols, Sun and sky reflectance by the sea surface and whitecaps, and finally corrections for sensor out-of-band response and polarization effects. One goal of the tutorial—guided by teaching needs— is to distill the results of dozens of papers published over several decades of research in atmospheric correction for ocean color remote sensing. Any subsequent modifications to the originally published techniques are noted in the documentation. This content of this tutorial is available online as the *Atmospheric Correction* chapter of the *Ocean Optics Web Book*, beginning at `http://www.oceanopticsbook.info/view/atmospheric_correction/chapter_overview`. A pdf version of the report can be downloaded as Mobley et al. (2016) in the publications section of the *Ocean Optics Web Book*.

Acknowledgments

Contents

List of Figures

List of Tables

Part I

The Atmospheric Correction Problem

In several recent years the NASA Ocean Biology and Biogeochemistry Program supported an intensive summer course, "Ocean Optics Summer Class: Calibration and Validation in Support of Ocean Color Remote Sensing," at the University of Maine (`http://misclab.umeoce.maine.edu/education.php`). Those graduate-level classes covered both theory and instrumentation for optical oceanography and ocean color remote sensing. During those courses, Jeremy Werdell of the NASA Goddard Space Flight Center, Ocean Biology Processing Group (OBPG) gave lectures on how the OBPG calibrates, validates, and processes ocean color data from sensors such as SeaWiFS, MODIS, and VIIRS (Werdell, 2015). His lectures outlined the many complicated steps used for atmospheric correction of measured at-sensor radiances and inspired this tutorial.

The purpose of this tutorial is to expand upon Werdell's lectures and review and summarize in one document the entire process of atmospheric correction as currently implemented by OBPG. The algorithms and equations presented here rest on several decades of research going all the way back to the Coastal Zone Color Scanner (CZCS), which was launched in 1978. References are given to the original literature, which can be consulted for historical perspective and the scientific underpinnings and details of the current algorithms.

There are many other sources with additional information about atmospheric correction. The NASA ocean color web site at `http://oceancolor.gsfc.nasa.gov/cms/` contains a wealth of information about how NASA collects, processes, calibrates, validates, archives and distributes ocean color data from a variety of satellite sensors. That web site has many pages with links to various technical memos and other information about ocean color, and many of the data files underlying the atmospheric correction process can be downloaded there.

There are also many non-NASA sources of information on atmospheric correction. The Ocean Optics Web Book (`http://www.oceanopticsbook.info/`) presents basic information on optical oceanography and ocean-color remote sensing needed to understand the present tutorial. The University of Maine website given above links to PowerPoint presentations of lectures given at the University of Maine summer courses, and to videos of the 2015 lectures. The International Ocean Color Coordinating Group (IOCCG) has hosted summer lecture series during which the lectures were videoed. The IOCCG lectures delivered by Menghua Wang in 2012 and 2014 (`http://www.ioccg.org/training/SLS-2012/` and `http://www.ioccg.org/training/SLS-2014/`) cover much of the material presented here. IOCCG report 10 (`http://www.ioccg.org/reports/report10.pdf`) compares the SeaWiFS-MODIS vs. MERIS vs. OCTS-GLI vs. POLDER atmospheric correction algorithms, but assumes that the reader is already familiar with the general process.

This tutorial is organized as follows. Part I first formulates the atmospheric correction problem in terms of the various contributions to the top-of-the-atmosphere (TOA) radiance measured by a satellite-borne sensor. Those contributions come from solar radiance scattered by atmospheric molecules and aerosols, Sun and sky radiance reflected by the sea surface (either by the water surface itself or by foam from whitecaps), and finally from water-leaving radiance. The nature and magnitude of these contributions is then illustrated using numerical simulations from a coupled ocean-atmosphere radiative transfer model. The computations of various reflectances and atmospheric transmittances are then discussed in detail. Part II then treats the various contributions in turn, showing how each undesired contribution is estimated so that it can be removed from the measured TOA value. The end result is an estimate of the water-leaving radiance, or its corresponding exact normalized water-leaving reflectance, which carries information about the water-column

itself.

Once obtained, the normalized water-leaving reflectance is the input to algorithms for retrieval of various quantities of scientific interest. These ocean-color products include—among others—the Chlorophyll *a* concentration, the water-column diffuse attenuation for downwelling plane irradiance at 490 nm (Kd490, which is a proxy for water transparency), water-column absorption and backscatter coefficients, and particulate organic and inorganic Carbon. The algorithms for retrieval of specific products, given the normalized reflectance, are given in a series of reports found at `http://oceancolor.gsfc.nasa.gov/cms/atbd`. Those retrieval algorithms are not discussed here.

Problem Formulation

The total radiance L_{t} measured by a satellite-borne sensor at the top of the atmosphere (TOA) comes from contributions by atmospheric scattering, L_{atm}; Sun and sky radiance reflected back upward by the sea-surface and reaching the TOA, $L_{\text{surf}}^{\text{TOA}}$; and water-leaving radiance that reaches the TOA, $L_{\text{w}}^{\text{TOA}}$:

$$L_{\text{t}} = L_{\text{atm}} + L_{\text{surf}}^{\text{TOA}} + L_{\text{w}}^{\text{TOA}} . \tag{1.1}$$

For brevity, the viewing direction $(\theta_{\text{v}}, \phi_{\text{v}})$ and wavelength λ are not shown. Expanding this equation into further levels of detail requires the definition of many different radiances, and precise notation is needed to minimise confusion. The atmospheric contribution L_{atm} is always considered to be at the TOA. However, the surface-reflected radiance and water-leaving radiance can be formulated either at the sea surface or at the TOA. For these radiances, a superscript TOA will be used to specify the TOA value. Thus L_{w} will denote the water-leaving radiance just above the sea surface, and $L_{\text{w}}^{\text{TOA}}$ will denote how much of L_{w} reaches the TOA. Table 1.1 summarizes the various radiances introduced in this chapter and used throughout this report.

The atmospheric contribution in Eq. (1.1), usually called atmospheric path radiance, comes from scattering by atmospheric gases and aerosols, including multiple scattering between gases and aerosols. The path radiance that comes solely from scattering by atmospheric gas molecules is usually called the Rayleigh radiance, L_{R}, because scattering by molecules is well described by the Rayleigh mathematical model of scattering by particles that are much smaller than the wavelength of light. In the absence of any aerosols, the atmospheric path radiance would equal the Rayleigh radiance. Let L_{a} denote the aerosol contribution, which is the path radiance that would occur if the atmosphere consisted only of aerosol particles. Let L_{aR} denote the contribution resulting from multiple scattering between aerosols and gases. The total surface reflectance can be separated into a contribution due to direct Sun glint from the water surface, $L_{\text{g}}^{\text{TOA}}$; by background sky radiance reflected by the water surface, $L_{\text{sky}}^{\text{TOA}}$; and by Sun and sky radiance reflected by whitecaps and foam, $L_{\text{wc}}^{\text{TOA}}$. Thus Eq. (1.1) can be further partitioned into

$$L_{\text{t}} = L_{\text{R}} + [L_{\text{a}} + L_{\text{aR}}] + L_{\text{g}}^{\text{TOA}} + L_{\text{sky}}^{\text{TOA}} + L_{\text{wc}}^{\text{TOA}} + L_{\text{w}}^{\text{TOA}} . \tag{1.2}$$

In practice, the aerosol and aerosol-gas contributions are usually grouped together and treated as one contribution, sometimes denoted $L_{\text{A}} = L_{\text{a}} + L_{\text{aR}}$ and often called just the aerosol contribution.

Table 1.1: Radiance notation. Spectral radiance L has SI units of W m^{-2} nm^{-1} sr^{-1}; in practice mW cm^{-2} μm^{-1} sr^{-1} is often used.

Symbol	Definition
L_t	total upwelling radiance at the top of the atmosphere
L_atm	total contribution of atmospheric scattering to the TOA radiance
$L_\mathrm{surf}^\mathrm{TOA}$	total contribution of surface-reflected radiance to the TOA radiance
L_R	total Rayleigh radiance at the TOA
L_r	"standardardized" Rayleigh radiance at the TOA
L_a	TOA radiance due to scattering by aerosols only
L_aR	TOA radiance due to aerosol-molecule scattering
L_A	$L_\mathrm{a} + L_\mathrm{aR}$; total aerosol radiance at the TOA
L_w	water-leaving radiance just above the sea surface
$L_\mathrm{w}^\mathrm{TOA}$	the part of the water-leaving radiance L_w that reaches the TOA
L_g	direct Sun glint radiance just above the sea surface
$L_\mathrm{g}^\mathrm{TOA}$	the part of the direct Sun glint radiance L_g that reaches the TOA
L_sky	surface-reflected background sky radiance at the sea surface
$L_\mathrm{sky}^\mathrm{TOA}$	the part of the surface-reflected background sky radiance L_sky that reaches the TOA
L_wc	radiance due to whitecaps and foam just above the sea surface
$L_\mathrm{wc}^\mathrm{TOA}$	the part of the whitecap radiance L_wc that reaches the TOA
L_u	upwelling underwater radiance just beneath the sea surface

The sky reflectance term is accounted for as part of the Rayleigh correction, which incorporates reflectance by the sea surface. For some sensors that were specifically optimized for ocean color (e.g., CZCS and SeaWiFS), the strongest part of the Sun glint (the Sun's glitter pattern) is avoided by pointing the sensor in a direction away from the Sun so that almost no direct glint is present in the image. However, there is still a correction for residual amounts of Sun glint. Figure 1.1 illustrates these contributions to the TOA radiance.

Most papers (e.g., Wang and Bailey, 2001; Wang, 2002) rewrite Eq. (1.2) as

$$L_\mathrm{t} = L_\mathrm{R} + [L_\mathrm{a} + L_\mathrm{Ra}] + T L_\mathrm{g} + t L_\mathrm{wc} + t L_\mathrm{w}\,, \tag{1.3}$$

or something very similar. Now, however, L_g, L_wc, and L_w are all measured at sea level. T is the direct transmittance between the sea surface and the TOA along the viewing direction, and t is diffuse transmittance in the viewing direction. These transmittances are discussed in §4.

Yet a third formulation can be found in the literature (e.g., Franz et al., 2007, Eq. 1):

$$L_\mathrm{t} = \left(L_\mathrm{r} + [L_\mathrm{a} + L_\mathrm{ra}] + t_\mathrm{dv} L_\mathrm{wc} + t_\mathrm{dv} L_\mathrm{w}\right) t_\mathrm{gv} t_\mathrm{gs} f_\mathrm{p}\,. \tag{1.4}$$
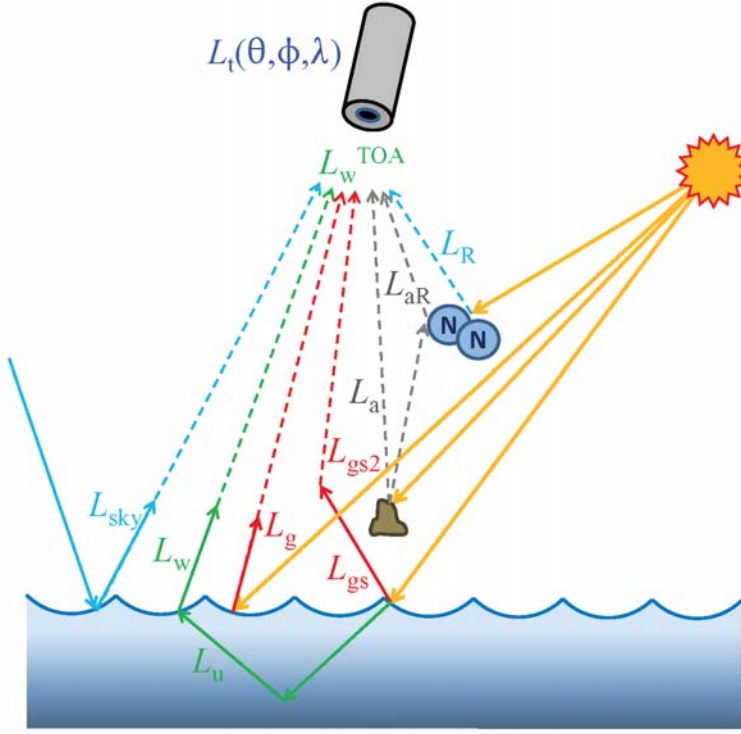
Figure 1.1: Qualitative illustrations of the various processes contributing to the total TOA radiance. The notation corresponds to Table 1.1 and colors correspond to the spectra of Fig. 2.2. The blue N-N represents a nitrogen (N_2) molecule, or any other atmospheric gas molecule; the brown blob represents an aerosol particle. The red glint terms are discussed in §2.

Here t_{dv} is the diffuse transmittance along the viewing path of the sensor. t_{gv} is the transmittance by atmospheric gases in the viewing direction, and t_{gs} is the transmittance by atmospheric gases in the Sun's direction; these transmittances are usually called gaseous transmittances. f_p is a known instrument polarization-correction factor. Comparison of Eqs. (1.3) and (1.4) shows, for example, that

$$L_R = L_r t_{gv} t_{gs} f_p \,.$$

Thus the total TOA Rayleigh contribution L_R has been factored into a product of terms involving a Rayleigh term times gaseous transmittances and a polarization-correction factor. The difference between Eqs. (1.3) and (1.4) is primarily a matter of simplification for presentation purposes. The f_p term came into the nomenclature because MODIS has large polarization sensitivity and this requires correction. Earlier papers by Gordon and Wang often ignored the gaseous transmission terms because they were only considering ozone, which could be "taken off the top," so to speak, with the remaining problem being effectively formulated below the ozone layer. The L_r term is computed using a standard atmosphere and only non-absorbing gases N_2 and O_2. This allows "standard" Rayleigh radiances L_r to be computed as a function of Sun and viewing geometry. The gaseous transmittances are computed by use of absorption coefficients, computed path lengths, and

gas concentrations for the various gases. The f_p term is computed for each image pixel as a function of atmosphere and surface polarization states (modeled Rayleigh and glint Stokes vectors) and the sensor-specific polarization sensitivity with viewing direction.

All of Eqs. (1.2), (1.3), and (1.4) can be found in the literature. They all give the same TOA total radiance L_t. Which form is used in a particular instance is determined by convenience. Forms (1.2), (1.3) are often convenient for discussions of theory, whereas form (1.4) is convenient for operational atmospheric correction algorithms.

The goal of atmospheric correction is to convert a measured top-of-the-atmosphere radiance L_t into the corresponding sea-level water-leaving radiance L_w. Since only L_t is measured, this requires estimation of the various atmospheric and surface-reflectance terms seen in Eqs. (1.3) or (1.4) so that they can be subtracted from L_t in order to arrive at L_w. How this is done is the subject of Part II of this report.

Example Radiances

Let us illustrate the magnitudes of the various radiances in Eqs. (1.2) and (1.3) with a specific example. The orbital characteristics of the proposed NASA HyspIRI (Hyperspectral Infrared Imager; `http://hyspiri.jpl.nasa.gov/`) satellite were used to obtain the Sun zenith and azimuthal angles at the time the sensor would fly over a point at (latitude, longitude) = (28.75 N, 158.00 W) on June 21. This point is north of the island of Oahu in Hawaii and is known as Station ALOHA (A Long-term Oligotrophic Habitat Assessment). Figure 2.1 shows the relevant angles needed for the simulation. A coupled HydroLight-MODTRAN ocean-atmosphere radiative transfer code was used to compute the in-water and atmospheric radiances both just above the sea surface and at the top of the atmosphere. (HydroLight is an underwater radiative transfer code; `http://www.hydrolight.info`. MODTRAN is an atmospheric code; `http://www.modtran5.com/about/index.html`. Both are widely used for radiative transfer calculations in their respective geophysical domains.) That code can separate the Rayleigh vs. [aerosol + aerosol-Rayleigh] contributions, but cannot separate the pure aerosol from the aerosol-Rayleigh contributions. Like wise, it does not normally separate Sun glint and sky glint contributions, although that separation can be effected with some extra effort (explained below). (The partitioning of atmospheric radiance contributions in the model simulations is not exactly the same as is done operationally, but the model simulations can still illustrate the various contributions to the TOA radiance.)

A simulation was done for the following environmental conditions:

- The water was homogeneous and infinitely deep.

- The water IOPs were simulated using a chlorophyll concentration of $Chl = 0.05$ mg m^{-3} in the "new Case 1" IOP model in HydroLight. This IOP model is based on Bricaud et al. (1998) for absorption and Morel et al. (2002) for scattering. (This IOP model is described in detail at `http://www.oceanopticsbook.info/view/optical_constituents_of_the_ocean/__level_2/a_new_iop_model_for_case_1_water`.)

- The Sun zenith angle was $\theta_{\mathrm{Sun}} = 17.99$ deg and the Sun's azimuthal angle was east of the nadir point at 84.34 deg from true north.
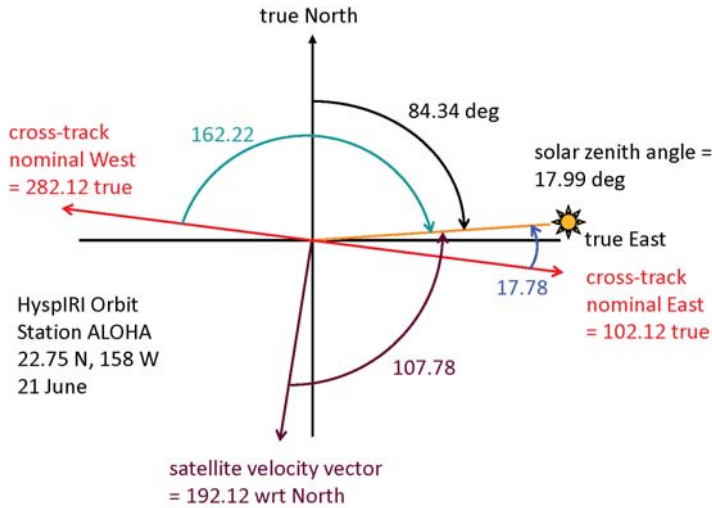
Figure 2.1: Sun and viewing geometry for a mid-day HyspIRI pass over Station ALOHA on 21 June.

- The off-nadir viewing angle was $\theta_v = 30$ deg, $\phi_v = 281.12$ deg, which is at right angles to the satellite's orbital direction and looking to the west side of the orbit, away from the Sun's direction.

- The atmospheric conditions (temperature profile, water vapor, ozone, etc.) were typical of a tropical marine atmosphere (defined via MODTRAN's "Tropical Atmosphere" option). The sky conditions were clear. The aerosols were for an open-ocean marine atmosphere.

- The wind speed was 10 m s^{-1}.

- The wavelength resolution was 10 nm from 350 to 1500 nm.

Figure 2.2 shows various radiances and irradiances obtained from this simulation. The solid curves are values at the TOA, and the dotted curves are the corresponding quantities just above the sea surface. The E_d TOA curve (the solid purple line) is the extraterrestrial solar irradiance (averaged over 10 nm bands) on a surface parallel to the mean sea surface. The dips in the curve below 700 nm are due to absorption by various elements in the Sun's photosphere; these are Fraunhofer lines averaged over the 10 nm bands of this simulation. Above 700 nm, the Sun's irradiance is close to a blackbody spectrum (see http://www.oceanopticsbook.info/view/light_and_radiometry/level_2/light_from_the_sun). The purple dotted line shows how much of the TOA solar irradiance reaches the sea surface. There are large dips in the TOA irradiance that reached the sea surface in the regions around 940 and 1130; these are due to absorption by water vapor, as are the smaller dips near 720 and 820 nm. The large opaque region between 1350 and 1450 nm is due to water vapor and carbon dioxide. The dip at 760 nm is due to absorption by atmospheric oxygen. These absorption features of the Earth's atmosphere will affect any radiation passing through the atmosphere.

The solid blue line shows the TOA radiance L_t that would be measured by a satellite looking in the direction 30 deg West of the nadir point. The orange curve shows how much of the total is atmospheric path radiance, L_{atm}. The aqua and gray curves respectively show how much of

9
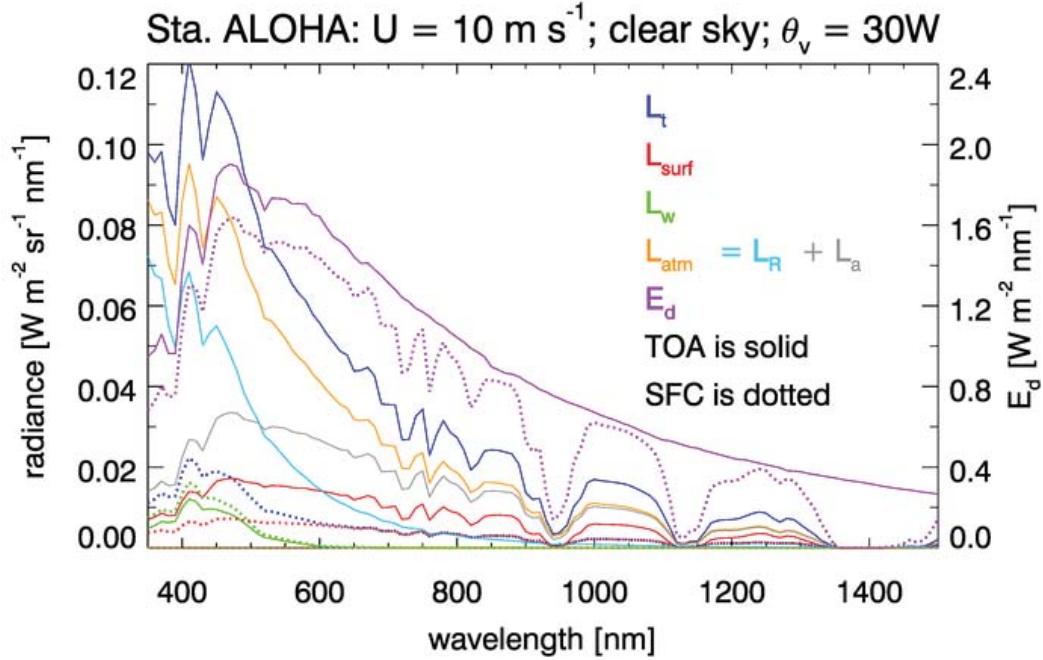
Figure 2.2: Example radiances contributing to the TOA radiance. Solid lines are radiances at the TOA; dotted lines are at the sea surface (SFC). The geometric, atmospheric, and water conditions are described in the text.

the path radiance is due to Rayleigh scattering by atmospheric gases and by aerosols (including aerosol-gas interactions). The green curves in Fig. 2.2 show that the water-leaving radiance at the TOA (the solid curve) is less than the water-leaving radiance just above the sea surface (the dotted curve). This makes intuitive sense, because part of the water-leaving radiance would be lost to atmospheric absorption or scattering into other directions before that radiance reaches the TOA.

The red curves show the total radiances due to surface reflectance, i.e., the sum of the background sky reflectance and the direct Sun glint. However, the red curves show that the surface-reflectance contribution is *greater* at the TOA than at the surface. This seems counterintuitive and requires explanation. In Fig. 1.1 the arrow labeled L_g represents Sun glint due to the occasional wave facet that is tilted in just the right direction to create glint that is seen by the sensor. The arrow labeled L_{gs} represents the very bright glint in the Sun's specular direction; the sensor is looking in the direction away from the Sun's azimuthal direction in order to avoid viewing this specular glint. However, the specular glint gives a strong reflected radiance, some of which is being scattered by the atmosphere into the sensor viewing direction; this is illustrated by the L_{gs2} arrow in Fig. 1.1. The surface contribution in Fig. 2.2 is the sum of the L_{sky}, L_g, and L_{gs2} contributions. If the ocean is viewed from just above the sea surface (the red dotted line), the surface-reflected radiance comes only from reflected sky radiance L_{sky} and a small amount of direct Sun glint L_g from wave facets that are tilted in just the right way to reflect the Sun's direct beam into the direction of the sensor. (This direct Sun glint L_g is minimal because of the choice of viewing direction.) These surface-reflected sky and Sun radiances decrease between the surface and the TOA, just as does the
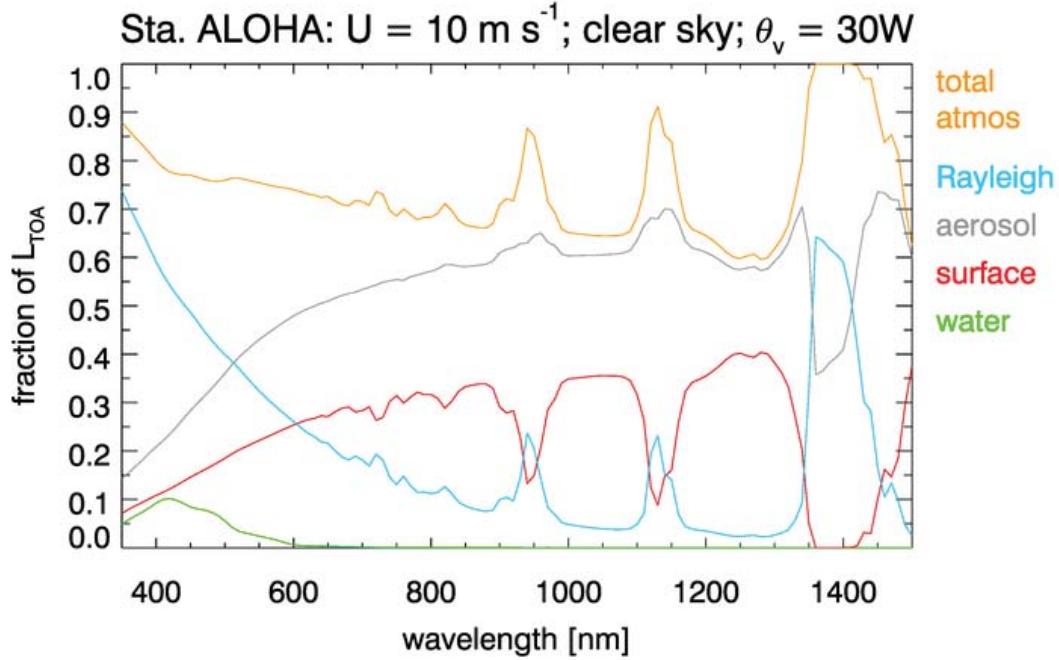
Figure 2.3: The fraction of L_t due to various processes, for the particular simulation of Fig. 2.2. (Need to add a curve for total atmos plus glint.)

water-leaving radiance. However, the total TOA radiance that arises from sea surface reflectance, as partitioned in the simulation, comes from the sum of the surface reflectance in the viewing direction (decreasing with altitude) and the contribution by atmospheric scattering of specular Sun glint into the viewing direction (L_{gs2}, increasing with altitude). The specular radiance L_{gs2} is large in magnitude, so the atmospheric scattering of this radiance into the viewing direction can be significant. If the present simulation is run with a level sea surface, for which there is no L_g Sun glint into the sensor direction, this behavior is still present and, indeed, is even somewhat greater in magnitude. (To fully isolate the effect of specular Sun glint being atmospherically scattered into the sensor, a special run was made in which any photon from the Sun's unscattered beam that was reflected by the sea surface was killed. That is, all Sun glint was forced to be zero. Only photons from the background sky that were reflected by the sea surface were allowed to contribute to the TOA surface-reflected radiance. In that case, the surface-reflected radiance behaves the same as the water-leaving radiance: less sky glint reaches the TOA than leaves the sea surface.)

Figure 2.3 shows the fractional contributions by these various processes to the total TOA radiance L_t. For this particular case, the water-leaving radiance is at most 10% of the total TOA radiance. The atmospheric path radiance contributes 70 to 90% of L_t, with the rest coming from surface glint. Below 500 nm, Rayleigh scattering by atmospheric gases is the largest contributor to the TOA radiance. This is also true in the band from 1350 to 1400 nm, where the atmosphere is essentially opaque, because the aerosols are located mostly near the sea surface. Aerosols are the greatest contributor between 500 and 1350 nm.

Figure 2.4 shows the L_t of Fig. 2.2, plus the corresponding L_t radiances for wind speeds of 0
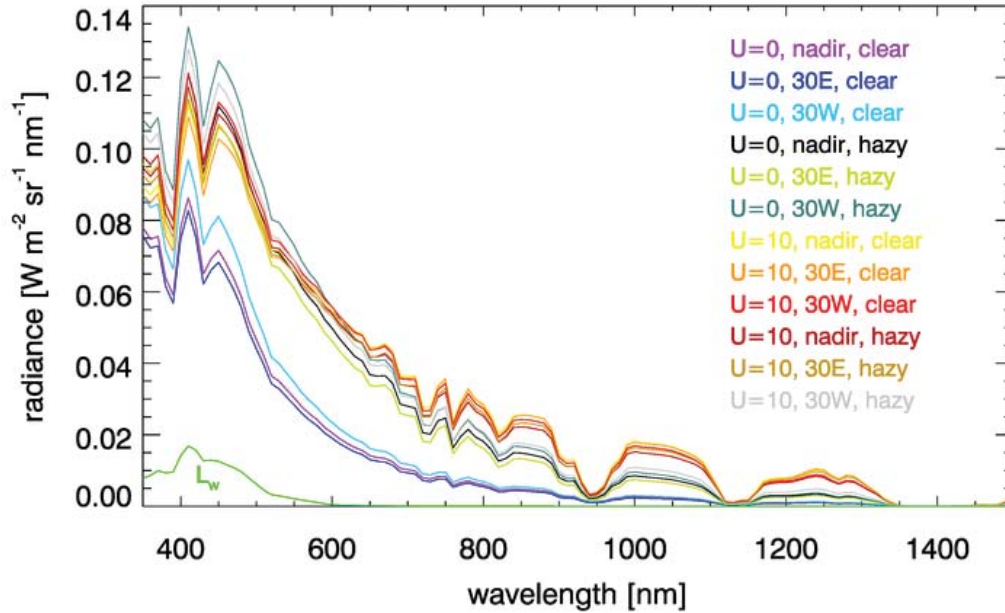
Figure 2.4: Upper curves: TOA radiances for various environmental and viewing conditions as labeled. Each TOA radiance has the same water-leaving radiance L_w, which is shown by the green curve.

and 10 m s^{-1}, clear and hazy atmospheric conditions, and viewing directions of 0 (nadir) and 30 deg East or West of the flight direction. (These simulations are discussed in detail at http://www. oceanopticsbook.info/view/remote_sensing/the_atmospheric_correction_problem.) Each of these much-different TOA radiances has essentially the same water-leaving radiance L_w, which is shown in green. The atmospheric correction problem can be visually summarized as follows: Given any of these TOA spectra and the geometry (Sun location and viewing direction), recover the water-leaving radiance specrum L_w. This is clearly a difficult problem because the needed atmospheric conditions (aerosol type and concentration in particular) are not obtained as part of the L_t measurement.

Normalized Reflectances

Ocean-color remote sensing algorithms usually work with remote-sensing reflectances or normalized water-leaving reflectances. The calculation and interpretation of those quantities are discussed in detail in this section.

The ratio of water-leaving radiance L_w to incident sky irradiance E_d is an apparent optical property (AOP) that has only weak dependence on external parameters such as solar zenith angle and sky conditions, but which is strongly correlated with water-column inherent optical properties (IOPs). However, the remote-sensing reflectance $R_{rs} \equiv L_w/E_d$ still does depend somewhat on the atmospheric and other conditions at the time of measurement and thus, strictly speaking, is tied to the particular time and location of the observation. (Further discussion and examples are given at `http://www.oceanopticsbook.info/view/overview_of_optical_oceanography/reflectances`.)

It would be desirable to have an AOP that completely removes the effects of solar zenith angle, viewing direction, atmospheric conditions, and sea state, while retaining a strong dependence on the water IOPs. It would then be possible to compare this AOP for measurements made at different times and/or locations, and thereby extract information about the differences in the water columns for the different measurements. Even for measurements made at the same time and location, normalization to a common set of conditions is needed, e.g., when comparing in situ measurements having different viewing directions. Such an AOP is obtained via the concept of the normalized water-leaving reflectance.

3.1   Normalized Radiances and Reflectances

Let $L_u(z, \theta_s, \theta_v, \phi)$ be the in-water, upwelling radiance at depth z, for a Sun zenith angle of θ_s and a viewing direction of θ_v, ϕ. Polar viewing direction $\theta_v = 0$ indicates a direction looking at the nadir, detecting radiance traveling toward the zenith. The azimuthal angle ϕ is measured relative to the Sun's azimuthal direction. $L_w(\theta_s, \theta_v, \phi)$ denotes the corresponding water-leaving radiance, which is measured just above the sea surface. These radiances depend strongly on wavelength, which is not shown. In practice, L_u is measured by instruments in the water. L_w can be obtained by atmospheric correction of a radiance measured at the top of the atmosphere, from an above-surface measurement at sea level after correction for surface reflectance, or from an in-water measurement

of L_u extrapolated upward through the sea surface.

One goal of normalization is to transform a satellite-based measurement of top-of-the-atmosphere radiance L_t into something that can be compared with a standard measurement made in situ, in the ocean, for whatever Sun zenith angle, viewing direction, atmospheric conditions, and wave state occurred at the time of the satellite measurement. Let this standard in situ measurement be the nadir-viewing radiance measured just below the sea surface, $L_\mathrm{u}(0^-, \theta_\mathrm{v} = 0)$. Depth $z = 0^-$ refers to a location in the water just below the sea surface; 0^+ refers to a location in the air just above the sea surface. Dividing $L_\mathrm{u}(0^-, \theta_\mathrm{v} = 0)$ by the downwelling plane irradiance within the water, $E_\mathrm{d}(0^-)$, gives the in-water Remote Sensing Ratio RSR:

$$RSR \equiv \frac{L_\mathrm{u}(0^-, \theta_\mathrm{v} = 0)}{E_\mathrm{d}(0^-)} \ . \tag{3.1}$$

The division of $L_\mathrm{u}(0^-, \theta_\mathrm{v} = 0)$ by $E_\mathrm{d}(0^-)$ removes the "zeroth order" effect of solar zenith angle θ_s and the "first order" atmospheric effects (including aerosol effects) on the magnitude of $L_\mathrm{u}(0^-, \theta_\mathrm{v} = 0)$. We now want to transform L_t into something comparable.

In the early days of satellite remote sensing, it was sometimes assumed that the upwelling underwater radiance distribution is isotropic. Under that assumption, RSR is approximately what you would get if the Sun were at the zenith and there were no atmosphere (i.e., the sky were black). This was the origin of statements that the normalized water-leaving radiance is the water-leaving radiance "which would exit the sea surface if the Sun were at the zenith and if the atmosphere were absent" (Gordon et al., 1988, page 10,910).

Fig. 3.1 compares upwelling and water-leaving radiances for "no atmosphere" or "black sky" vs. realistic sky conditions. The curves of this figure were generated using HydroLight with the Sun placed at the zenith. The sky was either black (a collimated incident sky radiance) or had a diffuse radiance angular distribution typical of a clear sky. The water IOPs were determined using the same "new Case 1" bio-optical model as for the simulations of the previous section. Runs were made for chlorophyll values of 0.05, 0.5 and 5 mg m^{-3}. The runs were at a wavelength of 550 nm and the sea surface was level. Each radiance is normalized by its value at the nadir-viewing direction to isolate the differences in the shapes of the curves. The upper set of curves shows the shape of the upwelling radiances L_u just below the sea surface as functions of the in-water, off-nadir viewing angle θ_v' at right angles ($\phi = 90$ deg) to the solar plane. The lower set of curves (those curving downward in the figure) shows the corresponding water-leaving radiances L_w as functions of the in-air, off-nadir viewing angle θ_v. For a level sea surface, these in-water and in-air angles are related by Snel's law $\sin\theta_\mathrm{v} = n_w \sin\theta_\mathrm{v}'$, where $n_w \approx 1.34$ is the water index of refraction. Although the differences in the black-sky and real-sky radiances are only a few percent over the range of angles relevant to most remote sensing ($\theta_\mathrm{v} \lesssim 60$ deg), differences of this magnitude are significant given the high accuracy requirements for retrieved water-leaving radiances in ocean remote sensing.

The observation that the upwelling radiance distribution depends on the sky radiance distribution indicates that the idea of removing the atmosphere is too extreme. Morel and Gentili (1996, page 4852) therefore revised the definition of normalized water-leaving radiance to be "...the radiance that could be measured by a nadir-viewing instrument, if the Sun were at the zenith in the absence of any atmospheric loss, and when the Earth is at its mean distance from the Sun." *The distinction between "atmosphere were absent" (i.e., a vacuum) and "absence of any atmospheric*
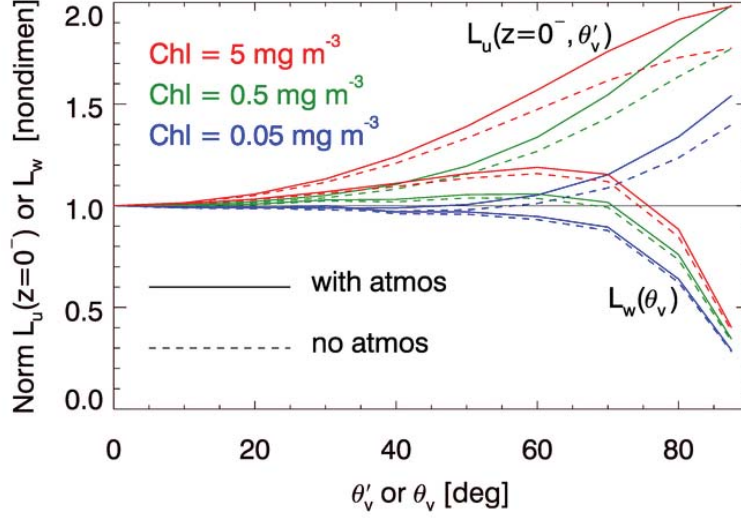
Figure 3.1: Comparisons of $L_{\mathrm{u}}(z = 0^-, \theta_{\mathrm{s}} = 0, \theta'_{\mathrm{v}}, \phi = 90)$ and $L_{\mathrm{w}}(\theta_{\mathrm{s}} = 0, \theta_{\mathrm{v}}, \phi = 90)$ for a zenith Sun in a black sky (no atmosphere; dashed lines) vs. a zenith Sun in a typical atmosphere (solid lines). The colors identify the chlorophyll concentrations. The black line at an ordinate value of 1 corresponds to an isotropic radiance distribution.

loss" (i.e., no attenuation by the atmosphere) is fundamental to understanding the developments of this section.

The normalization proceeds as follows. The first step is to account for solar zenith angle and atmospheric attenuation effects on $L_{\mathrm{w}}(\theta_{\mathrm{s}}, \theta_{\mathrm{v}}, \phi)$ via (e.g., Gordon et al. (1988, page 10,910) or Gordon and Wang (1994b, Eq. 4)):

$$[L_{\mathrm{w}}(\theta_{\mathrm{v}}, \phi)]_{\mathrm{N}} \equiv \frac{L_{\mathrm{w}}(\theta_{\mathrm{s}}, \theta_{\mathrm{v}}, \phi)}{\cos\theta_{\mathrm{s}}\, t(\theta_{\mathrm{s}})},$$

where $t(\theta_{\mathrm{s}})$ is the atmospheric diffuse transmittance for irradiance in the Sun's direction for the given atmospheric conditions. Recent papers include an explicit factor to correct L_{w} for the Earth-Sun distance at the time of measurement:

$$[L_{\mathrm{w}}(\theta_{\mathrm{v}}, \phi)]_N \equiv \left(\frac{R}{R_{\mathrm{o}}}\right)^2 \frac{L_{\mathrm{w}}(\theta_{\mathrm{s}}, \theta_{\mathrm{v}}, \phi)}{\cos\theta_{\mathrm{s}}\, t(\theta_{\mathrm{s}})}. \tag{3.2}$$

Here R is the Earth-Sun distance at the time of measurement, and R_{o} is the mean Earth-Sun distance. The $(R/R_{\mathrm{o}})^2$ factor corrects the L_{w} measurement to what it would be at the mean Earth-Sun distance. (The solar irradiance at the TOA varies by about 8% over the course of a year due to the Earth's elliptical orbit.)

$[L_{\mathrm{w}}(\theta_{\mathrm{v}}, \phi)]_{\mathrm{N}}$ is called the *normalized water-leaving radiance*. It is the water-leaving radiance that would occur if the earth were at the mean Earth-Sun distance, the Sun were at the zenith, and the atmosphere were non-attenuating. Note that although the factors of $(R/R_{\mathrm{o}})^2$, $\cos\theta_{\mathrm{s}}$, and $t(\theta_{\mathrm{s}})$ largely remove the effects of Earth-Sun distance, solar zenith angle, and atmospheric attenuation,

respectively, on the measured L_w, the normalized water-leaving radiance still refers to a particular viewing direction and depends on the sky angular radiance distribution at the time of observation.

Multiplying the $[L_w(\theta_v, \phi)]_N$ of Eq. (3.2) by a factor of π/F_o, where π has units of steradian and F_o is the extraterrestrial solar irradiance at the mean Earth-Sun distance, gives the *nondimensional normalized water-leaving reflectance* $[\rho_w]_N$ (e.g. Gordon and Wang, 1994b, page 7756):

$$[\rho_w(\theta_v, \phi)]_N \equiv \frac{\pi}{F_o}[L_w(\theta_v, \phi)]_N = \pi \frac{\left(\frac{R}{R_o}\right)^2 L_w(\theta_s, \theta_v, \phi)}{F_o \cos\theta_s\, t(\theta_s)}\,. \qquad (3.3)$$

(Radiant energy is a physical quantity that propagates through space and that can leave the water. Radiance is a derived physical quantity that likewise can leave the water, so it makes sense to speak of the "water-leaving radiance." Reflectance, however, is a property of a surface. Reflectance does not propagate through space and it cannot leave a surface, so it does not make sense to speak of the "water-leaving reflectance." However, the term "water-leaving reflectance" is well established shorthand for "reflectance based on the water-leaving radiance and the incident irradiance," and we will use the term even if it is linguistically somewhat improper.)

The *remote-sensing reflectance* R_{rs} is usually defined as

$$R_{rs}(\theta_s, \theta_v, \phi) \equiv \frac{L_w(\theta_s, \theta_v, \phi)}{E_d(0^+, \theta_s)}\,. \qquad (3.4)$$

In this definition, both L_w and E_d are values for the Earth-Sun distance at the time of measurement. However, this R_{rs} is numerically the same as what would be obtained if both L_w and E_d were corrected to the mean Earth-Sun distance by $(R/R_o)^2$ factors applied to each, because the correction factors on L_w and E_d cancel out. That is to say, the irradiance at the sea surface for Earth-Sun distance R is

$$E_d(0^+, \theta_s) = F_o \left(\frac{R_o}{R}\right)^2 \cos\theta_s\, t(\theta_s)\,. \qquad (3.5)$$

It thus follows that

$$[\rho_w(\theta_v, \phi)]_N = \pi \frac{\left(\frac{R}{R_o}\right)^2 L_w(\theta_s, \theta_v, \phi)}{F_o \cos\theta_s\, t(\theta_s)} = \pi \frac{L_w(\theta_s, \theta_v, \phi)}{E_d(\theta_s)} = \pi R_{rs}(\theta_v, \phi)\,. \qquad (3.6)$$

Another way to view $[\rho_w]_N$ is to think of it as the bidirectional reflectance distribution function (BRDF) of the ocean normalized by the BRDF of a perfectly reflecting Lambertian surface. The BRDF of a surface as measured in the laboratory is the radiance reflected by the surface divided by the incident plane irradiance onto the surface. The BRDF of a Lambertian surface whose irradiance reflectance is $\mathcal{R}$ is $\mathcal{R}/\pi$, with units of inverse steradian. For a perfect Lambertian reflector, $\mathcal{R} = 1$, and

$$[\rho_w]_N = \frac{BRDF_{ocean}}{BRDF_{Lamb}} = \frac{L_w/E_d}{1/\pi} = \pi R_{rs}\,.$$

This makes it clear that the π carries units of solid angle, so that $[\rho_w]_N$ is nondimensional.

3.2 The BRDF Effect

As noted above, the normalizations contained in $[\rho_w(\theta_v, \phi)]_N$ or $R_{rs}(\theta_v, \phi)$ remove the effects of solar zenith angle, atmospheric attenuation, and Earth-Sun distance on a measured radiance L_w. However, $[\rho_w(\theta_v, \phi)]_N$ still refers to a particular viewing direction (θ_v, ϕ). This dependence ties $[\rho_w(\theta_v, \phi)]_N$ to the angular distribution of the upwelling underwater radiance and to the transmittance through the sea surface from water to air (which depends on the wave state, i.e., on the wind speed). The upwelling underwater radiance in turn depends on the angular distribution of the incident sky radiance, surface transmittance from air to water, and to the absorbing and scattering properties of the water body (the scattering phase function in particular). The dependence of the upwelling radiance distribution on the sky radiance distribution, viewing geometry, and water optical properties is commonly called the BRDF effect. The final step is to remove the BRDF effect to the greatest extent possible.

The BRDF effect was studied by Morel and colleagues in a series of papers (Morel and Gentili, 1991, 1993, 1996) culminating in Morel et al. (2002). They used numerical radiative transfer models to compute correction factors that would transform a measurement made for a particular Sun zenith angle, viewing direction, wind speed, atmospheric conditions, and water IOPs into a measurement that corresponds to a zenith Sun and nadir viewing direction *for a typical marine atmosphere and for Case 1 water with a given chlorophyll value.* The correction involves three separate factors, $\mathfrak{R}$, f, and Q, as follows.

Let $\mathfrak{R}(\theta_v', W)$ be a nondimensional factor that accounts for all transmission and reflection effects by the wind-blown sea surface when $E_d(0^+)$ is transmitted downward through the surface to give $E_d(0^-)$, and $L_u(0^-, \theta_v', \phi)$ is transmitted upward through the surface to give $L_w(0^+, \theta_v, \phi)$. Polar angle θ_v' (measured from the nadir) is the underwater angle that is refracted by the surface into the above-surface viewing direction θ_v of the water-leaving radiance $L_w(\theta_v, \phi_v)$. W is the wind speed. $\mathfrak{R}(\theta_v', W)$ depends on the wind speed (i.e., the surface wave state) and the water index of refraction via the Snel's law mapping of θ_v' to θ_v. However, Gordon (2005) showed that the dependence of $\mathfrak{R}(\theta_v', W)$ on wind speed is very weak, and usually $\mathfrak{R}$ can be computed with adequate accuracy over a wide range of viewing angles using $W = 0$. The detailed derivation of $\mathfrak{R}(\theta_v', W)$ in Morel and Gentili (1996, Eq. 5 and Appendix D) shows that, strictly speaking, $\mathfrak{R}$ also depends on the solar zenith angle and the angular distribution of the incident atmospheric radiance, which affect how much incident irradiance is transmitted through the sea surface. Likewise, $\mathfrak{R}$ depends on the water IOPs via the in-water irradiance reflectance $R(0^+) = E_u(0^+)/E_d(0^+)$. However, these dependencies are weak compared to the directional (θ_v') dependency and so, for compactness and consistency with Morel's notation, are not shown as arguments.

Let $\mathfrak{R}_o(W)$ be the reference value of $\mathfrak{R}(\theta_v', W)$ corresponding to transmission normal to the mean sea surface $(\theta_v = \theta_v' = 0)$. Multiplying the $[L_w(\theta_v)]_N$ of Eq. (3.2) by $\mathfrak{R}_o(W)/\mathfrak{R}(\theta_v', W)$ corrects for surface-transmission effects for the actual viewing direction θ_v' and wind speed W. For $\theta_v' \approx 0$, $\mathfrak{R}_o \approx 0.53$; $\mathfrak{R}_o$ is greater than 0.52 out to angles of 50 deg. Note that Figure 4 of Morel et al. (2002), which shows ratios of $\mathfrak{R}_o(W)/\mathfrak{R}(\theta_v', W)$, was incorrectly computed; see the discussion and revised figures in Gordon (2005).

The dimensionless factor f is defined by $E_u(0^-)/E_d(0^-) \equiv f \times (b_b/a)$, where a and b_b are the water absorption and backscatter coefficients respectively. This factor parameterizes how down-

17

welling irradiance in the water is converted to upwelling irradiance by backscatter and reduced by absorption. That is to say, f relates the irradiance reflectance within the water to the most relevant IOPs. f values are in the range of 0.3 to 0.5 (Morel and Gentili, 1996, Fig. 2).

The factor $Q \equiv E_u(0^-)/L_u(0^-)$ (units of steradian) describes the angular distribution of the upwelling radiance. $Q = \pi$ sr for an isotropic upwelling radiance distribution; actual in-water radiance distributions typically have Q values in the range of 3 to 6 sr (Morel and Gentili, 1996, Fig. 3).

In practice, f and Q are combined to give a term that has less variability than the individual factors. The combined factor $f/Q \equiv L_u(0^-, \theta'_v, \phi)/E_d(0^-)$ describes how the downwelling irradiance just beneath the sea surface is reflected back upward as upwelling radiance in the direction (θ'_v, ϕ). The f/Q term thus describes both the efficiency of conversion of downwelling irradiance into upwelling radiance, and the angular (non-isotropic) distribution of the upwelling underwater radiance that generates the water-leaving radiance. f/Q values are typically in the range to 0.07 to 0.15 (Morel and Gentili, 1996, Fig. 6). Let f_o/Q_o refer to the ratio for the nadir viewing direction and Sun at the zenith.

Multiplying $[L_w(\theta_v, \phi)]_N$ by $(f_o/Q_o)/(f/Q)$ corrects for the difference of the actual angular distribution of the upwelling radiance and what that distribution would be for the Sun at the zenith, nadir viewing, *for the particular atmospheric and oceanic conditions used to compute f and Q.*

Applying these BRDF corrections to the $[L_w(\theta_v, \phi)]_N$ of Eq. (3.2) gives (Morel et al., 2002, Eq. 13):

$$[L_w]_N^{ex} \equiv [L_w(\theta_v, \phi)]_N \frac{\mathfrak{R}_o(W)}{\mathfrak{R}(\theta'_v, W)} \frac{f_o(\mathrm{ATM}, W, \mathrm{IOP})}{Q_o(\mathrm{ATM}, W, \mathrm{IOP})} \left[\frac{f(\theta_s, \mathrm{ATM}, W, \mathrm{IOP})}{Q(\theta_s, \theta'_v, \phi, \mathrm{ATM}, W, \mathrm{IOP})} \right]^{-1}. \qquad (3.7)$$

Morel et al. call $[L_w(\lambda)]_N^{ex}$ the "exact normalized water-leaving radiance". The arguments "ATM" and "IOP" refer to the specific set of atmospheric conditions and water inherent optical properties used to compute f and Q. (As previously noted, these arguments are omitted from the $\mathfrak{R}$ terms because the ATM and IOP dependencies are small for $\mathfrak{R}$.) This $[L_w(\lambda)]_N^{ex}$ is equivalent to the normalization seen in Franz et al. (2007, Eq. 2), except for a sensor-specific correction factor for out-of-band wavelength response. It should be noted that the f_o/Q_o factor has arguments of $(\mathrm{ATM}, W, \mathrm{IOP})$ because those values correspond to the same atmospheric and oceanic conditions as the f/Q factor; the difference is that f_o/Q_o corresponds to $\theta_s = 0$ and $\theta'_v = 0$. Values of the $(\mathfrak{R}_o/\mathfrak{R})(f_o/Q_o)/(f/Q)$ product are typically in the 0.6 to 1.2 range, depending on the IOPs, solar zenith angle, atmospheric conditions, wind speed, and wavelength.

It is noted that the wind speed at the time of observation, W, is shown in both the $\mathfrak{R}_o$ and (f_o/Q_o) terms in Eq. (3.7). It can be argued that these terms should use a reference value of $W = 0$, so that all quantities are referred to a level sea surface. However, as presently implemented by the OBPG, the same wind speed W is used in the reference terms.

The atmospheric conditions used to compute the f/Q factors were typical of marine atmospheres and are summarized as follows (Morel and Gentili, 1996; Morel et al., 2002):

- The atmosphere was modeled as 50 layers, each 1 km thick

- The aerosol optical thickness was $\tau_a = 0.2$ at 550 nm.

18

- The tropospheric aerosols had a relative humidity of 70% and were distributed in the upper 45 atmospheric layers

- The marine aerosols had a relative humidity of 90% and were distributed in the lower 5 atmospheric layers

- The aerosol phase functions were modeled using Mie theory and the data of Shettle and Fenn (1979)

- The sea surface was modeled using a Gaussian distribution of wave slopes based on the empirical wind-speed, wave-slope data of Cox and Munk (1954, page 847) for the given wind speed W. W was taken to be 0 for the Q calculations, although there are still some residual capillary waves according to the empirical slope data of Cox and Munk.

The water optical properties were obtained from bio-optical models for Case 1 water, for which the IOPs can all be parameterized by the chlorophyll concentration Chl. In particular, the scattering phase function was computed as a chlorophyll-weighted sum of phase functions for "small" and "large" particles, which themselves were computed using T-matrix theory for non-spherical particles with different size distributions. The details of the IOP bio-optical models are given in Morel et al. (2002).

The radiative transfer calculations were carried out using a Monte Carlo code for calculation of the $\mathfrak{R}$ factors, and using HydroLight for the f/Q calculations. The $\mathfrak{R}$ are tabulated for an exactly level sea surface and for wind speeds of $W = 0, 4, 10$ and 16 m s^{-1}; the $W = 0$ values include a small amount of residual capillary waves because the Cox-Munk mean square sea surface slopes are not extactly zero for a zero wind speed. The f/Q calculations were done both with and without Raman scattering by water. None of the calculations included polarization. These codes were run for

- 7 wavelengths (412.5, 442.5, 490, 510, 560, 620, and 660 nm)

- 6 chlorophyll values ($Chl = 0.03, 0.1, 0.3, 1.0, 3.0$ and 10 mg m^{-3}). The water was homogeneous.

- 6 solar zenith angles ($\theta_s = 0, 15, 30, 45, 60$ and 75 deg)

- 13 azimuthal angles ($\phi = 0$ to 180 deg by steps of 15 deg)

- 17 nadir angles ($\theta'_v = 1.078, 3.411, 6.289, 9.278, 12.300, 15.330, 18.370, 21.410, 24.450, 27.500, 30.540, 33.590, 36.640, 39.690, 42.730, 45.780,$ and 48.830 deg)

These runs give a total of $7 \times 6 \times 6 \times 13 \times 17 = 55,629$ f/Q values, which are organized into $7 \times 6 \times 6 = 252$ tables, each with 13 columns and 17 rows. A separate table gives values of $\mathfrak{R}(\theta'_v, W)$ at θ'_v increments of 1 deg and for wind speeds of $W = 0, 4, 10$ and 16 m s^{-2}. The tables including Raman effects are available at ftp://oceane.obs-vlfr.fr/pub/gentili/AppliedOptics2002/.

Use of these tables requires the chlorophyll concentration, which is not *a priori* known. In the initial study (Morel and Gentili, 1996), a band-ratio algorithm was used to obtain an initial guess for Chl. That value was then used in the tables to obtain the BRDF correction factors. Those factors give a new estimate of $[L_w(\lambda)]_N^{ex}$, which can be used to obtain an new value of Chl, and so

on. However, the tables are not tied to how the *Chl* value is obtained, so in practice any algorithm can be used to obtain *Chl* values from the reflectances in an iterative process.

Finally, the exact normalized water-leaving radiance of Eq. (3.7) is used in Eq. (3.3) to obtain the *exact normalized water-leaving reflectance*:

$$[\rho_{\mathrm{w}}]_{\mathrm{N}}^{\mathrm{ex}} \equiv \frac{\pi}{F_{\mathrm{o}}}[L_{\mathrm{w}}]_{\mathrm{N}}^{\mathrm{ex}} \tag{3.8}$$

$$= \left\{ \frac{\pi}{F_{\mathrm{o}}\cos\theta_{\mathrm{s}}\,t(\theta_{\mathrm{s}})} \frac{\mathfrak{R}_{\mathrm{o}}(W)}{\mathfrak{R}(\theta_{\mathrm{v}}',W)} \frac{f_{\mathrm{o}}(\mathrm{ATM},W,\mathrm{IOP})}{Q_{\mathrm{o}}(\mathrm{ATM},W,\mathrm{IOP})} \left[\frac{f(\theta_{\mathrm{s}},\mathrm{ATM},W,\mathrm{IOP})}{Q(\theta_{\mathrm{s}},\theta_{\mathrm{v}}',\phi,\mathrm{ATM},W,\mathrm{IOP})} \right]^{-1} \right\} \times$$

$$L_{\mathrm{w}}(\theta_{\mathrm{s}},\theta_{\mathrm{v}},\phi)\,. \tag{3.9}$$

The quantities in brackets can all be obtained from pre-computed look-up-tables given the Sun and viewing geometry, wavelength, atmospheric conditions used to obtain $L_{\mathrm{w}}(\theta_{\mathrm{s}},\theta_{\mathrm{v}},\phi)$ from $L_{\mathrm{t}}(\theta_{\mathrm{s}},\theta_{\mathrm{v}},\phi)$ (used to determine $t(\theta_{\mathrm{s}})$), and the chlorophyll concentration. The chlorophyll concentration determines the IOPs according to the bio-optical models for Case 1 water used in the Morel et al. calculations.

Although Morel and others call $[L_{\mathrm{w}}]_{\mathrm{N}}^{\mathrm{ex}}$ the "exact" normalized water-leaving radiance, and $[\rho_{\mathrm{w}}]_{\mathrm{N}}^{\mathrm{ex}}$ the "exact" normalized water-leaving reflectance, it must be remembered that these quantities are exact only if the atmosphere and ocean have exactly the same absorbing and scattering properties as used in the model simulations upon which the BRDF correction factors are based. That will of course not in general be the case. In Case 1 waters, the differences between the Morel et al. Case 1 IOP model and the actual ocean IOPs are often small enough that the BRDF-corrected quantities are sufficiently accurate for remote sensing. However, the differences can become large in Case 2 waters. Research therefore continues on ways to improve the BRDF correction, both to extend its validity to Case 2 water and to remove the need to estimate the chlorophyll concentration in order to use the look-up tables (e.g., Lee et al., 2011; Fan et al., 2016). Although further improvements can be anticipated, the BRDF correction as described above remains the OPBG operational algorithm at the time of this writing.

The OBPG works with radiance to get to $[L_{\mathrm{w}}]_{\mathrm{N}}^{\mathrm{ex}}$. However, when doing atmospheric correction on TOA radiances, the various look-up-tables used for Rayleigh correction, etc. are in terms of reflectances $[\rho_{\mathrm{w}}]_{\mathrm{N}}^{\mathrm{ex}}$. Equation (3.8) allows easy conversion from one to the other, depending on which quantity is most convenient for a given step of the atmospheric correction process.

It is to be noted that the "remote-sensing reflectance" reported by the NASA OBPG as a standard Level 2 product of the NASA ocean color satellites such as MODIS and VIIRS is the exact normalized water-leaving reflectance of Eq. (3.9), divided by π:

$$R_{\mathrm{rs}}(\mathrm{NASA}) = \frac{[\rho_{\mathrm{w}}]_{\mathrm{N}}^{\mathrm{ex}}}{\pi} = \frac{[L_{\mathrm{w}}]_{\mathrm{N}}^{\mathrm{ex}}}{F_{\mathrm{o}}}\,. \tag{3.10}$$

However, the "remote-sensing reflectance" computed by HydroLight is $R_{\mathrm{rs}}(\theta_{\mathrm{s}},\theta_{\mathrm{v}},\phi)$ as defined by Eq. (3.4). A given HydroLight run computes $R_{\mathrm{rs}}(\theta_{\mathrm{s}},\theta_{\mathrm{v}},\phi)$ for all viewing directions θ_{v},ϕ for the given θ_{s} and other conditions of wind speed, IOPs, and atmospheric radiance distribution. Thus the HydroLight R_{rs} outputs for various viewing directions incorporate the BRDF effects. (Indeed, comparison of HydroLight-computed $R_{\mathrm{rs}}(\theta_{\mathrm{s}},\theta_{\mathrm{v}},\phi)$ values with HydroLight values for a zenith Sun and nadir viewing direction is how the f/Q BRDF factors were determined in the Morel et al.

studies.) Thus there is no need for an explicit BRDF correction to the HydroLight-computed $R_{\rm rs}$. *If a HydroLight run has the Sun at the zenith, then the nadir-viewing HydroLight $R_{\rm rs}$ times π corresponds to $[\rho_{\rm w}]_{\rm N}^{\rm ex}$:*

$$[\rho_{\rm w}]_{\rm N}^{\rm ex} = \pi R_{\rm rs}({\rm HydroLight}; \theta_{\rm s} = 0, \theta_{\rm v} = 0) . \tag{3.11}$$

Recalling Eq. (3.10), this gives

$$R_{\rm rs}({\rm NASA}) = R_{\rm rs}({\rm HydroLight}; \theta_{\rm s} = 0, \theta_{\rm v} = 0) . \tag{3.12}$$

There should be only a very small difference in HydroLight's $\pi R_{\rm rs}$ and $[\rho_{\rm w}]_{\rm N}^{\rm ex}$, attributable to any differences in the angular distributions of the sky radiances used to compute the Morel BRDF factors and as used in HydroLight. Morel et al. (2002, page 6295) notes that these differences are negligible.

It should be noted that HydroLight $R_{\rm rs}$ values are valid for whatever IOPs were used in the run; there is no restriction to homogeneous Case 1 water and no need to estimate a chlorophyll concentration as must be done when applying the Morel BRDF factors. Thus *HydroLight can give a very general $[\rho_{\rm w}]_{\rm N}^{\rm ex}$ via Eq. (3.11), without the assumptions made by Morel et al. when developing the BRDF correction factors seen in Eq. (3.9).*

Figure 3.2 illustrates the magnitudes of the corrections to $\pi R_{\rm rs}(\theta_{\rm s}, \theta_{\rm v}, \phi)$ values. HydroLight was first run to generate remote-sensing reflectances for a Sun zenith angle of $\theta_{\rm s} = 50$ deg, with the Sun in a clear sky. The water IOPs and chlorophyll values were the same as those used for Fig. 3.1. The runs included Raman scatter by water and fluorescence by chlorophyll and CDOM. The dashed lines in Fig. 3.2 show the values of $\pi R_{\rm rs}(\theta_{\rm s} = 50, \theta_{\rm v} = 30, \phi = 90)$. These viewing angles correspond to a sensor viewing the ocean at an off-nadir angle of 30 deg at right angles to the solar plane. The HydroLight runs were then repeated with the Sun at the zenith. The solid lines in the figures show the resulting values of $[\rho_{\rm w}]_{\rm N}^{\rm ex}$ as determined by Eq. (3.11). Depending on the water IOPs, Sun zenith angle, viewing direction, and wavelength, the normalization can change a spectrum by tens of percent, or almost not at all. The changes tend to be greatest in high-chlorophyll waters, at large solar zenith angles, and at large off-nadir viewing angles.

When formulated in terms of reflectances, the partitioning of Eq. (1.3) becomes (e.g., Gordon and Wang, 1994a)

$$\rho_{\rm t} = \rho_{\rm R} + [\rho_{\rm a} + \rho_{\rm Ra}] + T\rho_{\rm g} + t\rho_{\rm wc} + t\rho_{\rm w} , \tag{3.13}$$

where the terms correspond to those of Eq. (1.3). A similar equation applies to the reflectance form of Eq. (1.4).

Figure 3.3 shows the radiances of Fig. 2.2 recast as normalized reflectances. It should be noted in Fig. 3.3 that the solar-spectrum features (most noticeable below 600 nm) seen in the TOA $E_{\rm d}$ spectrum of Fig. 2.2 are removed by the normalization process. However, the atmospheric absorption features (most noticeable beyond 600 nm) remain in the TOA reflectances, but are not present in the surface reflectances. Thus the dotted curves for $\rho_{\rm t}$, $\rho_{\rm g}$, and $\rho_{\rm w}$, are very smooth functions of wavelength. The surface glint reflectance spectrum $\rho_{\rm g}$ is almost independent of wavelength, whereas the surface glint radiance seen in Fig. 2.2 depends of wavelength in the same manner as the surface irradiance spectrum. (Note that the glint reflectance $\rho_{\rm g}$ considered here is not the same at the surface radiance reflectance factor ρ of Mobley (1999, Eq. 4) and Mobley (2015), which is a ratio of incident to reflected sky radiances for the given wind speed, and Sun and viewing directions.)

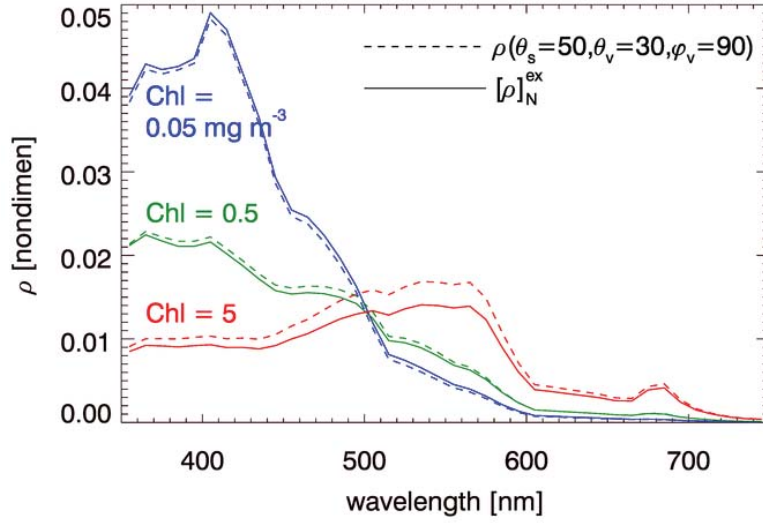Figure 3.2: Comparison of exact normalized water-leaving reflectances $[\rho_w]_N^{ex}$ (solid lines) with unnormalized reflectances (dashed lines) for $\theta_s = 50, \theta_v = 30, \phi = 90$. The color identifies the chlorophyll values of 0.05, 0.5, and 5 mg m^{-3}.
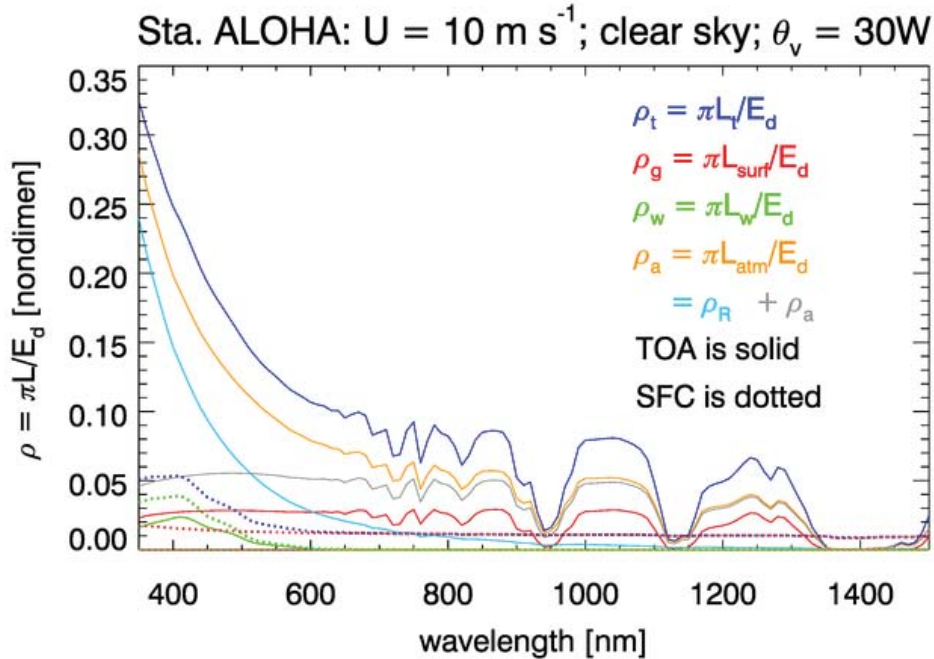

Figure 3.3: Normalized reflectances corresponding to the radiances of Fig. 2.2. These reflectances are $[\rho]_N$, not $[\rho]_N^{ex}$.

3.3 Summary

The *interpretation* of $[\rho_w]_N^{ex}$ as developed above can be summarized as follows:

- Start with a measured $L_w(\theta_s, \theta_v, \phi)$. Then

- The division by $\cos\theta_s$ in Eq. (3.2) moves the Sun to the zenith.

- The division by $t(\theta_s)$ in Eq. (3.2) rescales the radiance magnitude to account for atmospheric attenuation, but the angular distribution of the radiance is unchanged. This diffuse transmission is for the actual atmosphere at the time of observation.

- The $(R/R_o)^2$ factor in Eq. (3.2) corrects for the Earth-Sun distance.

- The BRDF factors in Eq. (3.7) normalize L_w as measured for the actual atmospheric and in-water radiance distributions to *what L_w would be for a reference atmospheric radiance distribution* and *for Case 1 water with the given chlorophyll value.*

The proposed atmospheric retrieval accuracy requirements for the PACE (Pre-Aerosol, Clouds, and ocean Ecosystem) mission are (Franz, 2015)

- for $[\rho]_N^{ex}$ in the 350-400 nm range, a maximum error of 0.002 or 10%

- for $[\rho]_N^{ex}$ in the 400-710 nm range, a maximum error of 0.001 or 5%

In terms of $R_{rs} = [\rho]_N^{ex}/\pi$, this gives

- for R_{rs} in the 350-400 nm range, a maximum error of 6×10^{-4} sr^{-1}

- for R_{rs} in the 400-710 nm range, a maximum error of 3×10^{-4} sr^{-1}

Given that the water-leaving radiance L_w is at most 10% of the TOA radiance (e.g., Fig. 2.3), a requirement for a 5% maximum error in L_w (expressed as the same percentage error in $[\rho]_N^{ex}$ or R_{rs}) implies a maximum error of roughly 0.5% in the measured TOA radiance L_t. Such a small error in the TOA radiance cannot be achieved by pre-launch sensor radiometric calibration alone. Thus ocean color sensors require post-launch "vicarious calibration." This term refers to the process of (1) performing atmospheric correction to recover sea-level R_{rs} spectra from the measured L_t; (2) propagating the corresponding sea-level L_w back to the TOA (including the atmospheric path radiance contributions) to obtain a TOA radiance L_t^{AC} for comparison with the sensor-measured TOA radiance L_t. The difference between the retrieved L_t^{AC} and the measured L_t then (3) gives a final set of sensor calibration correction factors to be applied to the measured TOA radiances so that they lead, after atmospheric correction, to the proper sea-level water-leaving radiances and associated reflectances.

The Q part of the Morel et al. correction has been validated against empirical data for Case 1 waters by Voss et al. (2007) and found to give good agreement with measured radiance distributions. As concluded there, "...the bidirectional corrections based on the lookup tables generated from the model, and presently applied to ocean color imagery, are sound and amply validated for Case 1 waters..." However, it should be remembered that the above BRDF correction is based on a particular atmospheric model and on particular bio-optical models for Case 1 water. For

different atmospheric conditions, the f/Q correction would be different, although the difference would probably be small. However, for different water IOPs, in particular for Case 2 waters with high mineral particle loads or high concentrations of CDOM, the differences in the water-column scattering and absorption properties could have a significant effect on the f/Q correction. That variability has not yet been studied, and the above correction remains the current state of the science and is implemented by the OBPG for operational ocean color image processing.

Atmospheric Transmittances

Equations such as (1.3) and (3.13) involve various direct (T) and diffuse (t) atmospheric transmission terms, which require discussion.

4.1   Direct Transmittance

Direct atmospheric transmission is used if only one particular path, or a narrow bundle of nearly colinear paths, connects the source and the observer. This is the case for specular reflection, as illustrated in the left panel of Fig. 4.1. When the sea surface is viewed by the sensor, only a small patch of sea surface is seen as the Sun's specular reflection or direct glint. Other points of the sea surface would be seen as localized patches of Sun glint for other viewing directions, but not by the sensor viewing direction as shown. In each case, the reflected radiance is traveling in a very narrow set of directions determined by the Sun's location and the law of reflection ($\theta_r = \theta_s$ for a level surface). The narrow beams of Sun glint for other viewing directions are represented by the dotted and dash lines in the left panel of the figure. These beams can influence the direction of interest only via two scatterings: the first out of the reflected beam and the second into the direction of interest. Such a two-scatter path is shown by the light dashed line. Two scatterings makes the contributions of the unseen beams of specular reflection to the direction of interest very small.

Let τ be the atmospheric optical depth along a vertical path (the nadir viewing direction for the sensor). This τ includes all effects of atmospheric absorption and attenuation by all atmospheric constituents. For an off-nadir viewing direction θ_v, the direct transmittance is then simply

$$T(\theta_v) = \exp(-\tau/\cos\theta_v).\tag{4.1}$$

This geometry is analogous to the Lambert-Beer law for radiance propagation of a beam through a homogeneous medium: $L(r) = L(0)\exp(-cr)$, where c is the beam attenuation coefficient and r is the distance traveled. In the present case, $\tau = cr_a$, where r_a is the distance though the atmosphere on a vertical (nadir-viewing) path, and $r = r_a/\cos\theta_v$ is the atmospheric path length along the viewing direction.
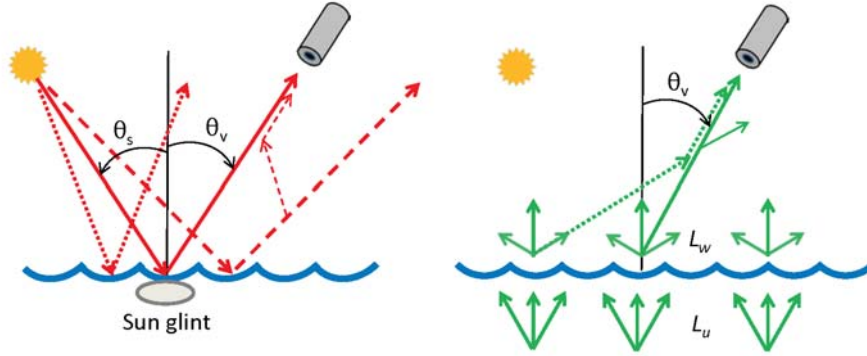
Figure 4.1: Left panel: Illustration of Sun glint as seen from the TOA, which is described by a direct transmittance. Right panel: Illustration of water-leaving radiance as seen from the TOA, which is described by a diffuse transmittance.

4.2 Diffuse Transmittance

For water-leaving radiance $L_{\rm w}$, every point of the sea surface is emitting an upward distribution of radiance $L_{\rm w}(\theta, \phi)$, as illustrated in the right panel of Fig. 4.1. Radiance from all locations and various directions can be scattered into the direction of interest via only one scattering, as illustrated by the dotted line in the right panel of Fig. 4.1. Radiance scattered out of the beam along the viewing direction can thus be replaced via a single scattering from the radiance emitted by a neighboring point propagating in a different direction. The diffuse transmittance therefore depends not just on the atmospheric properties and viewing direction, but also on the angular distribution of $L_{\rm w}$, which in general is unknown. This situation is analogous to the diffuse attenuation $K_{\rm d}$ of downwelling irradiance within the water column of a plane parallel ocean that is illuminated at all points of the surface. Because radiance absorbed or scattered out of the path between the source and sensor can be replaced by radiance from other sea surface points and directions, the diffuse transmittance $t(\theta_{\rm v})$ will be greater than the direct transmittance $T(\theta_{\rm v})$ (just as the the diffuse transmittance $\exp(-K_{\rm d}z)$ is always greater than than the beam transmittance $\exp(-cz)$). Accounting for the angular distribution of $L_{\rm w}$ and for the scattering processes makes the computation of diffuse transmittance more complicated than for direct transmittance.

The diffuse transmittance of the water-leaving radiance along a particular viewing direction $(\theta_{\rm v}, \phi_{\rm v})$ is by definition

$$t(\theta_{\rm v}, \phi_{\rm v}, \lambda) \equiv \frac{L_{\rm w}^{\rm TOA}(\theta_{\rm v}, \phi_{\rm v}, \lambda)}{L_{\rm w}(\theta_{\rm v}, \phi_{\rm v}, \lambda)} \,, \tag{4.2}$$

where $L_{\rm w}$ is the water-leaving radiance at the sea surface and $L_{\rm w}^{\rm TOA}$ is the water-leaving radiance that reaches the TOA. Henceforth, all quantities are assumed to be functions of wavelength, and the argument λ will be omitted. One way to compute $t(\theta_{\rm v}, \phi_{\rm v})$ is to run a coupled ocean-atmosphere radiative transfer model to compute the needed $L_{\rm w}(\theta_{\rm v}, \phi_{\rm v})$ and $L_{\rm w}^{\rm TOA}(\theta_{\rm v}, \phi_{\rm v})$ for a wide range of atmospheric and oceanic conditions, Sun and viewing geometries, and wavelengths. The values of $t(\theta_{\rm v}, \phi_{\rm v})$ would then be obtained via Eq. (4.2) and tabulated for later use. Such tables would need to be constructed for all possible aerosol types (i.e, aerosol phase function shapes), aerosol optical

thicknesses, water IOPs (or at least for chlorophyll concentrations in Case 1 waters), and viewing geometries. The tables would necessarily be large because of the large number of parameters that can affect $t(\theta_v, \phi_v)$.

Yang and Gordon (1997) examined the computation of diffuse transmittance and errors therein on the retrieved water-leaving radiance. Using a combination of radiative transfer numerical modeling of the ocean and atmosphere and reciprocity principles, they compared diffuse transmittances computed using realistic modeled and measured $L_u(\theta', \phi')$ distributions versus diffuse transmittances computed on the assumption that L_u is isotropic. Here $L_u(\theta', \phi')$ denotes the upwelling underwater radiance distribution just beneath the sea surface. For a level sea surface, $L_w(\theta_v, \phi_v) = T_F(\theta')L_u(\theta', \phi')/n_w^2$, where n_w is the index of refraction of the water, the in-water θ' is related to the in-air θ_v by Snel's law $\sin\theta_v = n_w \sin\theta'$, and $T_F(\theta')$ is the Fresnel transmittance of the surface from water to air. When L_u is isotropic, the diffuse transmittance is independent of the azimuthal angle and is denoted by $t^*(\theta_v)$.

Yang and Gordon (1997, Eq. 3) show via a clever use of reciprocity that the diffuse transmittance of radiance t^* along an atmospheric path in the direction of the Sun at solar zenith angle θ_o is numerically equal to the diffuse transmittance of irradiance from the TOA to a depth just beneath the sea surface, on the assumption that there is no upwelling radiance within the water. That is,

$$t^*(\theta_o) = \frac{E_R(\theta_o)}{F_o \cos(\theta_o) T_F(\theta_o)} , \tag{4.3}$$

where $E_R(\theta_o)$ is the downwelling plane irradiance just beneath the sea surface for an extraterrestrial solar irradiance F_o incident onto the TOA at angle θ_o, and $T_F(\theta_o)$ is the Fresnel downward transmission of the sea surface for radiance incident at angle θ_o from the normal. Since the upwelling radiance $L_u(\theta', \phi')$ used to obtain this result is assumed to be isotropic, the azimuthal dependence of t^* is irrelevant, and the desired diffuse attenuation for radiance at viewing direction $\theta_v = \theta_o$ is equal to the value of the irradiance transmission at the same polar angle. The great virtue of Eq. (4.3) is that it allows the efficient numerical computation of t^* using backward (reverse) Monte Carlo simulation of downwelling irradiance for a given aerosol type and optical thickness.

The retrieved water-leaving radiance is, by Eq. (4.2),

$$L_w(\theta_v, \phi_v) = \frac{L_w^{TOA}(\theta_v, \phi_v)}{t(\theta_v, \phi_v)} . \tag{4.4}$$

Let L_w^* denote the retrieval when t^* rather than t is used in Eq. (4.4). The error in the retrieved water-leaving radiance due to using t^* rather than the exact t is

$$\frac{\Delta L_w}{L_w} = \frac{L_w^* - L_w}{L_w} = \frac{t - t^*}{t^*} . \tag{4.5}$$

Yang and Gordon (1997) found that for viewing angles ϕ_v perpendicular to the principle plane (the plane of the Sun), the errors in the retrieved L_w are no more than 4% for viewing angles $\theta_v \leq 45$ deg, Sun zenith angles $\theta_o \leq 60$ deg, and aerosol optical thicknesses typical of clear atmospheres. The errors in band-ratio algorithms were less; e.g., the error in $L_w(443)/L_w(555)$ (used to retrieve chlorophyll concentration) is less than 2% except for very clear water and some viewing directions, for which the error in the ratio is about 3%. These parameter ranges covered most of the needs for SeaWiFS and errors of this magnitude were deemed acceptable compared to other errors in the

27

retrieval process (i.e., removal of atmospheric path radiance). In that case, the diffuse attenuation can be obtained by pre-computed functions of the form

$$t^*(\theta_v) = A(\theta_v) \exp[-B(\theta_v)\tau_a].$$

(4.6)

where $A(\theta_v)$ and $B(\theta_v)$ are tabulated for each aerosol type. Thus, for N angles θ_v, only $2N$ numbers $A(\theta_v)$ and $B(\theta_v)$ need to be tabulated for each aerosol type. Moreover, the aerosol type and optical thickness are determined as part of the process to remove the aerosol contribution to the total path radiance. This enables selection of the appropriate A, B, and τ_a, and evaluation of Eq. (4.4) is operationally feasible. If aerosols are ignored, Eq. (4.6) reduces to $t^*(\theta_v) = \exp[-\frac{1}{2}\tau_R/\cos\theta_v)]$, where τ_R is the Rayleigh optical thickness. This is the formula used in the early days for CZCS atmospheric correction. The value of Eq. (4.6) is that it allows the aerosol optical thickness τ_a to be incorporated into the diffuse transmittance calculations via a simple exponential and pre-computed A and B values.

However, for larger off-nadir viewing angles θ_v, for azimuthal viewing directions near $\phi_v = 0$ or 180 deg, and for very clear water, the errors $\Delta L_w/L_w$ can be as much as 6%. This could be significant for the MODIS Aqua sensor, which views a wide range of ϕ_v directions. Gordon and Franz (2008) therefore re-examined the model of Yang and Gordon (1997) and developed a correction term to t^* so that Eq. (4.4) becomes

$$L_w(\theta_v, \phi_v) = \frac{L_w^{TOA}(\theta_v, \phi_v)}{t^*(\theta_v)[1 + \delta(\theta_v, \phi_v)]}.$$

(4.7)

The $\delta(\theta_v, \phi_v)$ factor corrects for the bi-directional effects resulting from the use of an isotropic L_u in the computation of t^*, rather than the exact, non-isotropic $L_u(\theta', \phi')$. The $L_u(\theta', \phi')$ needed for computation of δ was obtained from $L_u = (f/Q)(b_b/a)$ and chlorophyll-based models for f/Q and b_b/a. Again, the δ correction term can be pre-computed and tabulated for various aerosol types and water IOPs. Evaluation of the impact of the δ correction applied to both SeaWiFS and MODIS Aqua data showed that retrieved water-leaving radiances will be in error by no more than $\sim$1% if $\theta_v < 60\,$deg and the δ correction is omitted. For $\theta_v > 60\,$deg, i.e. near the edges of scan lines, the use of the δ correction is warranted.

In current operational practice, the tabulated A and B functions are applied for both downwelling (solar irradiance) and upwelling L_w paths. The $\delta(\theta_v)$ correction of Gordon and Franz (2008) is not applied because it is an added complication with no significant impact in most instances.

CHAPTER 5

Vicarious Calibration

The atmospheric correction techniques described in Part II of this tutorial remove most of the effects of atmospheric scattering and absorption and sea surface reflectance from a measured TOA radiance. The end result is an estimate of the water-leaving radiance, which can be converted to a normalized reflectance as shown in §3.1. However, neither the sensor radiometric calibration nor the atmospheric correction are perfect, so a satellite-derived water-leaving radiance usually will not exactly match a water-leaving radiance measured at the sea surface. It is therefore necessary to make comparisons between satellite-derived radiances and radiances measured at the sea surface in order to determine the gain or correction factor needed to convert a best estimate of a radiance into one that agrees with the radiance measured at the sea surface. This process is called vicarious calibration.

The vicarious calibration methodology employed by the OBPG is described in Franz et al. (2007). Their procedure simultaneously corrects for residual errors in both sensor radiometric calibration and in atmospheric correction. The gain factors are therefore specific to a particular sensor and atmospheric correction procedure, but they are independent of the how the water-leaving radiance is obtained. It is assumed that the sensor has been calibrated as well as possible, so that only residual calibration errors need be corrected by the vicarious calibration process.

Operational data processing starts with a measured TOA total radiance L_t and derives the corresponding water-leaving radiance L_w. The process is based on Eq. (1.4):

$$L_t = \left(L_r + L_A + t_{dv}L_{wc} + t_{dv}L_w\right) t_{gv}t_{gs}f_p\,,\tag{5.1}$$

where (recall Table 1.1 and the associated discussion)

- L_t is the TOA radiance measured by the sensor,

- L_r is the Rayleigh radiance, which is due to scattering by atmospheric molecules,

- L_A is the radiance due to scattering by aerosol particles and aerosol-molecule multiple scattering,

- L_{wc} is the radiance due to whitecaps and foam,

- L_w is the water-leaving radiance,

- t_{dv} is the diffuse transmittance along the viewing path of the sensor,

- t_{gv} and t_{gs} are the transmittances by atmospheric gases in the viewing and solar directions respectively, and

- f_p is a known sensor-specific polarization-correction factor.

These quantities are all functions of wavelength. No specular-reflection term is included in Eq. (5.1) because it is assumed that pixels containing a detectable amount of specular reflection are omitted from consideration. In this equation, the aerosol radiance L_A and the water-leaving radiance L_w are the two primary unknowns. The aerosol-dependent diffuse transmittance t_{dv} can be computed for a given aerosol type as described in §4.2. The Rayleigh and whitecap radiances and the gaseous transmittances can be computed for given atmospheric conditions as described in Part II of this report. The determination of the aerosol contribution is the crux of the atmospheric correction process and will be described in §9. These computations constitute the atmospheric correction process. Once these terms have been computed, Eq. (5.1) can be solved for a measured L_t to obtain the corresponding L_w.

To develop the correction factors, this process is reversed. Let L_w^t denote the known or "target" water-leaving radiance that is to be matched by the satellite-derived value. In most instances, the target water-leaving radiance is obtained from in-situ measurement, but can in principle be the value retrieved by another satellite sensor or predicted by a model. In any case, this value can be propagated to the TOA under various assumptions about the atmospheric conditions to obtain the corresponding target TOA radiance L_t^t which, ideally, would match the satellite-measured TOA radiance. The ratio

$$g(\lambda) = \frac{L_t^t(\lambda)}{L_t(\lambda)} \qquad (5.2)$$

is then the correction or gain factor that, when multiplied by a measured L_t gives an adjusted TOA radiance L_t^t that, when atmospherically corrected, yields the correct water-leaving radiance L_w^t. Note that the gain factor is different for each wavelength. The gain factors are created via a series of "match-up" comparisons of satellite and in situ data and then, once determined, are routinely applied as part of the operational reduction of satellite-measured TOA radiances to water-leaving radiances.

Now consider the details of the computation of the gain factors. A satellite-derived L_w is converted to an exact normalized water-leaving radiance as described in §3.1. This process can be summarized as

$$[L_w]_N^{ex} = \frac{L_w}{\mu_s \, f_s \, t_{ds} \, f_b \, f_\lambda} , \qquad (5.3)$$

where

- μ_s is the cosine of the solar zenith angle (cf. Eq. 3.2),

- f_s is the Earth-Sun distance correction factor (cf. Eq. 3.2),

- t_{ds} is the Rayleigh-aerosol diffuse transmittance in the Sun's direction (cf. Eq. 3.2),

- f_b is the BRDF correction factor (cf. Eq. 3.7), and

- f_λ is a band-pass adjustment factor.

A target water-leaving radiance is converted to an exact normalized water-leaving radiance in the same manner:

$$[L_w^t]_N^{ex} = \frac{L_w^t}{\mu_s^t \, f_s^t \, t_{ds}^t \, t_{gs}^t \, f_b^t \, f_\lambda^t} \, , \tag{5.4}$$

where now the superscript t on the terms in Eq. (5.4) indicates that these terms are evaluated for the Sun and viewing geometry at the time of the measurement of L_w^t, which may be different from the geometry at the time of the satellite observation leading to L_w. A factor of t_{gs} is included in Eq. (5.4) to account for the diffuse transmittance due to absorption by gases in the Sun's direction at the time of measurement of L_w^t. This factor does not appear in Eq. (5.3) because that correction to the total measured radiance L_t^t is accounted for in Eq. (5.1). The radiances in Eq. (5.1) are computed for the full spectral response of each sensor band. The f_λ factor converts these full-band values to nominal band-center wavelengths to remove residual out-of-band response effects. Since the satellite and in situ instruments usually have different spectral responses, this factor adjusts the satellite and in situ values to a common wavelength dependence.

Writing L_w in terms of $[L_w]_N^{ex}$ via Eq. (5.3) and then replacing $[L_w]_N^{ex}$ by the target value $[L_w^t]_N^{ex}$ gives an equation for the target value of the TOA radiance:

$$L_t^t = \left(t_{dv}[L_w^t]_N^{ex}(\mu_s \, f_s \, t_{ds} \, f_b \, f_\lambda) + L_r + L_A^t + t_{dv}L_{wc} \right) t_{gv}t_{gs}f_p \, . \tag{5.5}$$

The total transmittance along the Sun's path is the product of the diffuse transmittance for the Rayleigh and aerosol scattering and the diffuse transmittance for gaseous absorption. The t_{ds}^t term depends on the aerosols and is thus an unknown for the calibration target. The total transmittance for the target could be obtained from axillary measurements (e.g., from a Sun photometer) made at the time of the target radiance measurement. However, such measurements are not generally available and, even if available, any error in those measurements would be an additional source of error in the the target radiance. Therefore, the satellite-retrieved atmospheric and aerosol properties are used to evaluate the total transmittance for the target measurement via

$$t_{ds}^t t_{gs}^t = \exp \left[\ln(t_{ds}t_{gs}) \frac{\mu_s}{\mu_s^t} \right] \, . \tag{5.6}$$

The total transmittance for the target is therefore the total transmittance for the satellite with a correction for the difference in the solar zenith angles. Other terms in Eq. (5.5) such as the Rayleigh radiance and gaseous transmittances along the viewing direction are evaluated for the atmospheric conditions of the satellite retrieval as described in §6. Thus the t_{dv} that multiplies L_{wc} is determined by Rayleigh-scattering calculations based on the sea-level pressure. The whitecap radiance is modeled as a function of wavelength and wind speed as described in §8. These choices reference both the target and the satellite radiances to a common atmosphere, which is desirable for the development of the gain factors.

Finally, the BRDF correction factors f_b and f_b^t must be evaluated. As discussed in §3.2, the IOPs needed for evaluation of the BRDF correction are parameterized in terms of the chlorophyll concentration Chl. If a measurement of Chl is made in conjunction with the target measurement, then that value of Chl can be used to evaluate the BRDF correction. However, chlorophyll measurements are not usually available. Operationally, the chlorophyll concentration is obtained via

31

insertion of the satellite-derived $[L_w]_N^{ex}$ (or the corresponding reflectance $[\rho_w]_N^{ex}$) into a chlorophyll-retrieval algorithm. That is an iterative process because $[L_w]_N^{ex}$ is required to determine Chl, and Chl is required to determine $[L_w]_N^{ex}$. During the determination of gain factors, the target radiance can be used as input to the operational chlorophyll-retrieval algorithm and no iteration is required.

The final issue is the determination of the aerosol properties. This is a two-step process based on the "black-pixel" assumption to be described in §9.2. As seen in Table 9.1, satellite sensors have two NIR wavelengths used for aerosol retrievals. Call the longer of these wavelengths λ_L and the shorter λ_S. (For VIIRS, the NIR bands are at the nominal wavelengths $\lambda_L = 862$ nmm and $\lambda_S = 745$ nmm.) During determination of the gain factors, it is first assumed that the water-leaving radiance at these two wavelengths is zero (the black-pixel assumption). This is usually a good approximation for the mid-ocean, oligotrophic waters used for vicarious calibration. It is further assumed that the instrument calibration is perfect for the λ_L band, in which case the gain factor for the longer NIR band is $g(\lambda_L) = 1$. The black-pixel assumption means that Eqs. (5.1) and (5.5) reduce to

$$L_t(NIR) = \left(L_r + L_A + t_{dv}L_{wc} \right) t_{gv}t_{gs}f_p \tag{5.7}$$

$$L_t^t(NIR) = \left(L_r + L_A^t + t_{dv}L_{wc} \right) t_{gv}t_{gs}f_p , \tag{5.8}$$

respectively, at the two NIR bands. Given the satellite-measured TOA radiances at the two NIR bands, Eq. (5.7) can be solved for L_A at the two NIR bands. The assumption that $g(\lambda_L) = 1$ means that $L_A^t(\lambda_L) = L_A(\lambda_L)$. Thus $L_t^t(\lambda_L)$ is determined via Eq. (5.8) evaluated at λ_L. The locations for match-ups are purposely chosen at times and locations where it is reasonable to assume that the aerosol type in stable and predictable over the image area, e.g. mid-ocean areas where the aerosols are predominately sea salt and water droplets. The aerosol model derived from the satellite measurements as described in §9.2 can then be used along with the value of $L_t^t(\lambda_L)$ to determine $L_t^t(\lambda_S)$. Both L_t and L_t^t are then known at the two NIR wavelengths, and the NIR gain factor at $g(\lambda_S)$ can be determined by Eq. (5.2).

Values of $g(\lambda_S)$ are computed for various times and locations during the lifetime of the mission. These values are averaged to determine the mean gain $\bar{g}(\lambda_S)$. The selection of suitable images for gain determination is quite strenuous and most candidate pixels are eliminated from consideration because of glint, inhomogeneous water at the target location, or non-ideal atmospheric conditions. The details of the selection criteria and statistical determination of the mean gain factors are given in Franz et al. (2007). Experience shows that 20 to 40 match-ups are required for the determination of $\bar{g}(\lambda_S)$ values that are stable to within 0.1% of their long-term values. Once the NIR gains $g(\lambda_L) = 1$ and $\bar{g}(\lambda_S)$ have been determined for the given sensor, the extrapolation algorithm described in §9.2 can be used to determine $L_A^t(\lambda)$ at all wavelengths. Equation (5.8) then gives $L_t^t(\lambda)$, and the gains at the remaining visible wavelengths are obtained from Eq. (5.2). Once determined, the gains are held fixed and applied as part of the operational atmospheric correction process.

For the SeaWiFS sensor the gains ranged from 1.0377 at 412 nm to 0.972 at 765 nm. A correction of 3 or 4% to the TOA radiance can correspond to a 30 or 40% correction to the water-leaving radiance because the water-leaving radiance is typically about 10% of the TOA radiance. Thus the determination of accurate gain factors is critical to the overall retrieval process. It must be remembered that a set of gains must be determined for each sensor and atmospheric correction algorithm. As improvements are made to the atmospheric correction algorithms described in Part

II, the gains must be recomputed. However, these recomputations can be made using the original target radiances. Gain recalculation is a part of the standard reprocessing of data sets.

Part II

The NASA OBPG Algorithms

This part of the tutorial discusses, one by one, the various corrections made to the TOA radiance during the OBPG atmospheric correction process. The entire sequence of data processing beginning with the measurement of a TOA radiance and ending with the output of a geophysical product such as a global map of chlorophyll concentration is divided into a number of processing levels. These steps are defined in Table 5.1. The atmospheric correction process described here takes the data from Level 1b to Level 2.

Table 5.1: Processing Levels

Level	Definition
0	refers to unprocessed instrument data at full resolution. Data are in "engineering units" such as volts or digital counts.
1a	is unprocessed instrument data at full resolution, but with information such as radiometric and geometric calibration coefficients and georeferencing parameters appended, but not yet applied, to the Level 0 data.
1b	refers to Level 1a data that have been processed to sensor units (e.g., radiance units). Level 0 data are generally not recoverable from level 1b data.
	Atmospheric correction is applied to Level 1b TOA radiance to create Level 2 data.
2	refers to derived geolocated, geophysical variables (e.g., normalized water-leaving reflectance $[\rho_\mathrm{w}(\lambda)]_\mathrm{N}^\mathrm{ex}$, chlorophyll concentration, $K_\mathrm{d}(490 \text{ nm})$, and AOT(865 nm)) at the same resolution and location as Level 1 data.
3	are variables mapped onto uniform space-time grids, often with missing points interpolated or masked, and with regions mosaiced together from multiple orbits to create large-scale maps, e.g. of the entire earth.
4	refers to results obtained from a combination of satellite data and model output (e.g., the output from an ocean ecosystem model), or results from analyses of lower level data (i.e., variables that are not measured by the instruments but instead are derived from those measurements).

The next chapter shows how to account for absorption and scattering by atmospheric gases. Sea-surface reflectance by Sun glint and white caps are then discussed, followed by the various aspects of correction for the effects of atmospheric aerosols. The last two chapters discuss the sensor-specific corrections for spectral out-of-band response and for polarization. Figure 5.1 shows the sequence in which the various corrections are applied during the overall process.

It is important to keep in mind that there are severe computational constraints on how atmospheric correction is performed on an operational basis. The MODIS-Aqua sensor, for example, collects about 1.4 terrabytes of data per day. The requirement to routinely process this amount of data (along with data from other sensors) requires that various approximations be made in order to speed up the calculations. Some of the corrections require ancillary information such as sea level pressure, wind speed, and ozone concentration, which are not collected by ocean color sensors
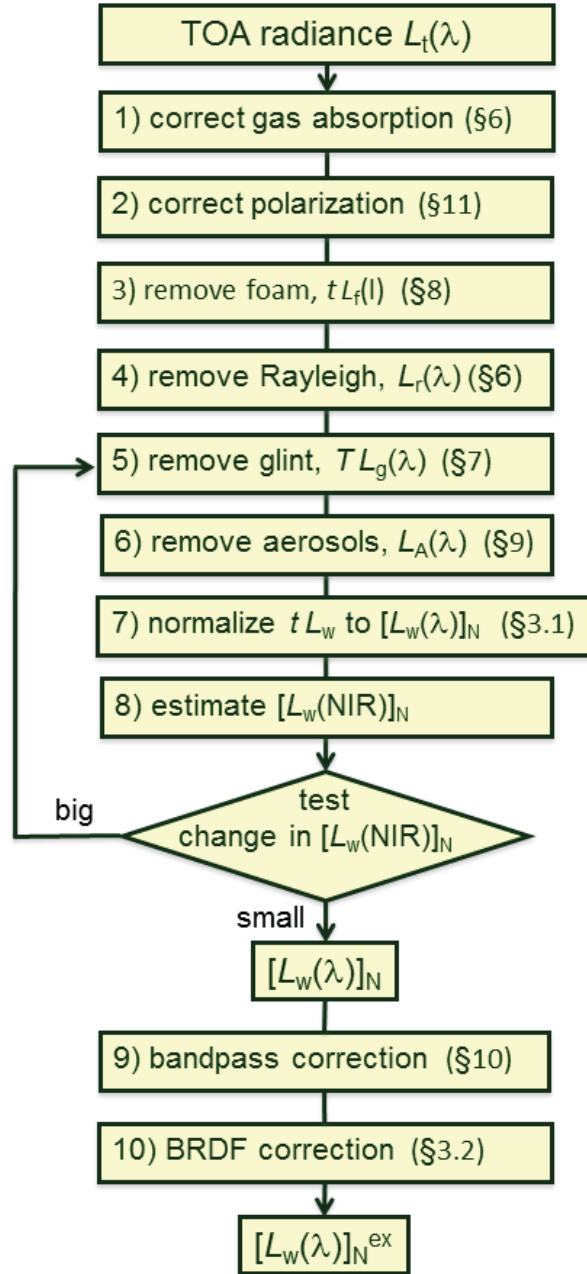
Figure 5.1: Flowchart of the atmospheric correction process. The section numbers refer to the pages giving the details of each step.

themselves. These ancillary data may be inaccurate or missing (in which case climatological values must be used). The quality of the ancillary information impacts the accuracy of the atmospheric correction. Table 5.2 shows some of the ancillary data and its sources as used by the various atmospheric correction algorithms.

Table 5.2: Ancillary data needed for atmospheric correction. Abbreviations: NCEP, National Centers for Environmental Prediction; OMI, Ozone Monitoring Instrument; TOMS, Total Ozone Mapping Spectrometer; SCIAMACHY, SCanning Imaging Absorption spectroMeter for Atmospheric CHartographY; GOME, Global Ozone Monitoring Experiment; Reynolds/NCDC, Reynolds analysis, National Climate Data Center; NCEI, NOAA National Centers for Environmental Information (previously NODC); NSIDC, National Snow and Ice Data. Center.

Data	Source	Use
atmospheric pressure	NCEP	Rayleigh correction
water vapor	NCEP	transmittance
wind speed	NCEP	Rayleigh, Sun glint, white caps
ozone concentration	OMI/TOMS	transmittance
NO_2 concentration	SCIAMACHY/OMI/GOME	transmittance
sea surface temperature	Reynolds/NCDC	seawater index of refraction and backscattering
sea surface salinity	NCEI World Ocean Atlas, Salinity Climatology	seawater index of refraction and backscattering
sea ice coverage	NSIDC	masking

The sea surface temperature and salinity are used to compute the water index of refraction and water backscattering coefficient as described in Werdell et al. (2013). Operationally, pixels are masked before atmospheric correction for only a few conditions, namely the presence of land or clouds, and saturation of the measured radiance. An attempt is made to process all other pixels. A separate mask is applied during atmospheric correction to pixels with too much Sun glint. Various flags are incorporated into Level 2 and 3 data after the atmospheric correction process described below. These identify pixels that may have various problems such as sea ice contamination, turbid water, bottom effects, or failed atmospheric correction. These flags are listed at `http://oceancolor.gsfc.nasa.gov/VALIDATION/flags.html`. Other information on flags is given in Patt et al. (2003, Chapter 6). With the exception of Sun glint, applying masks and flags is not a part of the atmospheric correction process per se, so this topic is not discussed here.

Gases

This chapter first describes the Rayleigh corrections made for non-absorbing gases, and then the corrections for absorbing gases.

6.1 Nonabsorbing Gases

A radiative transfer numerical model is used to solve the vector (polarized) radiative transfer equation for non-absorbing atmospheric gases only. The radiative transfer model includes atmospheric multiple scattering, polarization, and sea surface roughness modeled analytically by a Cox-Munk slope distribution with an added analytical wave shadowing function. The Cox-Munk slope distribution is azimuthally isotropic (no dependence on wind direction); therefore only the relative angle between Sun and viewing direction matters. This greatly simplifies the Fourier decomposition described in Wang (2002, Eq. 3). The radiative transfer model is described in Ahmad and Fraser (1982).

6.1.1 Wind Speed and Surface Reflectance Effects

Background sky reflectance by the rough sea surface is accounted for as part of the Rayleigh correction. Some sensors (CZCS, SeaWiFS, OCTS) could be tilted to avoid looking at glint near the Sun's specular direction. Other sensors (MODIS, VIIRS, MERIS, OLI) do not tilt and therefore must account for specular reflection.

Wind speed and surface glint corrections are computed as described in Wang (2002): Run the numerical model to compute a look up table (LUT) of TOA Fourier components $L_r^m(\lambda, \theta_s, \theta_v, \tau_{Ro}, W)$ (his Eq. 3) for the following conditions:

- The sensor wavelength bands (e.g., bands centered at 412, 443, 490, 510, 555, 670, 765, 865 for SeaWiFS). The radiative transfer model is run using band-averaged optical thicknesses (rather than running at high-wavelength resolution, and then averaging the L_r values over the band response functions to get the nominal band values of L_r for a particular sensor).

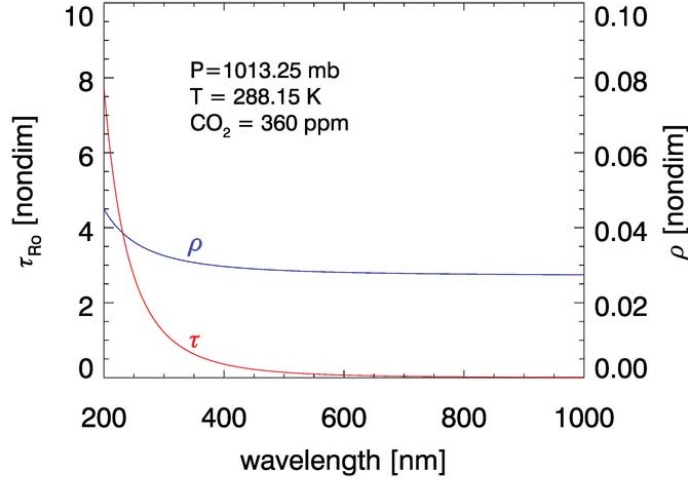- 45 Sun zenith angles θ_s from 0 to 88 deg by 2 deg

Figure 6.1: The Rayleigh optical thickness and depolarization ratio based on Bodhaine et al. (1999). [Plotted from NASA data file rayleigh_bodhaine.txt]

- 41 viewing nadir angles θ_v from 0 to 84 deg by roughly 2 deg

- Rayleigh optical thickness τ_{Ro} for standard sea level atmospheric pressure $P_o = 1013.25$ hPa (1013.25 millibar).

- 8 wind speeds $W = 0$, 1.9, 4.2, 7.5, 11.7, 16.9, 22.9 and 30.0 m/s. (These wind speeds correspond to convenient spacing in the mean square slopes of the sea surface according to the Cox-Munk equation $mss = 0.00512W$: $mss = 0.0$, 0.01, 0.02, 0.04, 0.06,... for $W = 0$, 1.9, 4.2, 7.5, 11.7, ...) Linear interpolation is used for values between these wind speeds.

The Rayleigh optical thickness $\tau_{Ro}(\lambda)$ at 1 atmosphere of pressure, P_o (1013.25 hPa), temperature of 288.15K, and a CO_2 concentration of 360 ppm is given by Bodhaine et al. (1999, Eq. 30):

$$\tau_{Ro}(\lambda) = 0.0021520 \left(\frac{1.0455996 - 341.29061\lambda^{-2} - 0.90230850\lambda^2}{1.0 + 0.0027059889\lambda^{-2} - 85.968563\lambda^2} \right) , \qquad (6.1)$$

where λ is in micrometers. These values and the corresponding Rayleigh depolarization ratio $\rho(\lambda)$ are shown in Fig. 6.1. (At the scale of this figure, the Bodhaine values are almost indistinguishable from the values given by the formula of Hansen and Travis (1974); see Bodhaine et al. (1999, Eq. 15), which were used in earlier calculations.)

The Rayleigh LUTs for L_r contain the I, Q and U Stokes vector components in reflectance units, as a function of wind speed and geometry. The Stokes vector V component for circular polarization is assumed to be zero. There is a separate LUT for each wavelength.

During image correction, the wind speed W for a given pixel comes from NCEP 1 deg gridded data, interpolated to the image pixel.

6.1.2 Pressure Effects

The Rayleigh optical thickness at the time of the observation depends on the number of atmospheric gas molecules between the sea surface and the top of the atmosphere. The number of molecules is directly proportional to the sea-level pressure P. Thus the Rayleigh optical thickness at any pressure P is given by

$$\tau_R(P, \lambda) = \frac{P}{P_o} \tau_{Ro}(P_o, \lambda) \,.$$

The TOA L_R is then computed by (Wang (2005, Eq. 5) and subsequent equations)

$$L_R[\tau_R(P, \lambda)] = L_R[\tau_R(P_o, \lambda)] \frac{1 - \exp[-C(\lambda, M)\tau_R(P, \lambda)M]}{1 - \exp[-C(\lambda, M)\tau_R(P_o, \lambda)M]} \,, \tag{6.2}$$

where

$$M = \frac{1}{\cos\theta_s} + \frac{1}{\cos\theta_v} \tag{6.3}$$

is the geometric air mass factor for the total path through the atmosphere. $C(\lambda, M)$ is a coefficient that is determined so that Eq. (6.2) gives the best fit to $L_R[\tau_R(P, \lambda)]$ as computed by an extremely accurate atmospheric radiative transfer model when run for values of sea level pressure $P \neq P_o$. Numerical simulations show that this coefficient can be modeled as

$$C(\lambda, M) = a(\lambda) + b(\lambda)\ln(M)$$
$$a(\lambda) = -0.6543 + 1.608\tau_R(P_o, \lambda)$$
$$b(\lambda) = 0.8192 - 1.2541\tau_R(P_o, \lambda) \,.$$

6.2 Absorbing Gases

CO, N_2O, CH_4, and CO_2 have negligible absorption at the visible and NIR wavelengths relevant to ocean color remote sensing. However, O_2, O_3, NO_2, and H_2O have absorption bands in the visible and NIR. The O_2 and H_2O bands can be avoided by judicious choice of sensor bands, as shown in Fig. 6.2 for the MODIS bands. However, as seen in Figs. 6.3 and 6.4, O_3 and NO_2 have broad, concentration-dependent absorption bands that cannot be avoided. It is therefore necessary to account for absorption by these two gases.

The concentrations of absorbing gases are usually measured as column concentrations, i.e., the number of molecules per unit area, or as the equivalent in Dobson units. One Dobson unit refers to a layer of gas that would be 10 μm thick at standard temperature and pressure, or about 2.69×10^{16} molecules cm^{-2}. 1000 DU = 1 atm-cm; that is, 1000 DU is the number of molecules that would give a layer of gas 1 cm thick at a pressure of one atmosphere.

For optically thin absorbing gases that are high in the atmosphere (O_3 in particular), it is possible to correct for absorption using just the geometric air mass factor M computed as in Eq. (6.3) because scattering is not significant. However, for gases near the surface (NO_2 in particular), multiple scattering by dense gases and aerosols is significant and increases the optical path length, hence the absorption. Thus M is not a good approximation for the total optical path length through an absorbing gas near sea level.

Note that an absorbing gas reduces the TOA radiance because light is lost to absorption. Correcting for this loss will increase the TOA radiance or reflectance, with the effect being greatest at blue wavelengths where multiple scattering is greatest.
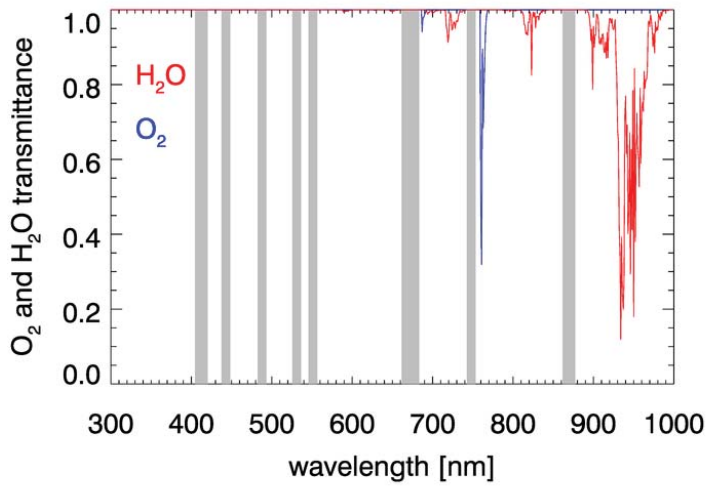
Figure 6.2: Transmittance by O_2 and H_2O for a moist tropical atmosphere. The resolution is 1 nm. The MODIS sensor bands are shaded in gray.

Figure 6.3: Transmittance by O_3 for 200, 350, and 500 Dobson units and a vertical path through the atmosphere.

Figure 6.4: Transmittance by NO_2 for low (2.8×10^{15}), typical (1.1×10^{16}), and high $(6.0 \times 10^{16}$ molecules cm$^{-2})$ concentrations of NO_2 and a vertical path through the atmosphere.

6.2.1 Absorption by Ozone

The diffuse transmission by ozone can be written as

$$t_{O_3} = \exp\left[-\tau_{O_3}\left(\frac{1}{\cos\theta_s} + \frac{1}{\cos\theta_v}\right)\right] \tag{6.4}$$

$$= \exp\left[-\tau_{O_3}M\right],$$

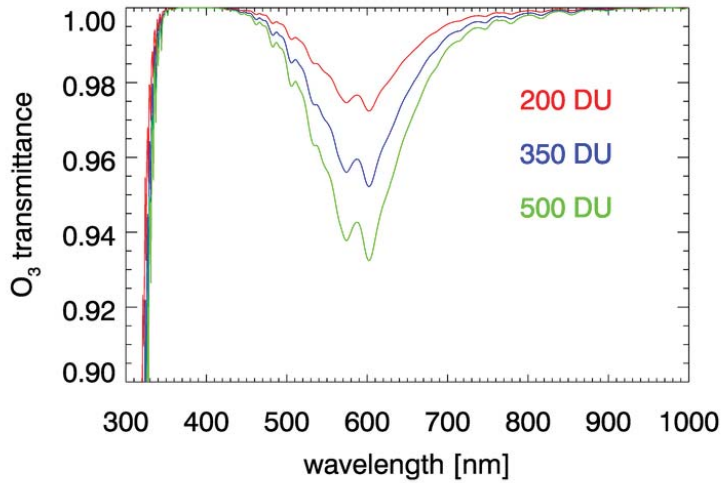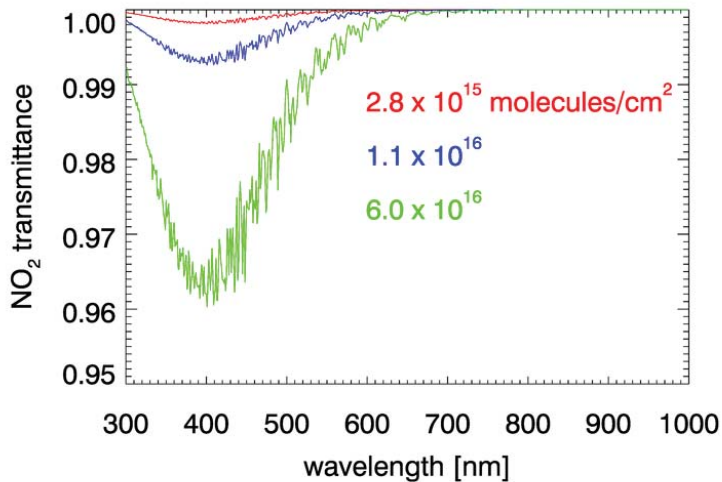where M is the geometric air mass factor previously defined in Eq. (6.3), and τ_{O_3} is the optical thickness of the ozone for a vertical path through the atmosphere. Scattering by ozone is negligible, but absorption is significant at some wavelengths. Thus τ_{O_3} is the optical thickness for absorption by ozone, which is given by

$$\tau_{O_3}(\lambda) = [O_3]k_{O_3}(\lambda), \tag{6.5}$$

where $[O_3]$ is the ozone concentration (column amount in molecules cm^{-2}), and k_{O_3} is the absorption cross section (in cm^2 molecule^{-1}). The ozone concentration $[O_3]$ for a given image pixel is obtained from the NASA OMI or TOMS sensors (Ozone Monitoring Instrument; Total Ozone Mapping Spectrometer, now replaced by OMI).

As was seen for transmittance in Figs. 6.3 and 6.4, the absorption cross sections for gases like O_3 and, especially, NO_2 can vary with wavelength on a nanometer scale. To fully resolve the effects of such wavelength dependence on sensor signals, radiative transfer calculations would require computationally intensive "line-by-line" calculations followed by integration over the sensor bands. To avoid that computational expense, band-averaged values of the Rayleigh optical depth and absorption cross sections k_{O_3} and k_{NO_2} are computed for each sensor and tabulated. Radiative transfer calculations then use the band-averaged values with just one radiative transfer calculation done for each sensor band. These band-averaged values depend on the sensor even for the same nominal wavelength band (e.g, the 412 nm blue band) because of different band widths about the nominal center wavelength and different sensor response functions within a band. Figure 6.5 shows example band-averaged values for the VIIRS and MODIS Aqua sensors.
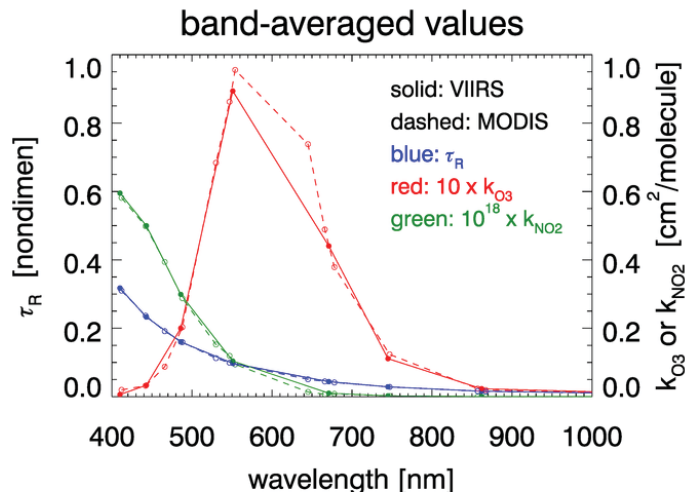
Figure 6.5: Band-averaged Rayleigh optical depth τ_R, ozone absorption cross section k_{O_3}, and NO_2 absorption cross section k_{NO_2} for the VIIRS and MODIS Aqua sensors. (Data from `http://oceancolor.gsfc.nasa.gov/DOCS/RSR_tables.html`)

6.2.2 Absorption by NO_2

Nitrogen dioxide NO_2 occurs both in the stratosphere and near the Earth's surface. NO_2 in the lower atmosphere is generated primarily by human activities (automobiles, industry, fires), and the highest concentrations are near the earth's surface in industrial areas. Numerical simulations show that failure to correct for absorption by NO_2 can give errors of approximately 1% in TOA radiances at blue wavelengths, which result in $\sim 10\%$ errors in retrieved water-leaving radiances (Ahmad et al., 2007).

The geometric air mass factor M of Eq. (6.3) and a simple atmospheric transmittance function like that of Eq. 6.4) are valid for ozone absorption corrections because scattering by ozone in the upper atmosphere is negligible. However, such functions may be not adequate for NO_2 correction calculations because of multiple scattering in the dense lower atmosphere. Further guidance for the form of the NO_2 correction comes from the observation that the water-leaving radiance L_w sees all NO_2 in the atmosphere, so the total NO_2 concentration N must be used to correct L_w for NO_2 absorption. However, the upwelling atmospheric path radiance L_{atm}, which is generated throughout the atmosphere, is not strongly influenced by the absorbing gas very near the surface. Extremely accurate numerical simulations show that in that case, N', the NO_2 concentration between an altitude of 200 m and the TOA, can be used as a satisfactory measure of NO_2 concentration. This result leads to different corrections for the measured TOA path radiance and for the water-leaving radiance.

Let ρ_{obs} be the uncorrected, observed (measured) TOA reflectance, and let ρ_{corr} be the TOA reflectance corrected for NO_2 absorption effects. Comparison of numerical simulations and analytical approximations justifies a correction of the form

$$\rho_{corr} = \rho_{obs} \exp\left[\alpha N'\left(\frac{1}{\cos\theta_s} + \frac{1}{\cos\theta_v}\right)\right],$$

43

where N' is the NO_2 concentration between an altitude of 200 m and the TOA. This simple formula gives ρ_{corr} values that are within 0.15% of the values obtained by exact numerical simulations that account for the total column NO_2 concentration and multiple scattering.

The correction for water-leaving radiance proceeds as follows. The reflectances can be written as (Ahmad et al., 2007, Eqs. 1 and 7)

$$\rho_t(\theta_s, \theta_v) = \rho_{\text{path}}(\theta_s, \theta_v) + t_3(\theta_v) t_d(\theta_s) \rho_w(\theta_s, \theta_v) + \text{glint and whitecap terms}$$

(omitting the arguments for wavelength, azimuthal angle, and wind speed). Here t_3 is the diffuse transmission along the viewing direction from the sea surface to the sensor, t_d is the diffuse transmission of downwelling solar irradiance, and ρ_w is the water-leaving reflectance at the sea surface. Consider now only the path and water-leaving terms, and omit the directional arguments for brevity. Then multiplying this equation by the exponential correction factor for the observed TOA reflectance gives

$$\rho_t \exp\left[\alpha N' \left(\sec\theta_s + \sec\theta_v\right)\right] = \rho_{\text{path}} \exp\left[\alpha N' \left(\sec\theta_s + \sec\theta_v\right)\right]$$
$$+ \left[t_3 \exp(\alpha N' \sec\theta)\right] \left[t_d \rho_w \exp(\alpha N' \sec\theta_s)\right].$$

Numerical simulations show that both the path reflectance and the diffuse transmission term $[t_3 \exp(\alpha N' \sec\theta)]$ are accurate to within 0.2% with this correction. However, the error in the water-leaving factor, $[t_d \rho_w \exp(\alpha N' \sec\theta_s)]$ is in error by 0.5 to 1.5%, which is unacceptably large. The reason for the greater error in this term is that it depends on the downwelling irradiance, which passes through the entire atmosphere and thus sees the total concentration N, not just the reduced concentration N' that is adequate for correction of the TOA path term. However, the error in this term also decreases to $\sim 0.2\%$ if N' is replaced by N. This error can be reduced still further by the following empirical procedure.

For bands where NO_2 absorption is significant (e.g., at 412 or 443 nm), the atmospheric correction is determined as always (without NO_2 correction) using the NIR bands. However, rather than subtract these terms from the corrected TOA reflectance, the atmospheric correction terms (including the Rayleigh reflectance) are reduced for NO_2 absorption by applying a factor of $\exp[-\alpha N'(\sec\theta_s + \sec\theta_v)]$. The computed path reflectance for NO_2 is then subtracted from the observed TOA reflectance to obtain $\Delta\rho_{\text{obs}} = t_3 t_d \rho_w$, which is the TOA value for water-leaving reflectance in the presence of NO_2. The NO_2-corrected value of the water-leaving reflectance is then obtained by multiplying this $\Delta\rho_{\text{obs}}$ by $\exp(\alpha N' \sec\theta) \exp(\alpha N \sec\theta_s)$, which gives

$$\exp(\alpha N' \sec\theta) \exp(\alpha N \sec\theta_s) \Delta\rho_{\text{obs}}$$
$$= \left[t_3 \exp(\alpha N' \sec\theta)\right] \left[t_d \rho_w \exp(\alpha N \sec\theta_s)\right].$$

Note that $t_3 \exp(\alpha N' \sec\theta)$ is the NO_2-corrected transmission term, and $\rho'_w = t_d \rho_w \exp(\alpha N \sec\theta_s)$ is the desired NO_2-corrected water-leaving reflectance. This equation is then solved to obtain ρ'_w:

$$\rho'_w = \frac{\exp(\alpha N' \sec\theta) \exp(\alpha N \sec\theta_s) \Delta\rho_{\text{obs}}}{t_3 \exp(\alpha N' \sec\theta)}. \tag{6.6}$$

Note that the exponentials are increasing the magnitude of the water-leaving radiance compared to the no-NO_2 case, which accounts for the loss due to NO_2 absorption along the paths of the Sun's

direct beam and the viewing direction. The term for the Sun's direct beam uses the full column NO_2 concentration N, whereas the viewing-path term uses the reduced concentration N'. This is an artifice that brings the analytical correction of Eq. (6.6) into close agreement with the exact numerical calculations. The absorption cross section α is a function of wavelength. Computations are done for α at 18 deg C, and then a temperature correction is made. (Ahmad's Table 1 gives the band-averaged NO_2 absorption cross sections for SeaWiFS and MODIS bands, which are called σ in that table. This σ is same quantity as α in his Eq. (4) and in the equations of this chapter.)

Sun Glint

Both direct Sun glint and background sky reflectance are included in the radiative transfer calculations. However, the Sun glint contribution is removed from the LUTs so as to allow the historical approach of Gordon and Wang (1994a) to be used. The current Rayleigh LUTs are wind speed dependent, but the aerosol LUTs assume a flat ocean. Thus the LUTs include diffuse sky reflectance but not specular reflection. There is thus an explicit correction for Sun glint, but not for diffuse sky reflectance, which is accounted for as part of the Rayleigh correction.

Even for sensors (such as SeaWiFS) that are designed with tilt capabilities allowing them to be oriented so that they do not look at the Sun's glitter pattern, there can still be significant residual glint radiance reaching the sensor, especially near the edges of the obvious glint area. This is corrected as follows.

Recall Eq. (1.3):

$$L_\mathrm{t} = L_\mathrm{R} + [L_\mathrm{a} + L_\mathrm{Ra}] + TL_\mathrm{g} + tL_\mathrm{wc} + tL_\mathrm{w} \,,$$

where L_g is the direct Sun glint radiance. L_g is computed using the analytical Cox-Munk wind speed-wave slope distribution and the Sun and viewing geometry. Wang and Bailey (2001, Eq. 2) write the Sun glint radiance L_g in terms of a normalized Sun glint L_GN, which is defined by

$$L_\mathrm{g}(\lambda) \equiv F_\mathrm{o}(\lambda)T(\theta_\mathrm{s}, \lambda)L_\mathrm{GN} \,.$$

L_GN is computed using an azimuthally symmetric analytical form of the Cox-Munk wind speed–wave slope distribution for the given Sun and viewing directions, and an incident irradiance of magnitude $F_\mathrm{o}(\lambda) = 1$ W m^{-2} nm^{-1}. L_GN thus has the angular distribution of the surface-reflected radiance, but its units are 1/steradian. Note that L_GN is independent of wavelength.

During image processing, pixels with a value of $L_\mathrm{GN} > 0.005$ sr^{-1} are masked out as having too much glint to be useful. Pixels with $L_\mathrm{GN} \leq 0.005$ sr^{-1} have a glint correction applied before use.

For the glint correction, atmospheric attenuation occurs first along the path of the Sun's direct solar beam as the Sun's beam travels from the TOA to the sea surface; the associated transmittance is $T(\theta_\mathrm{s}, \lambda)$. Attenuation then occurs along the viewing direction from the sea surface back to the TOA; this transmittance is $T(\theta_\mathrm{v}, \lambda)$. These are both direct beam transmittances because only one particular path connects the Sun with a point on the sea surface that reflects the direct beam into the sensor (recall the left panel of Fig. 4.1). The total "two-path" transmittance is the product of

the transmittances. The glint radiance correction, which is subtracted from L_t, is then (Wang and Bailey, 2001, Eqns. 4 and 5)

$$T(\theta_v, \lambda)L_g(\theta_v, \lambda) = F_o(\lambda)T(\theta_s, \lambda)T(\theta_v, \lambda)L_{GN},$$

where

$$T(\theta_s, \lambda)T(\theta_v, \lambda) = \exp\left\{-[\tau_R(\lambda) + \tau_a(\lambda)]\left(\frac{1}{\cos\theta_s} + \frac{1}{\cos\theta_v}\right)\right\}, \qquad (7.1)$$

and where $\tau_R(\lambda)$ and $\tau_a(\lambda)$ are the Rayleigh and aerosol optical thicknesses, respectively.

Wang and Bailey (2001) comment (page 4792, left column) that the effects of ozone absorption have already been accounted for before this state of processing. This is now also true for NO_2 absorption.

Note that the glint correction cannot be computed unless the aerosol optical thickness (AOT) τ_a is known. The AOT is obtained in a two-step process. First, the measured $L_t(\lambda)$ and the wind speed W are used to get a first estimate $\tau_a^{(1)}(\lambda)$ of the AOT. This estimate is obtained using the aerosol correction algorithms described in Chapter 9. This estimate is then used in Eq. (7.1), and the glint-corrected TOA radiance is then computed as

$$L'_t(\lambda) = L_t(\lambda) - F_o(\lambda)T(\theta_s, \lambda)T(\theta_v, \lambda)L_{GN}. \qquad (7.2)$$

This gives the initial estimate $L_t^{(1)'}(\lambda)$ of $L'_t(\lambda)$. This value is then used again in the AOT algorithm to obtain the second estimate $\tau_a^{(2)}(\lambda)$ for the AOT. The second AOT estimate is then used again in Eqs. (7.1) and (7.2) to obtain an improved estimate $L_t^{(2)'}(\lambda)$. In practice, only two iterations give a satisfactory final estimate for the AOT, $\tau_a(\lambda) = \tau_a^{(2)}(\lambda)$, and thus for the glint-corrected TOA radiance. This final $\tau_a(\lambda)$ is then used to compute the aerosol contribution to the TOA radiance, as described in Chapter 9.

Whitecaps

The contribution of white caps and foam to the TOA radiance depends on two factors: the reflectance of whitecaps per se and the fraction of the sea surface that is covered by whitecaps.

Following Gordon and Wang (1994b), the contribution of whitecaps and foam at the TOA is (recall Eq. 3.13)

$$t(\theta_v, \lambda)\rho_{wc}(\lambda) = [\rho_{wc}(\lambda)]_N \, t(\theta_s, \lambda) \, t(\theta_v, \lambda) \,,$$

where $t(\theta_v, \lambda)$ is the diffuse atmospheric transmission in the viewing direction, $t(\theta_s, \lambda)$ is the diffuse transmission in the Sun's direction, and $[\rho_{wc}(\lambda)]_N$ is the non-dimensional normalized whitecap reflectance. $[\rho_{wc}(\lambda)]_N$ is defined in the same manner as was the normalized water-leaving radiance $[\rho_w(\lambda)]_N$ in §3, namely

$$[\rho_{wc}]_N \equiv \frac{\pi}{F_o}[L_{wc}]_N = \pi\frac{\left(\frac{R}{R_o}\right)^2 L_{wc}(\theta_s)}{F_o \, \cos\theta_s \, t(\theta_s)} \,, \tag{8.1}$$

where L_{wc} is the whitecap radiance. It is assumed that the whitecaps are Lambertian reflectors, so that (unlike for L_w) L_{wc} does not depend on direction θ_v, ϕ. This gives the interpretation (Gordon and Wang, 1994b, page 7754) that "ρ is the reflectance–the reflected irradiance divided by the incident irradiance–that a Lambertian target held horizontally at the TOA would have to have to produce the radiance L." $[\rho_{wc}]_N$ can be interpreted as the average reflectance of the sea surface that results from whitecaps in the absence of atmospheric attenuation.

The effective whitecap irradiance reflectance is taken from Koepke (1984) to be 0.22 (albeit with $\pm 50\%$ error bars). This reflectance is independent of wavelength. This gives $[\rho_{wc}]_N = 0.22F_{wc}$, where F_{wc} is the fraction of the sea surface that is covered by whitecaps. The fractional coverage is taken from Stramska and Petelski (2003), who give two models for for F_{wc}:

$$F_{wc} = 5.0 \times 10^{-5}(U_{10} - 4.47)^3 \qquad \text{for developed seas} \tag{8.2}$$

$$F_{wc} = 8.75 \times 10^{-5}(U_{10} - 6.33)^3 \qquad \text{for undeveloped seas} \tag{8.3}$$

where W is the wind speed in m s^{-1} at 10 m. Formula (8.3) for undeveloped seas is used on the assumption that if the seas are well developed it is probably stormy, hence cloudy, so that remote sensing is not possible. The blue curve in Fig. (8.4) shows F_{wc} for undeveloped seas.
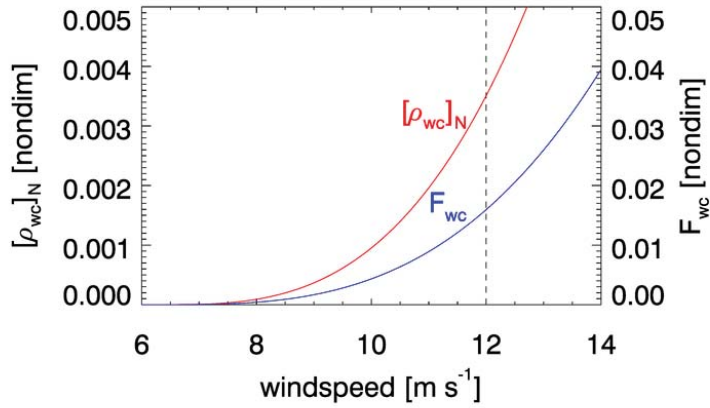
Figure 8.1: Whitecap normalized reflectance as given by Eq. (8.4) with $a_{wc} = 1$, and the fraction of sea surface whitecap coverage as given by Eq. (8.3).

The final model for $[\rho_{wc}]_N$ is then taken to be

$$
\begin{aligned}
[\rho_{wc}]_N(\lambda) &= a_{wc}(\lambda) \times 0.22 \times F_{wc} \\
&= a_{wc}(\lambda) \times 1.925 \times 10^{-5}(U_{10} - 6.33)^3 \, .
\end{aligned}
\tag{8.4}
$$

A whitecap correction is applied for wind speeds in the range $6.33 \leq U_{10} \leq 12$ m s^{-1}. The factor $a_{wc}(\lambda)$ is a normalized whitecap reflectance that describes the decrease in reflectance at red and NIR wavelengths. This factor is taken from Frouin et al. (1996, Figs. 3 and 4); the values are

λ =	412	443	490	510	555	670	765	865
a_{wc} =	1.0	1.0	1.0	1.0	1.0	0.889	0.760	0.645

Linear interpolation is used as needed between these values. Figure 8.1 shows the whitecap reflectance as given by Eq. (8.4) when $a_{wc} = 1$.

Aerosols

9.1 Aerosol Properties

Aerosols are solid or liquid particles that are much larger than gas molecules but small enough to remain suspended in the atmosphere for periods of hours to days or longer. Typical sizes are 0.1 to 10 μm. An aerosol's optical properties are determined by its composition, usually parameterized via its complex index of refraction, and its particle size distribution (PSD).

For the purposes of atmospheric correction, aerosol particle size distributions are modeled as a sum of "fine" (small; radii less than roughly 1 μm) and "coarse" (large; radii greater than roughly 1 μm) particles, with a log-normal distribution for each. (The log-normal distribution is reviewed in Campbell (1995).) The cumulative volume distribution is then (Ahmad et al., 2010a)

$$\frac{dV(r)}{d\ln r} = \sum_{i=1}^{2} \frac{V_{oi}}{\sqrt{2\pi}\sigma_i} \exp\left[-\left(\frac{\ln r - \ln r_{voi}}{\sqrt{2}\sigma_i}\right)^2\right].$$

Here $V(r)$ is the volume of particles per volume of space with size less than or equal to r; $V(r)$ is typically specified as μm^3 cm^{-3}. r_{voi} is the volume geometric mean radius, and σ_i is geometric standard deviation for class i. The integral of $dV(r)/d\ln r$ over all sizes $r = 0$ to ∞ (i.e., $\ln r$ from $-\infty$ to ∞) gives $V(\infty) = V_{oi}$. Thus V_{oi} is the total volume of particles of class i per volume of space.

A similar equation holds for the cumulative number distribution $dN(r)/d\ln r$, where $N(r)$ is the number of particles per volume of space with size less than or equal to r. The corresponding parameters r_{noi} and N_{oi} can be obtained from r_{voi} and V_{oi}; see the equations in Ahmad et al. (2010a). The particle size distribution (PSD) is given by

$$n(r) = \frac{dN(r)}{dr} = \frac{1}{r}\frac{dN(r)}{d\ln r},$$

where $n(r)dr$ is the number of particles per unit volume in size range r to $r + dr$. The units for $n(r)$ are usually expressed as particles m^{-3} μm^{-1}.

Figure 9.1 illustrates shapes of the volume $V(r)$, number $N(r)$, and particle size $n(r)$ distributions for an open ocean aerosol, computed using the parameter values of Ahmad et al. (2010a,
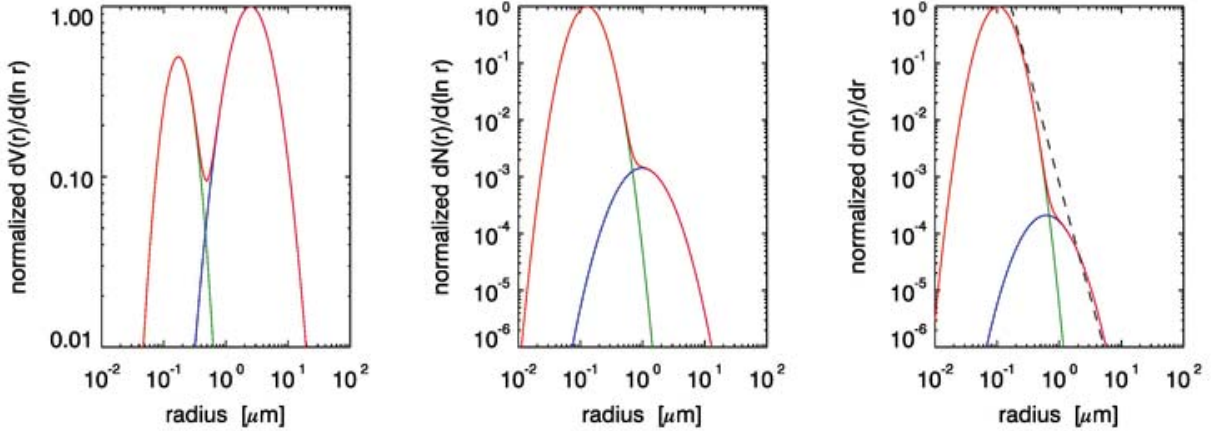
Figure 9.1: Illustration of aerosol volume, number, and particle size distributions. The parameter values are for an open-ocean aerosol. The green curve is fine particles; blue is coarse particles; red is the sum of fine and coarse particles. Each total curve is normalized to 1 at its maximum value.

Table 2). The distributions of the fine aerosols are given by the green lines. The blue lines are the coarse aerosols, and the red lines are the sums. The two roughly comparable distributions of left panel of the figure show that the fine and coarse aerosols each contribute a significant amount of the total particle volume. In the present example the fines are 25.7% of the total volume and the coarse particles are 74.3% of the total volume. The middle panel shows that the fines dominate the number of particles; in the present case there are 477 times as many fine particles as coarse. The right panel shows the PSD. The black dashed line shows the -4 slope of a Junge distribution for comparison.

The radius parameter r_{voi} and index of refraction both depend on the aerosol type (dust, sea salt, soot, etc.) and on the relative humidity Rh. The index of refraction generally depends on wavelength. Figure 9.2 shows the effect of relative humidity on cumulative volume and particle size distributions for an open-ocean aerosol (parameter values from Ahmad et al. (2010a, Table 4)). Note that as Rh increases, the particles absorb more water and increase in size, so the distributions shift to the right. The shape of the distribution also changes with Rh.

As modeled in Ahmad et al. (2010a), the fine particles are generally of "continental" origin and include both dust and soot. The fine particles are sometimes absorbing. The coarse particles are of "oceanic" origin and are assumed to be non-absorbing sea salts. The tables in Ahmad et al. (2010a) give the PSD parameters and indices of refraction for different aerosol types (dust, sea salt, soot, etc.) and relative humidities. (Note that Table 1 of Ahmad et al. (2010a) has errors. The corrected table is given in Ahmad et al. (2010b).)

An aerosol's physical properties determine its optical properties, namely its mass-, number-, or volume-specific absorption $a^*(\lambda)$ and scattering $b^*(\lambda)$ coefficients and scattering phase function $\tilde{\beta}(\psi, \lambda)$, where ψ is the scattering angle. If the particles are homogeneous spheres, Mie theory can be used to compute the optical properties from the physical properties. This is often done, although the assumption of homogeneous spherical particles may or may not be valid in a given situation. In any case, once the $a^*(\lambda)$ and scattering $b^*(\lambda)$ coefficients are known, then given the concentration
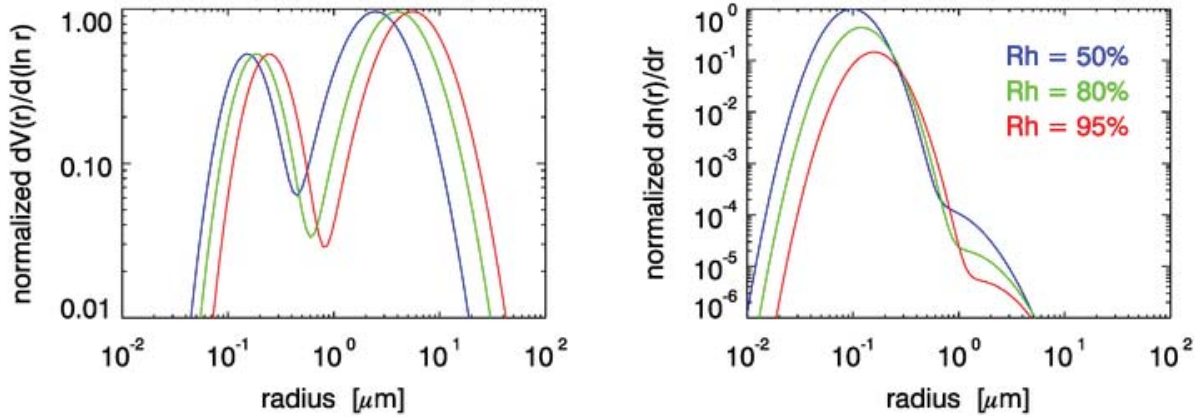
51

Figure 9.2: Effect of relative humidity Rh on the cumulative volume and particle size distributions for a typical open-ocean aerosol. The curves in each panel are normalized to 1 at the maximum value of the three curves.

profile $Conc(z)$ as a function of altitude z, the extinction coefficient $c(z, \lambda) = Conc(z)[a^*(\lambda) + b^*(\lambda)]$ can be computed. The aerosol optical thickness or aerosol optical depth is then given by

$$\tau_a(\lambda) = \int_{z_0}^{TOA} c(z, \lambda) dz\,,$$

where z_0 is the surface elevation. (Generally $z_0 = 0$ for mean sea level, but may also be the elevation of a lake.)

For all else held fixed, the aerosol optical thickness at wavelength λ is approximately related to the value at a reference wavelength λ_o by

$$\frac{\tau_a(\lambda)}{\tau_a(\lambda_o)} = \left(\frac{\lambda_o}{\lambda}\right)^\alpha \tag{9.1}$$

The parameter α is known as the Ångström exponent or Ångström coefficient. Smaller (larger) particles generally have a larger (smaller) Ångström exponent.

The single scattering albedo ω_o defined by

$$\omega_o(\lambda) = \frac{b^*(\lambda)}{c^*(\lambda)}$$

is also of use in modeling the optical effects of aerosols on the radiance distribution.

Ahmad et al. (2010a) constructed look-up-tables (LUTs) for 10 aerosol types and 8 relative humidities, for a total of 80 aerosol tables. The fine fraction was a mixture of 99.5% dustlike and 0.5% soot particles (not modeled by Shettle and Fenn) for all 10 aerosol types, which gives good agreement on average with AERONET measurements of aerosol optical properties. The ten aerosol models have different weights of fine and coarse particles, but the effective radius r_{eff} ($r_{\text{eff}} = \int r^3 n(r) dr / \int r^2 n(r) dr$) and mean radius μ_o ($\mu_o = \int r n(r) dr / \int n(r) dr$) are the same. The aerosol types were then defined by letting the fine-to-coarse fraction vary from 0 to 1. For each

aerosol type, relative humidities of $Rh = 30, 50, 70, 75, 80, 85, 90$, and 95% were used. The actual aerosol LUTs contain the components of the model from which to derive single-scattering aerosol reflectance ratios in each band (relative to any reference band), plus a set of quadratic coefficients relating single to multiple scattering (as in Gordon and Wang (1994a)), plus a separate table of Rayleigh-aerosol diffuse transmittance coefficients of the form $t = A\exp(-B\tau_a)$ (recall Eq. 4.6). Mie is theory used to compute the aerosol phase functions for use in the radiative transfer model.

9.2 Black-pixel Calculations

The algorithm developed by Gordon and Wang (1994a) is used, although the original aerosol models and LUTs have been updated as described in Ahmad et al. (2010a), and model selection is now partitioned by relative humidity (RH). (Gordon and Wang ignored the glint term since they were considering SeaWiFS, whose viewing direction was chosen to avoid direct Sun glint.)

Beginning with Eq. (3.13),

$$\rho_t = \rho_R + [\rho_a + \rho_{Ra}] + T\rho_g + t\rho_{wc} + t\rho_w, \tag{9.2}$$

The basic theory in Gordon and Wang (1994a) is developed using single-scattering theory, in which case the ρ_{Ra} term is zero because there is no multiple scattering. Multiple-scattering effects are then added via numerical models using the guidance of the single-scattering theory.

Assume that the corrections for Rayleigh, whitecaps, O_3, NO_2, and Sun glint have all been made. Then the left hand side of

$$\rho_t - \rho_R - T\rho_g - t\rho_{wc} = [\rho_a + \rho_{Ra}] + t\rho_w \tag{9.3}$$

or

$$\rho_{Aw} \equiv \rho_A + t\rho_w$$

is known. Here ρ_{Aw} is just convenient shorthand for the measured TOA reflectance ρ_t with the Rayleigh and other effects removed. The next task is to compute ρ_A, the combined aerosol and aerosol-Rayleigh reflectance, and move it to the left hand side, after which the desired ρ_w will be known.

Low-chlorophyll, Case 1 waters have negligible water-leaving radiance at near-infrared (NIR) wavelengths, i.e. beyond roughly 700 nm. For such waters, it can be assumed that $\rho_w(\lambda > 700 \text{ nm}) = 0$, which is known as the "black-pixel" assumption. Let λ_1 and λ_2 be two NIR wavelengths, with $\lambda_1 < \lambda_2$. At these two wavelengths, the TOA normalized reflectance (corrected as shown in Eq. (9.3)) is due entirely to atmospheric path radiance: $\rho_{Aw}(\lambda_i) = \rho_A(\lambda_i), i = 1, 2$. Table 9.1 shows the λ_1 and λ_2 bands for several sensors.

Now consider the ratio

$$\epsilon(\lambda_1, \lambda_2) \equiv \frac{\rho_A(\lambda_1)}{\rho_A(\lambda_2)} \underset{\text{Black Pixel}}{=} \frac{\rho_{Aw}(\lambda_1)}{\rho_{Aw}(\lambda_2)} \tag{9.4}$$

The quantity $\epsilon(\lambda_1, \lambda_2)$, and more generally the quantity $\epsilon(\lambda, \lambda_2)$ for any $\lambda < \lambda_2$, depends on the aerosol type, which is determined by the particle type, PSD, and relative humidity. Figure 9.3 shows the dependence of $\epsilon(\lambda, \lambda_2 = 865)$ for the ten aerosol models, for one particular set of solar zenith angle, viewing direction, and relative humidity.

For the given image pixel being corrected, the process is as follows:

Table 9.1: NIR bands used for aerosol correction.

Band Label	Wavelengths [nm]	Nominal Wavelength [nm]
SeaWiFS		
7	745-785	$\lambda_1 = 765$
8	845-855	$\lambda_2 = 865$
MODIS		
15	743-753	$\lambda_1 = 748$
16	862-877	$\lambda_2 = 869$
VIIRS		
M6	739-754	$\lambda_1 = 745$
M7	846-885	$\lambda_2 = 862$

- The relative humidity RH is taken from NCEP.

- For each bounding RH value in the family of 8 RH values in the database, the corresponding family of 10 aerosol types in the database is then searched to find the two aerosols types whose precomputed values of $\epsilon(\lambda_1, \lambda_2)$, call them ϵ_{low} and ϵ_{high}, bracket the measured value of $\epsilon(\lambda_1, \lambda_2)$ for the given Sun and viewing geometry.

- This selects two of the curves like those of Fig. 9.3, for which the corresponding $\epsilon(\lambda, \lambda_2)$ and τ_a values have been precomputed and stored in the aerosol LUT.

- It is assumed that the difference in the precomputed $\epsilon(\lambda, \lambda_2)$ is at all wavelengths in the same proportion as the measured $\epsilon(\lambda_1, \lambda_2)$ is to the bracketing values at the NIR reference wavelengths. Thus let

$$\Delta = \frac{\epsilon(\lambda_1, \lambda_2) - \epsilon_{\text{low}}(\lambda_1, \lambda_2)}{\epsilon_{\text{high}}(\lambda_1, \lambda_2) - \epsilon_{\text{low}}(\lambda_1, \lambda_2)} \tag{9.5}$$

- The aerosol reflectance at all wavelengths is then computed from the measured $\rho_{\text{Aw}}(\lambda_2)$ and the tabulated ϵ_{low} and ϵ_{high} values using

$$\rho_A(\lambda) = [(1 - \Delta)\epsilon_{\text{low}}(\lambda, \lambda_2) + \Delta\epsilon_{\text{high}}(\lambda, \lambda_2)] \rho_{\text{Aw}}(\lambda_2) \tag{9.6}$$

Now that $\rho_A(\lambda)$ is known, Eq. (9.3) gives

$$t\rho_w = \rho_{\text{Aw}} - \rho_A = \rho_t - \rho_R - T\rho_g - t\rho_{wc} - [\rho_a + \rho_{Ra}] \tag{9.7}$$

Recall that t is the diffuse transmission in the viewing direction, and that $t\rho_w$ is the contribution of water-leaving radiance (in reflectance form) at the TOA. The desired ρ_w at the sea surface is thus obtained from

$$\rho_w = \frac{\rho_{\text{Aw}} - \rho_A}{t} . \tag{9.8}$$

The aerosol optical depth is computed at all wavelengths using the values of $\tau(\lambda_2)$ and the Ångström exponent in Eq. (9.1).

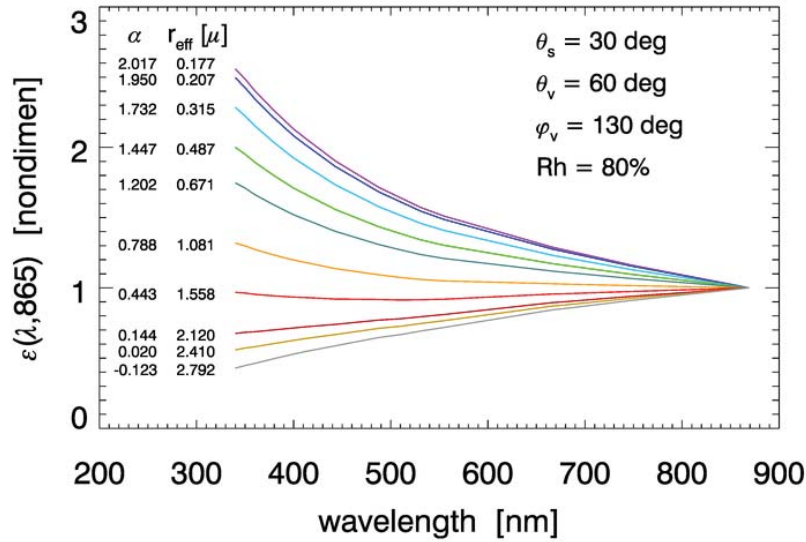This technique rests on two main assumptions:

54

Figure 9.3: Dependence of $\epsilon(\lambda, \lambda_2 = 865)$ on aerosol model. The aerosol model is determined by the value of the Ångström exponent α and the effective particle size r_{eff}. All curves are for a particular sun zenith angle θ_{s}, viewing direction $\theta_{\text{v}}, \phi_{\text{v}}$, and relative humidity RH, as shown.

- The water-leaving radiance is negligible at the NIR reference wavelengths. This is valid only for optically deep, Case 1 waters, with a chlorophyll concentration of 0.3 mg m^{-3} or less. Waters containing higher chlorophyll concentrations or mineral particles will violate this assumption. Figure 9.4 shows an example of very turbid water for which the remote-sensing reflectances at NIR wavelengths is not negligible.

- The aerosols are not strongly absorbing. Some mineral aerosols absorb strongly at blue wavelengths but not in the NIR. Their $\epsilon(\lambda, \lambda_2)$ functions look like the black curve in Fig. 9.5. Thus their presence cannot be detected from the NIR TOA radiances.

Note that these are unrelated assumptions: the water can have non-zero NIR reflectance and the atmosphere can have non-absorbing aerosols, or there can be zero NIR reflecance but absorbing aerosols. If the water-leaving radiance is not zero at the λ_2 reference wavelength, then the ρ_w contribution to ρ_{Aw} will be interpreted as a larger aerosol concentration. This leads to over-correction for the aerosol, i.e, subtracting too much ρ_A from ρ_{TOA}. The resulting ρ_{w} is then too small, and can even be negative at blue wavelengths. Likewise, if the aerosol is blue-absorbing, over-correction occurs at blue wavelengths and, again, ρ_{w} is too small or even negative at blue wavelengths.
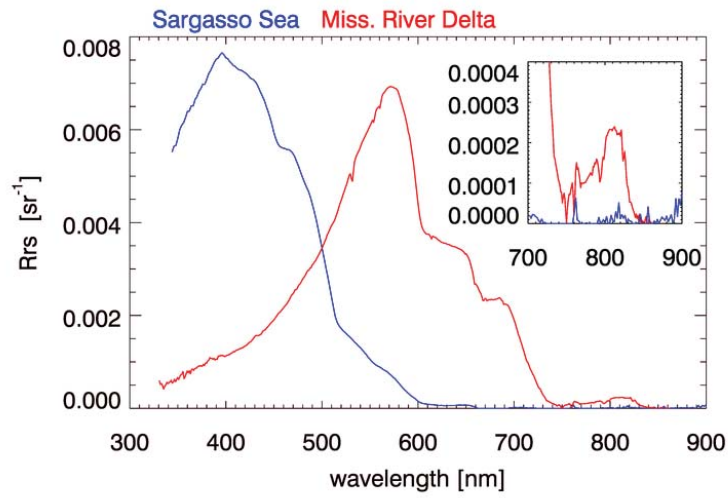
Figure 9.4: Examples of Rrs for Case 1 and Case 2 waters. Rrs is not zero in the NIR for the Mississippi River Delta water.
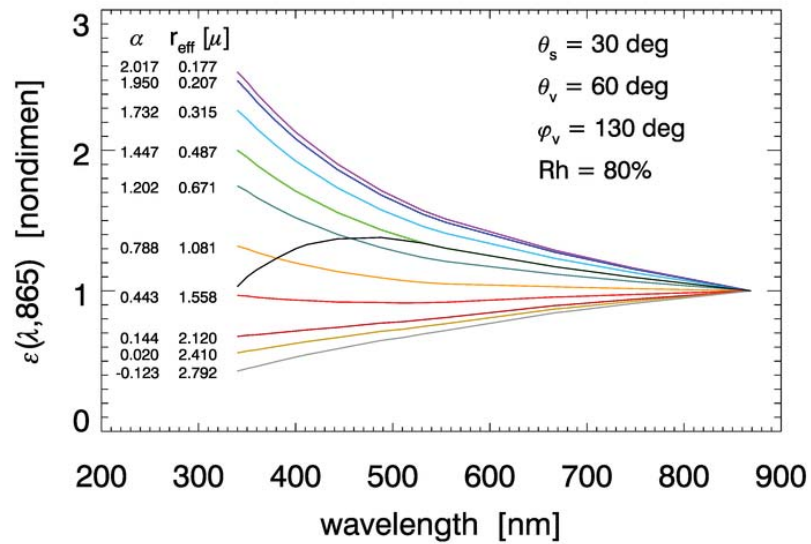

Figure 9.5: Qualitative behavior of $\epsilon(\lambda, \lambda_2 = 865)$ for a blue-absorbing aerosol (black curve).

9.3 Non-black-pixel Calculations

Many ways to treat non-black pixels have been developed; the method currently implemented by the OBPG is described in Bailey et al. (2010). This algorithm works as follows.

It is necessary to estimate $R_{rs}(\lambda)$ (or equivalently $\rho_w(\lambda)$) at the NIR reference wavelengths so that the non-zero water-leaving radiance can be removed from the TOA signal, leaving only the aerosol reflectance as the contribution to ρ_{Aw}, from which the aerosol type (i.e., $\epsilon(\lambda, \lambda_2)$) can be determined. However, $R_{rs}(NIR)$ can't be estimated until the aerosol contribution is removed. Thus an iterative solution must be used to obtain both $R_{rs}(NIR)$ and the aerosol type.

The remote-sensing reflectance can be written

$$R_{rs}(\lambda) = \frac{f(\lambda)}{Q(\lambda)} \frac{b_b(\lambda)}{a(\lambda) + b_b(\lambda)}. \tag{9.9}$$

As discussed in detail in §3, the f/Q factor describes the angular distribution of the water-leaving radiance, i.e., the BRDF of the ocean. This factor depends on the Sun and sky radiance distribution (parameterized by the solar zenith angle θ_s and AOT τ_a), water-column IOPs (parameterized by the chlorophyll concentration Chl in Case 1 waters), sea state (wind speed W), viewing direction (θ_v, ϕ_v), and wavelength. It has been extensively studied and numerically modeled by Morel et al. (2002), who present tabulated values as functions of $\theta_s, \tau_a, \theta_v, \phi_v, Chl, W$, and λ. Although the Morel et al. (2002) f/Q table was generated for Case 1 waters, analysis shows (Bailey et al., 2010) that it is often adequate for Case 2 waters as well. The f/Q factor is thus considered known for the present calculations.

The iterative correction for waters where the black-pixel assumption cannot be made has the following steps:

1. Assume that $R_{rs}(765)$ and $R_{rs}(865)$ are both 0, i.e. make the black-pixel assumption for both NIR reference bands.

2. Complete the atmospheric correction process as described in §9.2. This gives the initial estimate of $\rho_w(\lambda)$, or equivalently $R_{rs}(\lambda)$.

3. Use $R_{rs}(443)$ and $R_{rs}(555)$ from the initial estimate of $R_{rs}(\lambda)$ to get η by the empirical relationship (Lee et al. (2010, Eq. 8); Bailey et al. (2010, Eq. 3))

$$\eta = 2 \left[1 - 1.2 \exp \left(0.9 \frac{R_{rs}(443)}{R_{rs}(555)} \right) \right]. \tag{9.10}$$

4. Use the initial $R_{rs}(\lambda)$ to get an initial estimate of the chlorophyll concentration Chl. The particular algorithm used to obtain Chl from $R_{rs}(\lambda)$ depends on the sensor.

5. Use this Chl to obtain $a(670)$ via the empirical relationship (Bailey et al., 2010, Eq. 4)

$$a(670) = \exp[0.9389 \ln(Chl) - 3.7589] + a_w(670). \tag{9.11}$$

where the $a_w(670) = 0.439$ m^{-1} is the absorption by pure water.

6. Use $a(670)$ and $R_{rs}(670)$ in Eq. (9.9) to solve for $b_b(670) = b_{bw}(670) + b_{bp}(670)$, where $b_{bw}(670) = 4.26 \times 10^{-4}$ m^{-1} is the backscatter coefficient for pure sea water.

7. Use η from Eq. (9.10) and (Bailey et al., 2010, Eqs. 2b,3) to compute $b_{\mathrm{b}}(765)$:

$$b_{\mathrm{b}}(765) = b_{\mathrm{bw}}(765) + b_{\mathrm{pb}}(670) \left(\frac{670}{765}\right)^{\eta} \tag{9.12}$$

where $b_{\mathrm{bw}}(765) = 2.38 \times 10^{-4}$ m^{-1}. $b_{\mathrm{b}}(865)$ is computed in the same manner using $b_{\mathrm{bw}}(865) = 1.41 \times 10^{-4}$ m^{-1}.

8. Use this $b_{\mathrm{b}}(765)$ and $a(765) = a_{\mathrm{w}}(765) = 2.85$ m^{-1} to get $R_{rs}(765)$ from Eq. (9.9). Similarly, compute $R_{rs}(865)$ using $b_{\mathrm{b}}(865)$ and $a_{\mathrm{w}}(865) = 4.61$ m^{-1}.

9. Use the new, non-zero value of $R_{\mathrm{rs}}(765)$ (i.e. $\rho_{\mathrm{w}}(765)$) to remove the non-zero $\rho_{\mathrm{w}}(765)$ contribution to $\rho_t(765)$. Do the same calculation for 865 nm.

10. Return to Step 2 and repeat the atmospheric correction using the black-pixel algorithm. This will give a new (hopefully better) estimate of $R_{\mathrm{rs}}(\lambda)$, thus an new estimate of the other parameters, and finally new estimates of $R_{\mathrm{rs}}(765)$ and $R_{\mathrm{rs}}(865)$ at Step 8. After using the new values of $\rho_{\mathrm{w}}(765)$ and $\rho_{\mathrm{w}}(865)$ to correct for the non-zero water contribution to $\rho_t(765)$ and $\rho_t(865)$, return to Step 2 for a new iteration. Continue iterating until the change in $R_{\mathrm{rs}}(765)$ from one iteration to the next is less than 2%, which typically takes 2-4 iterations, or when 10 iterations have been made.

If this iteration process fails to converge within 10 cycles, then re-initialze with $\rho_{\mathrm{a}}(NIR) = 0$, i.e., set the NIR aerosol contribution to zero. This implies that all of the NIR reflectance is due to the water (after correction for Rayleigh and Sun glint). Repeat the iteration until convergence is reached. If convergence is still not reached, do one more calculation with $\rho_{\mathrm{a}}(NIR) = 0$ and flag the pixel as "atmospheric correction warning." However, even in this case, the retrieval may still be useful.

The above iteration is not done if the initial Chl estimate is less that 0.3 mg m^{-3}, and it is always done if the initial Chl estimate is greater that 0.7 mg m^{-3}. To prevent discontinuities in the final results, the $R_{\mathrm{rs}}(765)$ estimate is linearly weighted from 0 to 1 for $0.3 \leq Chl \leq 0.7$. Figure 9.6 shows the regions of the ocean where the non-black-pixel algorithm is likely to be applied.

Finally, rather than the exact NIR reference wavelengths of $\lambda_1 = 765$ and $\lambda_2 = 865$ shown above, in practice band-averaged IOP values are used for the particular sensor. Thus for VIIRS-NPP, the reference bands are centered at 745 and 862 nm, with the band-averaged $a_{\mathrm{w}}(745) = 2.806$ m^{-1}, and so on. Band averaged IOPs for different sensors are given at `http://oceancolor.gsfc.nasa.gov/DOCS/RSR_tables.html`.
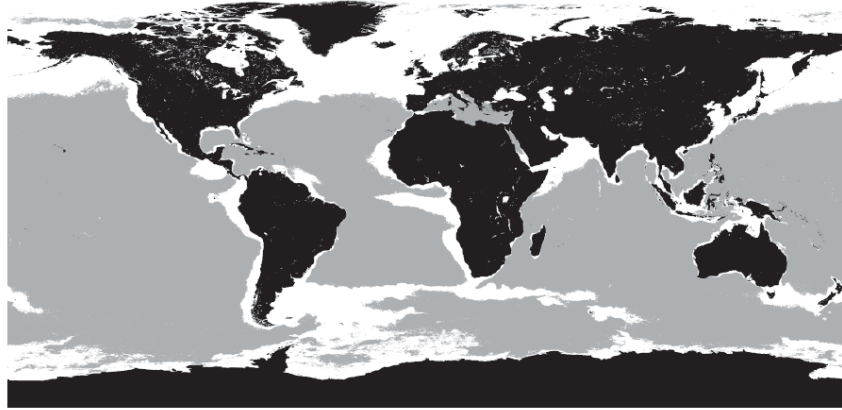
Figure 9.6: Regions of the ocean where the non-black-pixel correction is likely to be applied, based on SeaWiFS climatology. Land is black, gray is $Chl < 0.3$ mg m^{-3} (where the correction is not applied), and white is $Chl > 0.3$ mg m^{-3} (where the correction is applied). [Fig. 3 of (Bailey et al., 2010)]

9.4   Strongly Absorbing Aerosols

The aerosol models of Ahmad et al. (2010a) discussed in Section 9.2 include a small fraction of absorbing soot for the fine part of the aerosol size distribution. These aerosol models are used for routine correction for aerosols. These models, however, cannot account for the presence of strongly absorbing aerosols, which frequently occur in coastal regions downwind from continents, and even in mid-ocean regions because winds can transport fine dust particles long distances.

Strongly absorbing aerosols (especially at blue wavelengths) have been a topic of much research over the years (Gordon et al., 1997b, e.g.). However, as was illustrated in Fig. 9.5, there is no reliable way to detect the presence of absorbing aerosols from the NIR bands of Table 9.1 during the atmospheric correction process. Therefore, all pixels are processed using the algorithms for non- or weakly absorbing aerosols as described in the previous sections.

Spectral Out-of-band Correction

Figure 10.1 shows the sensor response functions (SRF) of the MODIS-Aqua bands used for ocean color remote sensing; each response function is normalized to 1 at its maximum. Visually, in this plot with a linear ordinate axis, the bands appear to be well defined and narrow, with full-width, half-maximum (FWHM; the wavelengths at which the function is one-half of its maximum) widths of 10 to 15 nm. However, when plotted with a logarithmic ordinate as in Fig. 10.2, it is seen that there is significant "out-of-band" (OOB) sensitivity; i.e., a non-zero response outside the nominal band width. In each plot, the black curve represents a TOA radiance with a wavelength dependence of λ^{-4}.

Rayleigh scattering with a λ^{-4} dependence dominates the total TOA radiance. If a radiance with such a wavelength dependence is measured by sensors having the response functions shown in Figs. 10.1 and 10.2, the total measured radiance in the ith band over the 380-1100 nm range shown in the figures will be (Gordon, 1995, Eq. 8)

$$L_i(\text{total}) = \frac{\int_{380}^{1100} L_{\text{TOA}}(\lambda)\, SRF_i(\lambda)\, d\lambda}{\int_{380}^{1100} SRF_i(\lambda)\, d\lambda} \, .$$

Define the "in-band" part of the total signal to be the part detected between chosen lower (λ_{low}) and upper (λ_{up}) wavelengths. The OBPG uses the wavelengths at which the SRF drops to 0.1% of its maximum value to define the lower and upper boundaries of the in-band region. For the nominal 488 nm band, for example, $\lambda_{\text{low}} = 460$ nm and $\lambda_{\text{up}} = 503$ nm. (The FWHM boundaries for the 488 nm band are $\text{FWHM}_{\text{low}} = 482$ nm and $\text{FWHM}_{\text{up}} = 493$ nm.) The part of the measured radiance that comes from in-band wavelengths is then

$$L_i(\text{in band}) = \frac{\int_{\lambda_{\text{low}}}^{\lambda_{\text{up}}} L_{\text{t}}(\lambda)\, \text{SRF}_{\text{i}}(\lambda)\, d\lambda}{\int_{380}^{1100} \text{SRF}_{\text{i}}(\lambda)\, d\lambda} \, , \tag{10.1}$$

with similar equations for the out-of-band contributions at wavelengths less than λ_{low} and greater than λ_{up}. Numerical integration shows that for a λ^{-4} TOA radiance and the nominal 488 nm band, 99.24% comes from the in-band wavelengths, 0.55% comes from out-of-band response at wavelengths less than $\lambda_{\text{low}} = 460$ nm, and 0.20% comes from out-of-band response at wavelengths greater than $\lambda_{\text{up}} = 503$ nm. For the 866 nm band, the corresponding numbers are 99.22% in-band,
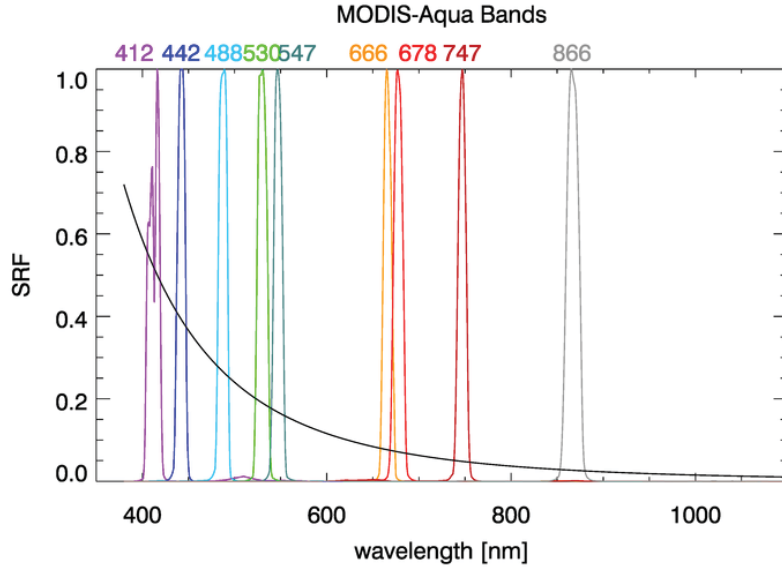
Figure 10.1: Relative sensor response functions (SRF) for the MODIS-Aqua bands used for ocean color remote sensing. The black curve represents a TOA radiance proportional to λ^{-4}. (Data from from http://oceancolor.gsfc.nasa.gov/DOCS/RSR_tables.html)
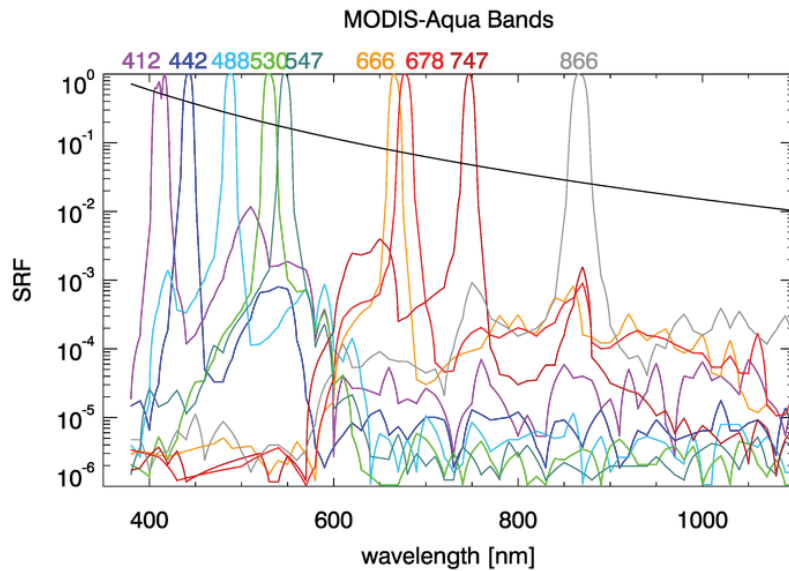

Figure 10.2: Same as Fig. 10.1 except that the ordinate axis is logarithmic to show the out-of-band response.
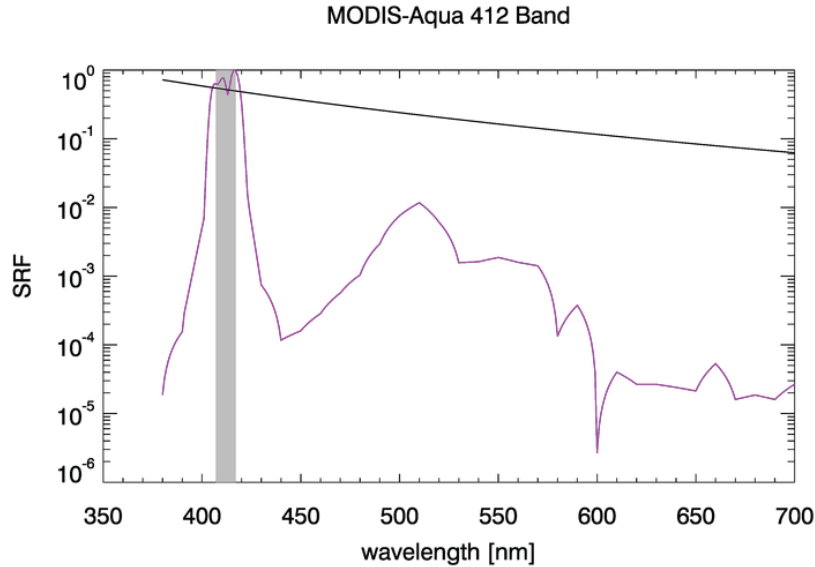
Figure 10.3: The MODIS-Aqua relative sensor response (purple) and a perfect sensor with a 10-nm FWHM (gray shading). The black line represents a radiance proportional to λ^{-4}.

0.63% from wavelengths less than $\lambda_{\text{low}} = 843$ nm, and 0.16% comes from wavelengths greater than $\lambda_{\text{up}} = 891$ nm. Thus, for the MODIS-Aqua bands, almost 1% of the TOA radiance attributed to a nominal bandwidth actually comes from outside that band. This magnitude of misattribution of radiances between bands is significant and requires correction for proper interpretation of measured data.

Gordon (1995) points out that the OOB corrections must be applied separately to the individual components of the TOA radiance because the OOB response depends on the spectral shape of the radiance. That is, separate corrections must be applied to the Rayleigh, aerosol, and water-leaving radiances. Those corrections are built into the sensor-specific Rayleigh and aerosol LUTs described above. This section describes how the OOB correction is applied to the remote-sensing reflectance R_{rs} after the preceding steps of the atmospheric correction process have been carried out.

It should be noted that OOB corrections are also required when comparing measurements made by sensors having different spectral responses. This happens, for example, when comparing a nominal MODIS 412 nm band value with an in-situ measurement made by a multispectral radiometer having a nominal 412 band. The filters in the MODIS and in situ radiometer instruments will not have exactly the same spectral responses or nominal bandwidths. In general, it is desirable to reference any measurement to what would be obtained by an ideal sensor with a perfect response function defined by the nominal FWHM. This is illustrated in Fig. 10.3 for the MODIS-Aqua 412 band and a sensor with a perfect "top hat" response for $407 \leq \lambda \leq 412$ nm. For a radiance with a λ^{-4} wavelength dependence, 18.1% of the MODIS nominal 412 band response comes from $\lambda < 407$, 60.5% comes from within the nominal 10 nm bandwidth of the perfect sensor, and 21.4% comes from $\lambda > 412$ nm.

Figure 10.4 shows $R_{\text{rs}}(\lambda)$ as computed for Case 1 water using a model of the type developed in Morel and Maritorena (2001) for $K_d(\lambda)$ and $R((\lambda)$.
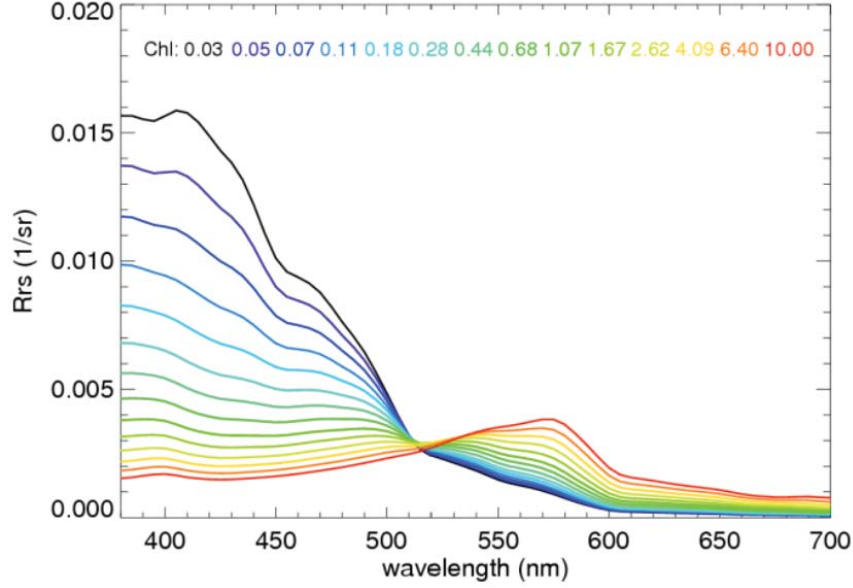
Figure 10.4: $R_{\text{rs}}(\lambda)$ spectra as functions of the chlorophyll concentration.

For each nominal sensor band labeled by $\lambda_i, i = 1, ..., N_{\text{bands}}$, and for each chlorophll value $Chl_j, j = 1, ..., N_{\text{Chl}}$, the $R_{rs}(\lambda)$ spectra of Fig. 10.4 are used in equations of the form of (10.1) with appropriate integration limits to compute:

- $R_{rs}^{11}(\lambda_i, Chl_j)$ = The mean R_{rs} over idealized 11-nm bandwidths (center wavelength ± 5 nm) corresponding to the nominal satellite bands (as illustrated by the gray 412 nm band in Fig. 10.3)

- $R_{rs}^{\text{full}}(\lambda_i, Chl_j) = R_{rs}$ computed using the full spectral response function for the ith sensor band.

- The ratio

$$r(\lambda_i, Chl_j) = \frac{R_{rs}^{11}(\lambda_i, Chl_j)}{R_{rs}^{\text{full}}(\lambda_i, Chl_j)}. \tag{10.2}$$

Figure 10.5 illustrates the results of these calculations for the SeaWiFS nominal 555 nm band. This figure shows chlorophyll values only for $Chl <= 3$ mg m^{-3}, which was felt to be the upper limit of reliability of the chlorophyll-based $R_{\text{rs}}(\lambda)$ model of Fig. 10.4. A similar figure can be drawn for each sensor band. If the chlorophyll concentration were known, a rearrangement of Eq. (10.2) and ratio curves like that of Fig. 10.4 could be used to compute the correction to the measured R_{rs}^{full} for the ith band.

However, the chlorophyll concentration is not yet known. To proceed, the $r(\lambda_i, Chl_j)$ curves like the one shown by the blue line of Fig. 10.5 are used to compute correction factors $r(\lambda_i)$ as functions of the ratio of the uncorrected $R_{\text{rs}}(490$ nm) to the uncorrected $R_{\text{rs}}(555$ nm). Each chlorophyll value shown in figures like 10.5 for the various bands gives a point like those shown in Fig. 10.6 for $r(555)$ vs. the uncorrected $R_{\text{rs}}(490)/R_{\text{rs}}(555)$. A corresponding set of $r(\lambda_i)$ points is computed for each band, but in each case as a function of $R_{\text{rs}}(490)/R_{\text{rs}}(555)$. (This choice of the ratio of 490 to 555 nm
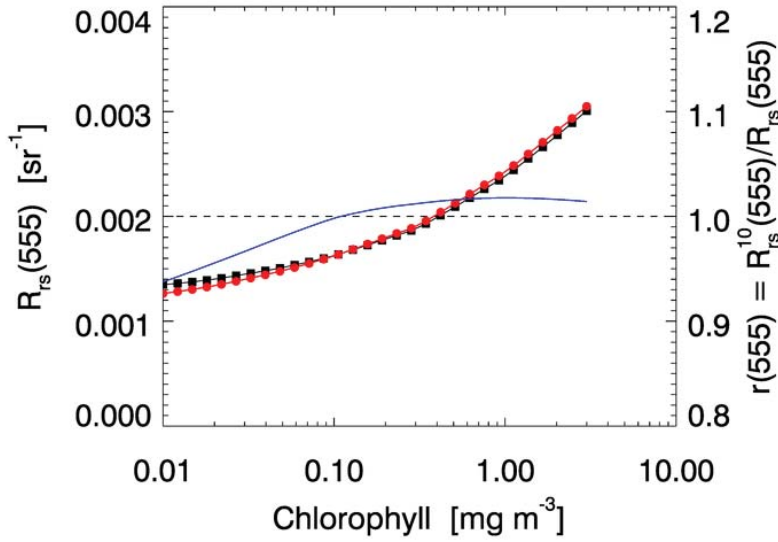
Figure 10.5: $R_{\rm rs}^{11}(\lambda_{555}, Chl_j)$ (red dots), $R_{\rm rs}^{\rm full}(\lambda_{555}, Chl_j)$ (black squares), and the ratio $r(\lambda_{555}, Chl_j)$ (blue line, right ordinate axis) for the SeaWiFS nominal 555 nm band.

for the independent variable traces back to SeaWiFS, for which these were the most trustworthy bands.) A best-fit function to the set of points so generated is then found for each of the $r(\lambda_i)$ vs. $R_{\rm rs}(490)/R_{\rm rs}(555)$ functions.

These functions are then used to apply the OOB correction to the measured $R_{\rm rs}(555)$ values as follows. Given the measured full-band (uncorrected) $R_{\rm rs}(i)$, the value of $R_{\rm rs}(490)/R_{\rm rs}(555)$ is used to evaluate the functional fit to the points of Fig. 10.6 in order to obtain the correction to be applied to the $R_{\rm rs}(555)$ value. The corresponding functions for the other bands are used to correct those bands. For example, the fit to $r(412)$ vs. $R_{\rm rs}(490)/R_{\rm rs}(555)$ is used to correct the 412 nm band, and so on. If the $R_{\rm rs}(490)/R_{\rm rs}(555)$ value is outside the range of the points used for the data fit as illustrated in Fig. 10.6, the value of the nearest point is used, rather than extrapolating with the fitting function beyond the range of the underlying data.

The $R_{\rm rs}(i)$ functions were developed using a Case 1 model for $R_{\rm rs}(\lambda)$ as shown in Fig. 10.4. Case 2 waters can have much different $R_{\rm rs}(\lambda)$ spectra and therefore should have different OOB corrections. However, in practice, Case 2 waters have the same correction applied as for Case 1 waters.

A final comment is warranted regarding the use of this out-of-band correction when comparing satellite-derived and in-situ measurements of $R_{\rm rs}$ (e.g, when doing vicarious calibration):

- If comparing a multispectral satellite band $R_{\rm rs}$ with in an in situ multispectral measurement, perform the OOB adjustment to the satellite data. (Of course, an adjustment should also be made to the in situ values based on the relative spectral responses $SRF(\lambda)$ of the in situ radiometer.)

- If comparing a multispectral satellite band $R_{\rm rs}$ with in an situ hyperspectral measurement that has been filtered with a 10 nm bandpass filter, perform the adjustment.
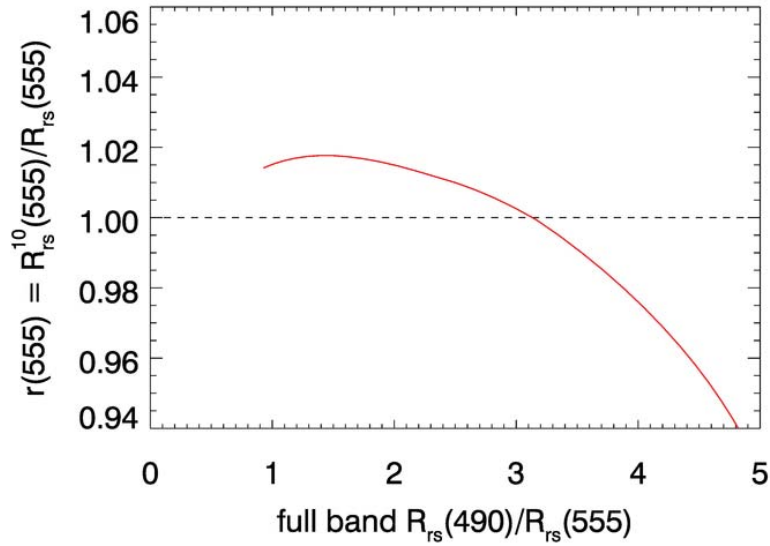
Figure 10.6: Out-of-band correction factor for the SeaWiFS 555 nm band as a function of the ratio of the uncorrected $R_{\mathrm{rs}}(490)$ to $R_{\mathrm{rs}}(555)$.

- If comparing a multispectral satellite band R_{rs} with an in situ hyperspectral measurement that has not been filtered, do not perform the OOB adjustment to the satellite data. However, the hyperspectral in situ spectrum should processed using the satellite sensor $SRF(\lambda)$ spectra. That is, replace the spectrum used in integrals of the form of Eq. (10.1) with the hyperspectral $R_{\mathrm{rs}}(\lambda)$.

Performing the OOB adjustment is the default for processing imagery at OBPG. Therefore, if a user wants to compare satellite data with unfiltered hyperspectral data as in the third bullet above, the standard Level 2 files cannot be used. The user would need to begin with the Level 1b TOA radiances, disable the OOB correction in the atmospheric correction software, and reprocess the TOA radiances to Level 2.

Polarization Correction

Radiance leaving the top of the atmosphere can be strongly polarized even though the sunlight incident onto the TOA is unpolarized. This is because scattering by atmospheric constituents, reflection by the sea surface, and scattering within the water all can generate various states of polarization from unpolarized radiance. Although remote sensing as considered here is based on the total TOA radiance without regard to its state of polarization, many instruments are sensitive to polarization. Therefore, the total TOA radiance they measure may depend on the state of polarization of the TOA radiance and the orientation of the instrument relative to the plane of linear polarization. Correction for these effects is required so that instruments give consistent measurements of the total TOA radiance.

The MODIS sensors are polarization sensitive. MODIS radiance measurements vary by up to $\pm 5.4\%$ for totally linearly polarized radiance, depending of the orientation of the sensor relative to the plane of polarization. This amounts to about $\pm 3\%$ differences in measured TOA radiances for typical values of atmospheric polarization (Meister et al., 2005). These effects must be accounted for in order to achieve the desired 0.5% accuracy in measured TOA radiance. Similarly, the VIIRS instrument polarization sensitivity is 1-2% and requires a polarization correction. SeaWiFS was by design not very sensitive to polarization ($< 0.25\%$), and no polarization correction was applied.

The state of polarization is described by the four-component Stokes vector $[I, Q, U, V]^T$, where superscript T denotes transpose, I is the total radiance without regard for its state of polarization, Q specifies the linear polarization resolved in planes parallel and perpendicular to a conveniently chosen reference plane, U specifies the polarization resolved in planes oriented $\pm 45 \deg$ to the reference plane, and V specifies the right or left circular polarization. The choice of the reference plane for specification of the Q and U components is arbitrary and can be made for convenience. The direction of propagation of the radiance is given by a unit vector $\hat{i}$, so that the Stokes vector can be written as $\boldsymbol{I} = [I, Q, U, V]^T \hat{i}$ when it is desired to indicate both its components and direction. Direction $\hat{i}$ can be specified by the polar (θ) and azimuthal (ϕ) directions in a spherical coordinate system as shown in Fig. 11.1. In that figure, $\hat{\theta}$ and $\hat{\phi}$ are unit vectors specified by the directions of increasing θ ($\theta = 0$ at the pole or $\hat{z}$ direction in a cartesian coordinate system) and increasing ϕ ($\phi = 0$ in a conveniently chosen azimuthal direction such as $\hat{x}$ pointing east or toward the Sun).

In the geophysical setting, it is customary to define the Stoke vector components Q and U with

reference to a plane defined by the normal to the sea surface and the direction of propagation of the radiance. This plane is known as the meridional plane and is partly shaded in light blue in Fig. 11.1. Following the notation and choices of Gordon et al. (1997a), let $\hat{r}_t = \hat{\phi}$ be the reference direction perpendicular to the meridional plane, and let $\hat{l}_t = -\hat{\theta}$ be the reference direction parallel to the meridional plane. The direction of propagation of the radiance to be measured is then $\hat{i} = \hat{r}_t \times \hat{l}_t$. The total TOA radiance resolved in these directions is denoted $\boldsymbol{I}_t = [I_t, Q_t, U_t, V_t]^T \hat{i}$.

This radiance is being measured by a sensor illustrated by the red rectangle in Fig. 11.1. The Stokes vector measured by that sensor has its Q and U components resolved along perpendicular $(\hat{r})$ and parallel $(\hat{l})$ directions chosen for convenience relative to the orientation of the sensor. The sensor will measure the TOA radiance as a Stokes vector $\boldsymbol{I}_m = [I_m, Q_m, U_m, V_m]^T \hat{i}$. For an incident radiance $\boldsymbol{I}$, the optical system comprising the sensor itself and any associated optical components (mirrors, lenses, etc.) will convert the incient radiance into a measured value given by $\boldsymbol{I}_m = \boldsymbol{M}\boldsymbol{I}$, where $\boldsymbol{M}$ is the 4×4 Mueller matrix that describes the optical properties of the sensor optical system. $\boldsymbol{M}$ is defined relative to the sensor reference directions $\hat{r}$ and $\hat{l}$. In order for $\boldsymbol{M}$ to operate on the TOA radiance $\boldsymbol{I}_t$, which is defined with reference directions $\hat{r}_t$ and $\hat{l}_t$, $\boldsymbol{I}_t$ must first be transformed (rotated) from the meridional-based $\hat{r}_t$, $\hat{l}_t$ system to the sensor-based $\hat{r}$, $\hat{l}$ system.

Let $\alpha = \cos^{-1}(\hat{l}_t \cdot \hat{l})$ be the angle between the parallel reference directions for $\boldsymbol{I}_t$ and for the sensor. With the choice of α being positive for clockwise rotations from $\hat{l}_t$ to $\hat{l}$ as seen looking "into
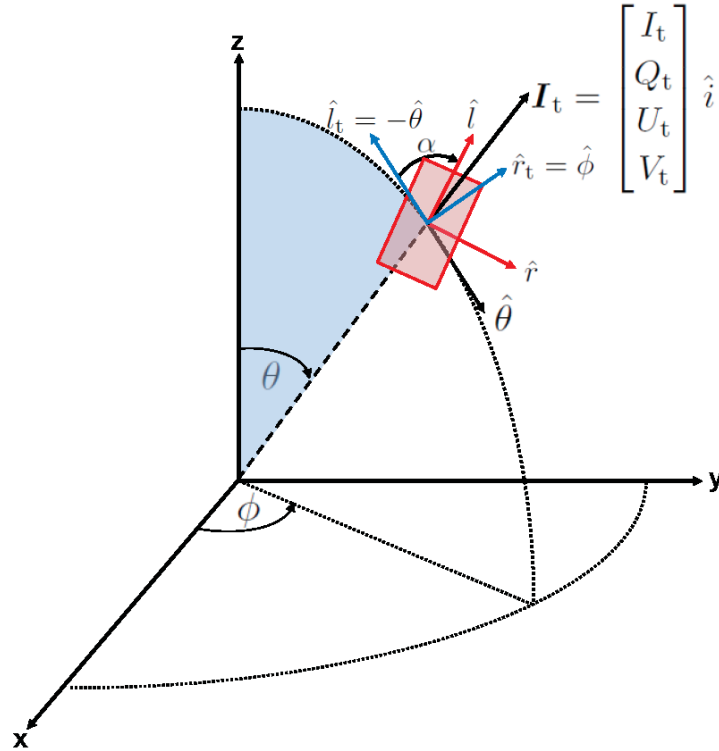

Figure 11.1: Angles and directions used in specification of Stokes vectors. The blue-shaded wedge indicates the meridional plane used to define the TOA Stokes vector $\boldsymbol{I}_t$ defined via the blue unit vectors; the red-shaded rectangle represents the sensor that measures $\boldsymbol{I}_m$ defined via the red unit vectors.

the beam" (looking in the $-\hat{\imath}$ direction), the transformation is given by the 4×4 rotation matrix

$$
\boldsymbol{R}(\alpha) =
\begin{bmatrix}
1 & 0 & 0 & 0 \\
0 & \cos(2\alpha) & \sin(2\alpha) & 0 \\
0 & -\sin(2\alpha) & \cos(2\alpha) & 0 \\
0 & 0 & 0 & 1
\end{bmatrix}.
\tag{11.1}
$$

Thus, the radiance as measured by the sensor is

$$
\boldsymbol{I}_{\mathrm{m}} = \boldsymbol{M}\boldsymbol{R}(\alpha)\boldsymbol{I}_{\mathrm{t}}.
\tag{11.2}
$$

It is important to note that the radiance measured by the sensor, $\boldsymbol{I}_{\mathrm{m}}$ depends both on the "true" TOA radiance $\boldsymbol{I}_{\mathrm{t}}$, the sensor optical properties via $\boldsymbol{M}$, and the orientation α of the sensor relative to the local meridional plane. $\boldsymbol{M}$ is fixed for a given sensor, but $\boldsymbol{I}_{\mathrm{t}}$ and α change from moment to moment as the sensor orbits and views the TOA radiance in different locations and directions. (To be exact, there are long-term changes to $\boldsymbol{M}$ caused by degradation of the sensor optical surfaces. These changes are monitored on-orbit and corrected by a cross-calibration technique.)

The quantity of interest here is the measured TOA radiance magnitude, which is given by the first element of the Stokes vector. Using (11.1) in Eq. (11.2) gives this to be

$$
\begin{aligned}
I_{\mathrm{m}} = M_{11}I_{\mathrm{t}} + &\, M_{12}[\cos(2\alpha)Q_{\mathrm{t}} + \sin(2\alpha)U_{\mathrm{t}}] \\
&+ M_{13}[-\sin(2\alpha)Q_{\mathrm{t}} + \cos(2\alpha)U_{\mathrm{t}}] + M_{14}V_{\mathrm{t}}.
\end{aligned}
\tag{11.3}
$$

Clearly, if $M_{11} = 1$ and all elements of $\boldsymbol{M}$ other than the M_{11} element are zero, then the sensor is not sensitive to the state of polarization and $I_{\mathrm{m}} = I_{\mathrm{t}}$. Physical arguments and numerical simulation show the circular polarization of the TOA radiance is very small: $|V_{\mathrm{t}}| \leq 10^{-3}I_{\mathrm{t}}$. This term is therefore neglected in the present correction algorithm. It is customary to define the elements of the *reduced* Mueller matrix by $m_{ij} \equiv M_{ij}/M_{11}$. Similarly defining reduced Stokes vector element by $q_{\mathrm{t}} \equiv Q_{\mathrm{t}}/I_{\mathrm{t}}$ and $u_{\mathrm{t}} \equiv U_{\mathrm{t}}/I_{\mathrm{t}}$, Eq. (11.3) becomes

$$
\begin{aligned}
I_{\mathrm{m}} = I_{\mathrm{t}}\{1 + &\, m_{12}[\cos(2\alpha)q_{\mathrm{t}} + \sin(2\alpha)u_{\mathrm{t}}] \\
&+ m_{13}[-\sin(2\alpha)q_{\mathrm{t}} + \cos(2\alpha)u_{\mathrm{t}}]\}.
\end{aligned}
\tag{11.4}
$$

Gordon et al. (1997a) gives the general procedure for measuring m_{12} and m_{13} in the laboratory. Meister et al. (2005) gives the details of these measurements for the MODIS sensors. These quantities, which specify the polarization sensitivity of the instrument, are determined before the instrument is launched; they are thus known. Angle α is determined by the orbit and pointing geometry of the sensor. It remains to determine the elements of $\boldsymbol{I}_{\mathrm{t}}$.

Following Eq. (1.3), the total TOA polarized radiance can be decomposed as

$$
\boldsymbol{I}_{\mathrm{t}} = \boldsymbol{I}_{\mathrm{R}} + \boldsymbol{I}_{\mathrm{a}} + \boldsymbol{I}_{\mathrm{Ra}} + T\boldsymbol{I}_{\mathrm{g}} + t\boldsymbol{I}_{\mathrm{wc}} + t\boldsymbol{I}_{\mathrm{w}}.
\tag{11.5}
$$

Here, as before, the Rayleigh (R), aerosol (a), and Rayleigh-aerosol (Ra) radiances are at the TOA; the glint (g), whitecap (wc), and water-leaving (w) radiances are at the sea surface. The surface values are transmitted to the TOA via the appropriate direct (T) and diffuse (t) transmittances. According to Eq. (11.2), each of these radiances must be known in order to predict what the sensor

will measure for a given TOA radiance and, thereby, to determine the correction needed to account for sensor polarization effects.

The surface-glint and atmospheric polarization contributions to the TOA signal are computed separately. Sea-surface glint can be highly polarized. This glint contribution to the TOA signal is computed using a vector radiative transfer code assuming a Rayleigh-scattering atmosphere above a rough Fresnel-reflecting ocean surface (Gordon and Wang, 1992; Wang, 2002; Meister et al., 2005). The water-leaving radiance is at most 10% of the TOA total, and the whitecap contribution is generally even less. These two terms are therefore ignored in the present development. The effect of aerosols and Rayleigh-aerosol interactions depends on the particle size distribution and concentration of the aerosols, which are unknown during atmospheric correction. Fortunately, numerical simulations show that the Rayleigh contribution to the TOA polarization is usually much greater than the aerosol-related contributions. Therefore, the aerosol contributions are also ignored and the polarization correction is based on the TOA Rayleigh radiance. The total TOA Stokes vector is then modeled as the sum of the glint and Rayleigh contributions.

Meister et al. (2005, Eq. 15) define the polarization correction via $p_c \equiv I_{\mathrm{m}}/I_{\mathrm{t}}$. Equations (11.3) and (11.4) allow this to be written as

$$p_c = \frac{1}{1 - m_{12}[\cos(2\alpha)Q_{\mathrm{t}} + \sin(2\alpha)U_{\mathrm{t}}]/I_{\mathrm{m}} - m_{13}[-\sin(2\alpha)Q_{\mathrm{t}} + \cos(2\alpha)U_{\mathrm{t}}]\}/I_{\mathrm{m}}} \ .$$

As applied during atmospheric correction, the unknown total TOA radiance components Q_{t} and U_{t} are replaced by the corresponding TOA Rayleigh components Q_R and U_R. The Rayleigh components are precomputed and tablulated for use during the first step of the atmospheric correction process, namely the removal of the Rayleigh contribution as described in §6. The end result is that the actual measured value I_{m} is used along with the Rayleigh radiance for the given atmospheric conditions and viewing geometry to obtain an estimate of the TOA radiance via

$$\begin{aligned} I_{\mathrm{t}} = I_{\mathrm{m}} &- m_{12}[\cos(2\alpha)Q_R + \sin(2\alpha)U_R] \\ &- m_{13}[-\sin(2\alpha)Q_R + \cos(2\alpha)U_R] \, . \end{aligned} \qquad (11.6)$$

Gordon et al. (1997a) show that this approximate polarization correction is acceptably accurate (errors $\Delta I_{\mathrm{t}}/I_{\mathrm{t}} < 0.01$ so long as the error has the same sign throughout the spectrum) when m_{12} is independent of wavelength and less than about 0.1 in magnitude. If m_{12} depends on wavelength, the approximation does not perform well for m_{12} as small as 0.02. Application of this polarization correction to MODIS Aqua imagery shows (Meister et al., 2005) that the polarization correction p_c is largest at blue wavelengths (the MODIS 412 nm band), where p_c lies in the range of 0.978 to 1.032.

References

Z. Ahmad and R. S. Fraser. An iterative radiative transfer code for ocean-atmosphere systems. *J. Atmos. Sci.*, 39:656–665, 1982.

Z. Ahmad, C. R. McClain, J. R. Herman, B. A. Franz, E. J. Kwaitkowska, W. D. Robinson, E. J. Bucsela, and M. Tzortziou. Atmospheric correction for NO2 absorption in retrieving water-leafing reflectances from the SeaWiFS and MODIS measurements. *Appl. Optics*, 39:6504–6512, 2007.

Z. Ahmad, B. A. Franz, C. R. McClain, E. J. Kwaitkowska, J. Werdell, E. P. Shettle, and B. N. Holben. New aerosol models for the retrieval of aerosol optical thickness and normalized water-leaving radiances from SeaWiFS and MODIS sensors over coastal regions and open oceans. *Appl. Optics*, 49:5545–5560, 2010a.

Z. Ahmad, B. A. Franz, C. R. McClain, E. J. Kwaitkowska, J. Werdell, E. P. Shettle, and B. N. Holben. New aerosol models for the retrieval of aerosol optical thickness and normalized water-leaving radiances from SeaWiFS and MODIS sensors over coastal regions and open oceans: publisher's note. *Appl. Optics*, 50:626, 2010b.

S. W. Bailey, B. A. Franz, and P. J. Werdell. Estimation of near-infrared water-leaving reflectance for satellite ocean color data processing. *Optics Express*, 18:7521–7527, 2010.

B. A. Bodhaine, N. B. Wood, E. G. Dutton, and J. R. Slusser. On Rayleigh optical depth calculations. *J. Atmos. Oceanic Technol.*, 16:1854–1861, 1999.

A. Bricaud, A. Morel, M. Babin, K. Allali, and H. Claustre. Variations of light absorption by suspended particles with chlorophyll a concentration in oceanic (case 1) waters: Analysis and implications for bio-optical models. *J. Geophys. Res.*, 103:31033–31044, 1998.

J. W. Campbell. The lognormal distribution as a model for bio-optical variability in the sea. *J. Geophys. Res.*, 100:13237–13254, 1995.

C. Cox and W. Munk. Measurement of the roughness of the sea surface from photographs of the sun's glitter. *J. Opt. Soc. Amer.*, 44:838–850, 1954.

Y. Fan, W. Li, K. J. Voss, C. K. Gatebe, and K. Stamnes. Neural network method to correct bidirectional effects in water-leaving radiance. *Appl. Optics*, 55:10–21, 2016.

B Franz. Atmospheric correction discussion: Where we are today and where we might be in 2.5 years, 2015. Presentation at the PACE Science Team Meeting; Jan 2014.

Available at `http://decadal.gsfc.nasa.gov/PACE/PACE_STM_01_2015/Presentations_day_2/BryanFranz_AC.pdf`.

B. Franz, S. W. Bailey, P. J. Werdell, and C. R. McClain. Sensor-independent approach to the vicarious calibration of satellite ocean color radiometry. *Appl. Optics*, 46:5068–5082, 2007.

R. Frouin, M. Schwindling, and P. Y. Dechamps. Spectral reflectance of sea foam in the visible and near infrared: In situ measurements and remote sensing implications. *J. Geophys. Res.*, 101: 14361–14371, 1996.

H. R. Gordon. Remote sensing of ocean color: a methodology for dealing with broad spectral bands and significant out-of-band response. *Appl. Optics*, 34:8363–8374, 1995.

H. R. Gordon. Normalized water-leaving radiance: revisiting the influence of surface roughness. *Appl. Optics*, 44:241–248, 2005.

H. R. Gordon and B. Franz. Remote sensing of ocean color: Assessment of the water-leaving radiance bidirrectional effects on the atmospheric diffuse transmittance for SeaWiFS and MODIS intercomparisons. *Rem. Sens. Environ.*, 112:2677–2685, 2008.

H. R. Gordon and M. Wang. Surface-roughness considerations for atmospheric correction of ocean color sensors. I: the Rayleigh-scattering component. *Appl. Optics*, 31:4247–4260, 1992.

H. R. Gordon and M. Wang. Retrieval of water-leaving radiance and aerosol optical thickness over the oceans with SeaWiFS: a preliminary algorithm. *Appl. Optics*, 33:443–452, 1994a.

H. R. Gordon and M. Wang. Influence of oceanic whitecaps on atmospheric correction of ocean-color sensors. *Appl. Optics*, 33:7754–7763, 1994b.

H. R. Gordon, O. B. Brown, R. H. Evans, J. W. Brown, R. C. Smith, K. S. Baker, and D. K. Clark. A semianalytical radiance model of ocean color. *J. Geophys. Res.*, 93:10909–10924, 1988.

H. R. Gordon, T. Du, and T. Zhang. Atmospheric correction of ocean color sensors: analysis of the effects of residual instrument polarization sensitivity. *Appl. Optics*, 36:69386948, 1997a.

H. R. Gordon, T. Du, and T. Zhang. Remote sensing of ocean color and aerosol properties: resolving the issue of aerosol absorption. *Appl. Optics*, 36:8670–8684, 1997b.

J. E. Hansen and L. D. Travis. Light scattering in planetary atmospheres. *Space Sci. Rev.*, 16: 527–610, 1974.

P. Koepke. Effective reflectance of oceanic whitecaps. *Appl. Optics*, 23:1816–1824, 1984.

Z.-P. Lee, R. A. Arnone, C.-M. Hu, P. J. Werdell, and B. Lubac. Uncertainties of optical parameters and their propagations in an analytical ocean color inversion algorithm. *Appl. Optics*, 49:369–381, 2010.

Z. P. Lee, K. Du, K. J. Voss, G. Zibordi, B. Lubac, R. Arnone, and A. Weidemann. An inherent-optical-property-centered approach to correct the angular effects in water-leaving radiance. *Appl. Optics*, 50:3155–3167, 2011.

G. Meister, E. J. Kwiatkowska, B. A. Franz, F. S. Patt, G. C. Feldman, and C. R. McClain. Moderate-resolution imaging spectroradiometer ocean color polarization correction. *Appl. Optics*, 44:55245535, 2005.

C. D. Mobley. Estimation of the remote-sensing reflectance from above-surface measurements. *Appl. Optics*, 38:7442–7455, 1999.

C. D. Mobley. Polarized reflectance and transmittance properties of wind-blown sea surfaces. *Appl. Optics*, 54:4828–4849, 2015.

A. Morel and B. Gentili. Diffuse reflectance of oceanic waters: its dependence on Sun angle as influenced by the molecular scattering contribution. *Appl. Optics*, 30:4227–4438, 1991.

A. Morel and B. Gentili. Diffuse reflectance of oceanic waters: II: Bidirectional aspects. *Appl. Optics*, 32:6864–6879, 1993.

A. Morel and B. Gentili. Diffuse reflectance of oceanic waters: III: Implication of bidirectionality for the remote-sensing problem. *Appl. Optics*, 35:4850–4862, 1996.

A. Morel and S. Maritorena. Bio-optical properties of oceanic waters: A reappraisal. *J. Geophys. Res.*, 106:7163–7180, 2001.

A. Morel, D. Antoine, and B. Gentili. Bidirectional reflectance of oceanic waters: accounting for Raman emission and varying particle scattering phase function. *Appl. Optics*, 41:6289–6306, 2002.

F. S. Patt, R. A. Barnes, Jr. R. E. Eplee, B. A. Franz, G. C. Feldman, S. W. Bailey, J. Gales, J. Werdell, M. Wang, R. Frouin, R. P. Stumpf, R. A. Arnone, Jr. R. W. Gould, P. M. Martinolich, V. Ransibrahmanakul, J. E. O'Reilly, and J. A. Yoder. Volume 22, Algorithm updates for the fourth SeaWiFS data reprocessing. In S. B. Hooker and E. R. Firestone, editors, *SeaWiFS Postlaunch Technical Report Series*, pages 1–74. NASA, 2003.

E. P. Shettle and R. W. Fenn. Models for the aerosols of the lower atmosphere and the effects of humidity variation on their optical properties, 1979. Environ. Res. Paper 676, AFGL-TR-79-0214.

J. Stramska and T. Petelski. Observations of oceanic whitecaps in the north polar waters of the atlantic. *J. Geophys. Res*, 108, 2003. doi: 10.1029/2002JC001321.

K. J. Voss, A. Morel, and D. Antoine. Detailed validation of the bidirectional effect in various Case 1 waters for application to ocean color imagery. *Biogeosciences*, 4:781–789, 2007.

M. Wang. The Rayleigh lookup tables for the SeaWiFS data processing: accounting for the effects of ocean surface roughness. *Internat. J. Remote Sensing*, 23:26932702, 2002.

M. Wang. A refinement for the Rayleigh radiance computation with variation of the atmospheric pressure. *Internat. J. Remote Sensing*, 26:56515653, 2005.

M. Wang and S. W. Bailey. Correction of sun glint contamination of the SeaWiFS ocean and atmosphere products. *Appl. Optics*, 40:4790–4798, 2001.

P. J. Werdell. Ocean color satellite atmospheric correction, 2015. Lecture at the 2015 Univ. of Maine Summer Class in Optical Oceanography and Remote Sensing. Video of the lecture is available at `https://www.youtube.com/playlist?list=PLQesc2lgL_DVxIS4AlkFigT_jq_5HIChX`.

P. J. Werdell, B. A. Franz, J. T. Lefler, W. D. Robinson, and E. Boss. Retrieving marine inherent optical properties from satellites using tempreature and salinity-dependent backscattering by seawater. *Optics Express*, 21:32611–32622, 2013.

H. Yang and H. R. Gordon. Remote sensing of ocean color: Assessment of the water-leaving radiance bidirectional effects on the atmospheric diffuse transmittance. *Appl. Optics*, 36:7887–7897, 1997.